TECHNISCHE UNIVERSITÄT MÜNCHEN
PHYSIK DEPARTMENT

Max-Planck-Institut für Astrophysik

Explosion and Remnant Systematics for Core-Collapse Supernovae in one Dimension

Marcella Ugliano

Vollständiger Abdruck der von der Fakultät für Physik der Technischen Universität München zur Erlangung des akademischen Grades eines

Doktors der Naturwissenschaften (Dr. rer. nat.)

genehmigten Dissertation.

Vorsitzender: Univ.-Prof. Dr. St. Paul

Prüfer der Dissertation:

1. Priv.-Doz. Dr. H.-Th. Janka
2. Univ.-Prof. Dr. W. Weise

Die Dissertation wurde am 30.04.2012 bei der Technischen Universität München eingereicht und durch die Fakultät für Physik am 25.06.2012 angenommen.

Chapter 1

Introduction

Hardly any other astrophysical event is as complex and physically diverse as the death of massive stars in a gravitational collapse and subsequent supernova explosion. The mechanism of conversion of gravitational potential energy from the collapsing iron core (with a radius similar to that of the Earth) into a shock-induced explosion has been the subject of intense theoretical activity in the modern computational era. The bounce from the imploding mantle rebounding off the nuclear density proto-neutron star does not inject enough energy to produce a shock with momentum sufficient to reach the surface [Wilson et al., 1986, Myra and Bludman, 1989, Swesty et al., 1994, Janka et al., 2007]. At the extreme temperatures and densities in the collapsing core, neutrinos of all three flavors are created with a total energy emission of around $3 \cdot 10^{53}$ erg. Deposition of a small fraction of this energy has been proposed as the energy source to drive the explosion [Colgate and White, 1966, Bethe and Wilson, 1985, Janka et al., 2007], and recent work has advocated the idea of acoustic vibrations of the proto-neutron star [Burrows et al., 2006]. The discovery of neutrinos from SN1987A confirmed the collapsing core idea in spectacular fashion [Hirata et al., 1987]. A final breakthrough in our understanding of how supernova explosions work, generally accepted and based on self-consistent models with all relevant physics included, however, has not been achieved yet (see Section 1.1).

Core collapse supernovae display a huge variety in their physical properties, such as remnant mass, explosion energy, and composition of the ejecta. For those cases where a progenitor star has been linked to the supernova event, observers have found significant variability even for stars of similar initial mass [see Smartt, 2009]. This variability could either be explained by differences in the structure of (nonrotating) stars of similar initial mass that can reflect in different explosion properties, or they might be connected to variations of the explosion mechanism, e.g. dependent on additional stellar parameters like rotation or strong magnetic fields.
Furthermore, observations of binaries containing neutron stars and black holes (e.g., X-ray binaries and binary pulsars) place constraints on their mass distribution. Estimates of the neutron star mass distribution have benefitted from observations of close pulsar binary systems where extremely accurate masses can be obtained through pulsar timing. Recently it has become clear that the mass distribution is at least bimodal, and likely has a wide spread ranging from low masses up to the maximum neutron star mass limit [Schwab et al., 2010, Valentim et al., 2011].
Black hole mass measurements rely on a complex combination of challenging observations of X-ray binaries (in quiescence, if they are transient) and of modeling of photometric and spectroscopic data. The uncertainties associated with these measurements are more significant than in the case of neutron stars. Recent analyses report that the minimum black hole mass lies in the range 4-5 $M_\odot$ and conclude that there is clear evidence for a gap in the compact objects distribution, with no remnants found in between

the maximum neutron star mass (~ 2 $M_\odot$) and 4-5 $M_\odot$ [Özel et al., 2010, Farr et al., 2011].

Knowledge of the connection between progenitor properties and explosion properties is a fundamental component in understanding the explosions and many studies have been devoted to this subject.
Woosley and Weaver [1995] calculated explosions for a grid of stellar masses and metallicities and followed explosive nucleosinthesys. Each star was exploded using a piston to give a specified final kinetic energy at infinity. They found that in most cases the final mass of the collapsed remnant did not correspond to the location of the piston, but to a "mass cut" farther out. This mass cut was found to be sensitive to the explosion energy, the presupernova structure, the stellar mass and the metallicity. They also found that the reverse shock generated when the supernova front shock travels through the hydrogen envelope of the star can decelerate a significant amount of matter, further increasing the final remnant mass. Woosley and Weaver [1995] concluded that stars larger than about 30 $M_\odot$ would experience considerable reimplosion of heavy elements following the initial launch of a successive shock and may leave black hole remnants up to 10 and more solar masses.
Thielemann et al. [1996] performed a similar study. They initiated the explosions with thermal energy deposition and they adjusted the parameters of their models in order to eject ^{56}Ni masses in agreement with supernova light curves. However they only study four progenitors of solar metallicity. Their results agree reasonably well with Woosley and Weaver [1995], after taking into account the systematic differences originating from different physics employed.

Woosley et al. [2002], Heger et al. [2003] extended the work of Woosley and Weaver [1995], including the effect of mass loss during the presupernova evolution which was neglected in Woosley and Weaver [1995] and increasing the number of progenitors studied. The predictions from all these works are summarized by Heger et al. [2003] in the diagram that is shown in Figure 1.1, which represents the current paradigm for the outcome of core-collapse supernovae. For solar metallicity, stars with an initial mass lower than about 25 $M_\odot$ will form neutron stars, while more massive stars will undergo weak explosions and form black holes some time after the explosion, because part of the material initially ejected does not have enough energy to escape and will fall back on the compact remnant. There might be a "window" of neutron stars formed by very massive stars (more than ~ 60 $M_\odot$) depending on the still uncertain mass loss rate of these stars during presupernova evolution. For lower metallicities, stars more massive than roughly 40 $M_\odot$ will not explode but directly collapse to a black hole. The exact thresholds between different regimes depend on many uncertain parameters.

Zhang et al. [2008] repeated this study starting from recently computed progenitors of solar and zero metallicity, and found results in agreement with previous works.
All these works, however, suffer from a great limitation: the explosions are initiated artificially, either by means of a piston or by deposition of energy, and neutrino physics is completely neglected. Both procedures are not based on a physical model of the explosion mechanism and have two major shortcomings: the explosion energy and the mass cut are imposed by hand and ad-hoc assumptions are made for the collapse phase.

Fryer [1999] computed two-dimensional simulations with a simplified scheme for neutrino transport to study the mass limits for black hole formation. He employed three different progenitors (which initial masses were 15, 25 and 40 $M_\odot$) and studied the effect of variating the neutrino energy input. This study confirmed the paradigm that stars more massive than ~ 25 $M_\odot$ form black holes (either via direct collapse or via fallback), but the major weaknesses of this work were the limited amount of progenitors studied

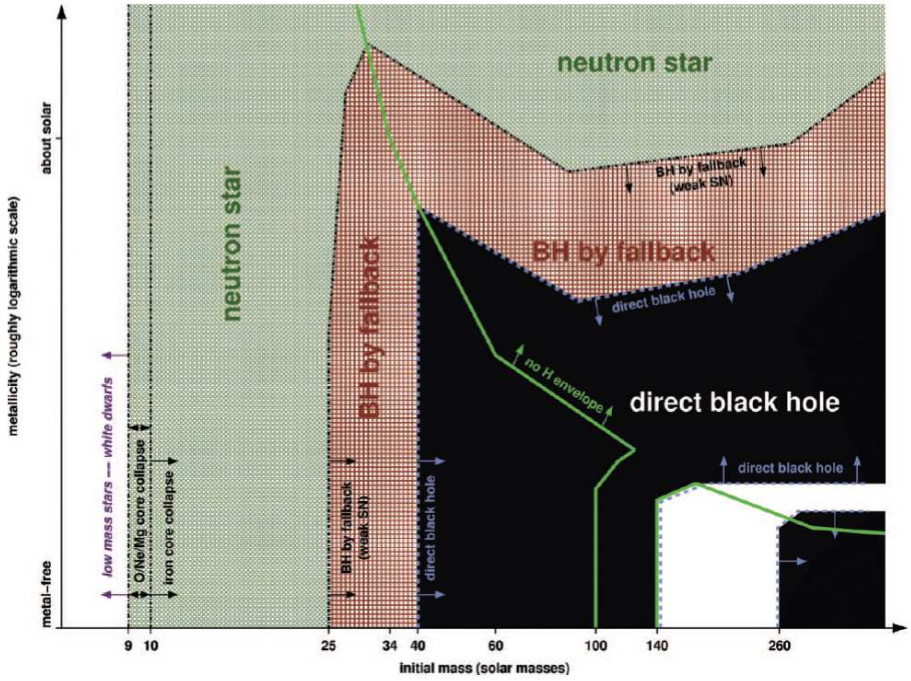

Figure 1.1: Remnants of massive single stars as a function of initial metallicity (y-axis; qualitatively) and initial mass (x-axis). The thick green line separates the regimes where the stars keep their hydrogen envelope from those where the hydrogen envelope is lost. The dashed blue line indicates the border of the regime of direct black hole formation (black). This domain is interrupted by a strip of pair-instability supernovae that leave no remnant (white). Outside the direct black hole regime, at lower mass and higher metallicity, follows the regime of BH formation by fallback (red cross-hatching and bordered by a black dot-dashed line). Outside of this, green cross-hatching indicates the formation of neutron stars. The lowest mass neutron stars may be made by O/Ne/Mg core collapse instead of iron core collapse (vertical dot-dashed lines at the left). At even lower mass, the cores do not collapse and only white dwarfs are made (white strip at the very left). Credit: Heger et al. [2003]

and the short time for which the simulations were carried on, ~ 1 s. The final remnant mass was calculated assuming that only the material whose binding energy was equal to the explosion energy at 1 s would be ejected, whereas the remaining material would fall back, which is rather simplistic since (i) the explosion energy might not be saturated yet at 1 s and (ii) any fallback driven by a reverse shock is ignored.
More recently, Fryer [2006] developed an analytical recipe to estimate the explosion energy in core-collapse supernovae, based on the assumption that the energy reservoir is limited to the convective region bounded by the edge of the proto-neutron star and the supernova shock. This recipe was used in Fryer et al. [2012] to study the dependence of the compact remnant mass function on the delay between core bounce and explosion. They find that if the explosion happens quickly (less than 250 ms after core bounce) the mass function has the same bimodality found by observers, while this bimodality disappears if the explosion is delayed as found in tipycal core collapse simulations [Janka et al., 2007]. They conclude that if the observational gap is confirmed, this might be a constraint on the explosion mechanism. However these results are based on a great number of assumptions and simplifications.

The study of the connection between progenitors and remnants which employs the most accurate treatment of the explosion mechanism is the work of O'Connor and Ott [2011].

They presented the results of a systematic study of failing core-collapse supernovae and the formation of stellar-mass black holes, performed with a general-relativistic 1.5D code with simplified neutrino transport. They study the dependence of black hole formation on progenitor compactness, precollapse rotational setup, neutrino heating efficiency and nuclear Equation of State (EoS).
They find that the outcome of core-collapse, for a given EoS, can be estimated, to first order, by a single parameter, the "compactness parameter", defined as

$$\xi_{2.5} = \frac{2.5 M_\odot / M_\odot}{R(M_{bary} = 2.5 M_\odot)/10^8 \text{ cm}}.$$

which, calculated at the time of core bounce, estimates the compactness of the stellar core at bounce.
The main shortcoming of this work was that no explosions were computed, therefore the only predictions that are made are for black hole mass and number. Furthermore, in order to estimate wether a model explodes or collapses to a black hole ad hoc assumptions on the neutrino heating were made.
Therefore, predictions of the initial-final remnant mass function and of explosive nucleosynthesis are still based on very simple and physically inaccurate methods to initiate the explosions.

We propose a novel approach to the study the connection between progenitors and the properties of core-collapse supernovae, based on a physically motivated mechanism for launching the explosions, namely neutrino energy deposition. Although the viability of this explosion mechanism is still under debate, it is clear that neutrino heating plays an important role in core collapse [Janka et al., 2007]. Moreover, recent sophisticated multidimensional simulations with detailed neutrino treatment are at least near the critical conditions for a success of the neutrino-driven mechanism [Buras et al., 2006b, Marek and Janka, 2009, Müller et al., 2012]. Therefore, adopting this approach is likely to be a step towards more realistic modeling of the explosions.
Here we will present the results of spherically symmetric explosion simulations for a set of about 100 progenitor stars of solar metallicity. The explosions were initiated by means of a neutrino-heating scheme that depends on parametrized neutrino quantities (luminosities and mean spectral energies) based on an analytic cooling model of the high-density core of the nascent neutron star. The free parameters of this model were calibrated by reproducing the observed properties of SN1987A (explosion energy, remnant mass and nickel ejection) with a suitable progenitor from our set, and kept constant for all calculations. The evolution of the explosion models was followed beyond shock breakout from the stellar surface in order to calculate the amount of material that falls back and the final remnant mass.

This thesis is structured as follows. In Chapter 2 we outline the numerical techniques adopted for our simulations (in particular, the neutrino-heating scheme is described in Section 2.3). In Chapter 3 we present the progenitors employed for this study and explain their most important properties. In Chapter 4 we compare the results of initiating the explosions with neutrino heating or with pistons, and we show that neglecting the effects of neutrinos can have a great impact on the predictions for remnant masses and nucleosynthetic yields. In Chapter 5 we present the results of neutrino driven explosion simulations for the full set of progenitors.

1.1 The neutrino-heating mechanism

At the end of hydrostatic burning, a massive star consists of concentric shells that are the relics of its previous burning phases (hydrogen, helium, carbon, neon, oxygen, silicon).

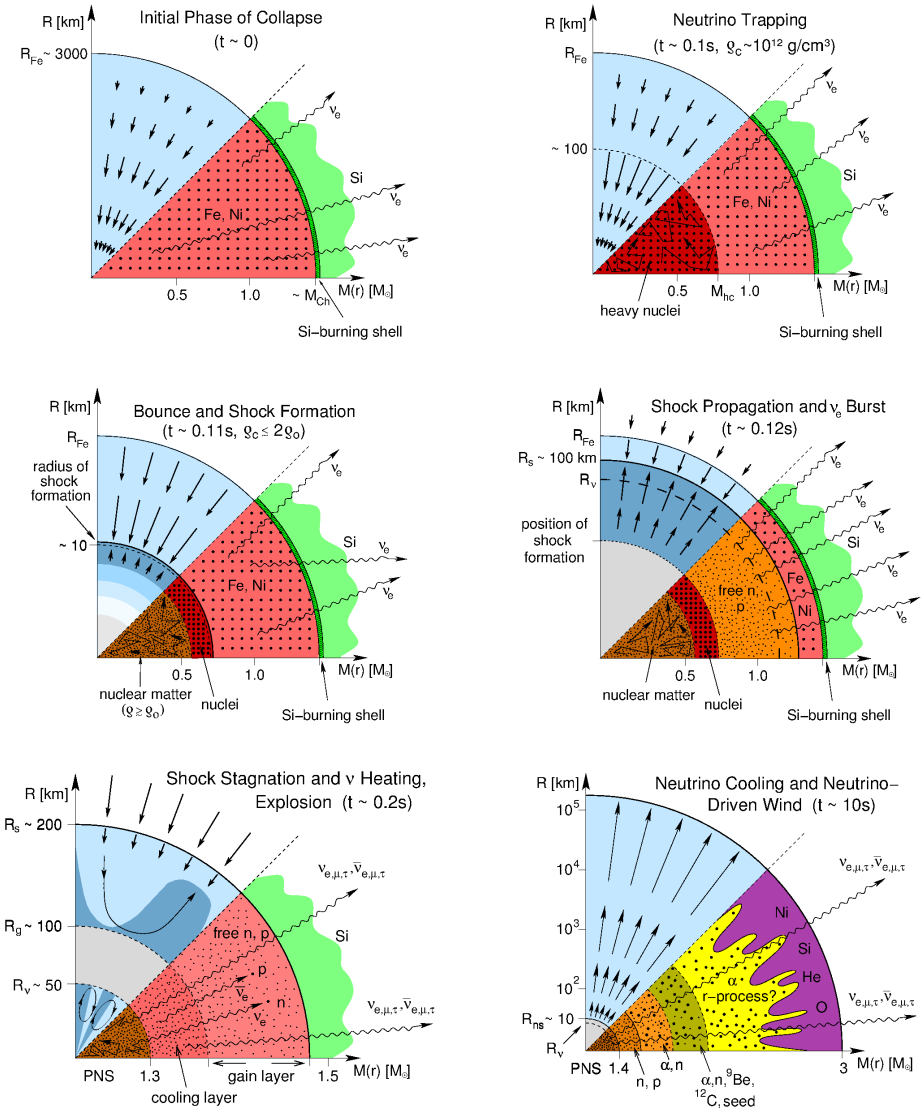

Figure 1.2: Schematic representation of the evolutionary stages from stellar core collapse through the onset of the supernova explosion to the neutrino-driven wind during the neutrino-cooling phase of the proto-neutron star (PNS). The panels display the dynamical conditions in their upper half, with arrows representing velocity vectors. The nuclear composition as well as the nuclear and weak processes are indicated in the lower half of each panel. Credit: Janka et al. [2007]

Iron is the final stage of nuclear fusion in hydrostatic burning, as the synthesis of any heavier element from lighter elements does not release energy; rather, energy must be used up. When the iron core, formed in the center of the massive star, grows by silicon shell burning to a mass around the Chandrasekhar mass limit of about 1.44 solar masses, electron degeneracy pressure cannot longer stabilize the core and it collapses. This starts what is called a core-collapse supernova in course of which the star explodes and parts of the star's heavy-element core and of its outer shells are ejected into the Interstellar Medium.

The onset of the collapse and the infall dynamics are very sensitive to the entropy and to

the number of leptons per baryon, Y_e [Bethe et al., 1979]. In turn, these two quantities are mainly determined by weak interaction processes, electron capture and β decay. First, in the early stage of the collapse, Y_e decreases by electron capture on (Fe-peak) nuclei, reactions which are energetically favorable when the electrons have Fermi energies of a few MeV at the densities involved. This reduces the increase of the electron pressure with density, thus accelerating the collapse, and shifts the distribution of nuclei present in the core to more neutron-rich material (Fig. 1.2, upper left panel). Second, many of the nuclei present can also β decay. While this process is quite unimportant compared to electron capture for initial Y_e values around 0.5, it becomes increasingly competitive for neutron-rich nuclei due to an increase in phase space related to larger Q_β values.

Electron capture, β decay, and partial photodisintegration of iron-group nuclei to alpha particles cost the core energy and reduce its electron density. As a consequence, the collapse is accelerated. An important change in the physics of the collapse occurs as the density reaches $\rho_{trap} \approx 10^{12}\mathrm{g/cm}^3$ (Fig. 1.2, upper right panel). Then neutrinos are essentially trapped in the core, because their diffusion time (due to coherent conservative scattering on nuclei) becomes larger than the collapse time [Bethe, 1990]. After neutrino trapping, the collapse proceeds essentially homologously [Goldreich, 1980], until nuclear densities ($\rho_0 \approx 10^{14}\mathrm{g/cm}^3$) are reached. Since nuclear matter has a much lower compressibility, the homologous core decelerates and bounces in response to the increased nuclear matter pressure. This drives a shock wave into the outer core, i.e. the region of the iron core which lies outside of the homologous core and in the meantime has continued to fall inwards at supersonic speed.

The core bounce with the formation of a shock wave is the starting point of a sequence of events that ultimately triggers a supernova explosion (Fig. 1.2, middle left panel), but the exact mechanism of the explosion and the crucial ingredients of this physically appealing scenario are still uncertain and controversial. If the shock wave is strong enough not only to stop the collapse, but also to explode the outer burning shells of the star, one speaks about the "prompt mechanism". However, it appears as if the energy available to the shock is not sufficient, and the shock uses up its energy in the outer core mostly by the dissociation of heavy nuclei into nucleons. This change in composition results in even more energy loss, because the electron capture rate on free protons is significantly larger than on neutron-rich nuclei due to the higher Q-values of the latter. A large fraction of the neutrinos produced by these electron captures behind the shock leave the star quickly in what is called the neutrino burst at shock break-out, carrying away energy.
This leads to further neutronization of the matter. The shock is weakened so much that it finally stalls and turns into an accretion shock at a radius between 100 and 200 km, i.e., the matter downstream of the shock has negative velocities and continues falling inward (Fig. 1.2, middle right panel). All state-of-the-art simulations of stellar core collapse agree with the models of the 1980's and 1990's [e.g. Wilson et al., 1986, Myra and Bludman, 1989, Swesty et al., 1994] that the prompt shock is unable to trigger supernova explosions.

After core bounce, a compact remnant begins to form at the center of the collapsing star, rapidly growing by the accretion of infalling stellar material until the explosion sets in. This nascent remnant - the proto-neutron-star - will evolve to a neutron star or may eventually collapse to a black hole. The newly born neutron star is initially still proton-rich and contains a large number of degenerate electrons and neutrinos. The latter are trapped because their mean free paths in the dense matter are significantly shorter than the radius of the neutron star. It takes a fraction of a second for the trapped neutrinos to diffuse out (Fig. 1.2, lower panels). On their way to the neutrinosphere, the neutrinos are down-scattered in energy space, thus converting their initially high degeneracy energy to thermal energy of the stellar medium [Burrows and Lattimer, 1986]. The further cooling

of the hot interior of the proto-neutron star then proceeds by neutrino-pair production and diffusive loss of neutrinos of all three lepton flavors. After several tens of seconds the compact remnant becomes transparent to neutrinos and the neutrino luminosity drops significantly [Burrows, 1988].

In the explosion scenario by the "delayed neutrino-heating mechanism", the stalled shock wave can be revived by the neutrinos streaming off the neutrinosphere. These neutrinos carry most of the energy set free in the gravitational collapse of the stellar core and deposit some of their energy in the layers between the nascent neutron star and the stalled shock front mainly by charged-current ν_e and $\bar{\nu}_e$ captures on free nucleons,

$$\nu_e + n \Rightarrow e^- + p, \tag{1.1}$$

$$\bar{\nu}_e + p \Rightarrow e^+ + n, \tag{1.2}$$

(Fig. 1.2, lower left panel). This neutrino heating increases the pressure behind the shock and the heated layers begin to expand, creating between shock front and neutron star surface a region of low density but rather high temperature, the so-called "hot bubble" [Colgate, 1989]. The persistent energy input by neutrinos keeps the pressure high in this region and drives the shock outwards again, eventually leading to a supernova explosion. This may take a few 100 ms and requires that during this time interval a few percent of the radiated neutrino energy (or 10-20% of the energy of electron neutrinos and antineutrinos) are converted to thermal energy of nucleons, leptons, and photons. The canonical explosion energy of a supernova is less than one percent of the total gravitational binding energy lost by the nascent neutron star in neutrinos.

The success of the delayed supernova mechanism turned out to be sensitive to a delicate competition of neutrino cooling between the neutrinosphere and the so-called "gain radius" on the one hand, and neutrino heating between the gain radius and the shock on the other (Fig. 1.2, lower left panel). The gain radius is defined as the radial position where the neutrino heating rate per nucleon and the neutrino cooling rate per nucleon become equal.
Only if the heating is sufficiently strong, depending on the size of the neutrino luminosities and the hardness of the neutrino spectra, an explosion can be triggered [Janka, 2001, and citations therein]. The effect is self-enhancing: strong heating of the matter accreted by the shock decelerates the infall and increases the time for matter to absorb neutrino energy, thus raising the efficiency of energy deposition by neutrinos. This positive feedback leads to further shock expansion and can initiate the final runaway. Strong cooling has the opposite effect. It accelerates the accretion flow through the gain layer and largely reduces the time matter is exposed to heating, hence diminishing the chance for an explosion [Janka, 2001].

Spherically simmetryc simulations with the state-of-the-art treatment of hydrodynamics and neutrino transport, disregarding multi-dimensional effects [e.g. Rampp and Janka, 2000, Mezzacappa et al., 2001, Buras et al., 2006b], agree that no delayed explosion can be obtained for progenitors more massive than 10 $M_\odot$.
In contrast, in case of stars with birth masses of 8-10 $M_\odot$, which do not develop an iron core but a core of oxygen, neon and magnesium with a thin carbon shell, surrounded by an extremely dilute and only loosely bound helium shell, neutrino heating was found to power explosions in one-dimensional (1D) simulations, although low energetic (only 0.1-0.2 bethe) [Kitaura et al., 2006].
With the currently most sophisticated treatment of neutrino transport that is applied in multidimensional supernova simulations (at the same level of refinement in the treatment of neutrino-matter interactions as in the state-of-the-art 1D models), neutrino heating and postshock convection were found to trigger a (probably rather weak) explosion only in case

of an 11.2 $M_\odot$ star [Buras et al., 2006b]. The more massive progenitors investigated by Buras et al. [2006b] did not explode during the simulated evolution periods of about 300 ms after core bounce, although a crucial criterion, the ratio of advection timescale to heating timescale, indicates that the critical condition for an explosion was not missed by much (roughly a factor of two in the 2D, 90° cases).
The onset of the explosion of the 11.2 $M_\odot$ star was aided by a recently discovered generic instability of the accretion shock to non-radial deformation. This so-called SASI (standing accretion shock instability, Blondin et al. [2003]) shows highest growth rates of the l=1,2 modes (i.e., the dipole and quadrupole terms of an expansion in spherical harmonics) and causes a bipolar sloshing of the shock with pulsational strong expansion and contraction. Since the shock is pushed farther out and the time matter stays in the heating layer therefore increases, this strengthens the neutrino-energy deposition and ultimately leads to a globally asymmetric initiation of the explosion. The SASI was found to be present in all multi-dimensional core-collapse simulations when the onset of the explosion was delayed for a sufficiently long time to allow the instability to develop.

However, self-consistent models for progenitor masses larger than about 12 $M_\odot$ do not produce explosions. It is not clear what is still missing. Three-dimensional simulations with sophisticated energy-dependent neutrino transport are definitely needed, however it is controversial wether explosions in 3D occur easier and earlier than in 2D [Hanke et al., 2011]. Even fundamental constraining parameters and ingredients are controversial. Do we understand the neutrino physics sufficiently well? Are our models correct in predicting the luminosities and mean energies of the radiated neutrinos? How important is rotation in the collapsing core? Do magnetohydrodynamic effects play a crucial role, tapping a large reservoir of free energy of rotation? Maybe the identification of such key aspects in the explosion mechanism will require observations that yield more direct evidence of what is going on in the supernova core than can be provided by explosion asymmetries, pulsar kicks or nucleosynthesis yields. The measurement of neutrino signals and gravitational waves will be able to yield such information, but that will require a galactic supernova to happen.

Chapter 2

Fundamental Equations and Numerical Methods

The analysis of the evolution of supernovae requires the solution of the hydrodynamics equations for supersonic, compressible fluids, coupled to the Poisson equation for gravity and the equation of radiative transfer for the neutrinos streaming away from the nascent neutron star. This system of equations cannot be solved analytically without a great number of assumptions and simplifications, therefore the numerical approach is essential to study the evolution of the supernova in detail.

The code employed is PROMETHEUS-HOTBubble, a neutrino-hydrodynamics code composed of several modules.

The *hydrodynamics* module is a direct implementation of the Piecewise Parabolic Method of Colella and Woodward [1984], a high-resolution shock capturing scheme that performs a conservative, (finite-volume) explicit integration of the Newtonian hydrodynamics equations with third-order accuracy in space and second-order accuracy in time, augmented by the Riemann solver of Colella and Glatz [1985] for real gases (see Sections 2.1 and 2.1.3).

General relativistic effects are approximated by using an "effective relativistic potential" (see Marek et al. [2006], Arcones et al. [2007] and Section 2.2).

The *neutrino transport* is based on a computationally very efficient, analytic integration along characteristics of the frequency-integrated zeroth-order moment equations of the Boltzmann equation for neutrino number and energy. The inner core of the neutron star is excised and replaced by a contracting Lagrangian boundary, which mimics the shrinking of the nascent neutron star. We prescribe a neutrino flux at the inner boundary according to an analytic cooling model for the proto-neutron star, described in detail in Section 2.3.1, and the neutrino spectra are assumed to have Fermi-Dirac distribution with a spectral temperature that is determined from the ratio of neutrino energy flux to neutrino number flux. Closure is achieved by employing the flux factor $f(r,t) = F/Ec$, for which we use a prescribed function which was determined by fits to Monte Carlo transport results (see Scheck et al. [2006] and Section 2.3).

2.1 Hydrodynamics

The hydrodynamics equations are considered in Eulerian form for spherical symmetry with source terms for gravity, neutrino energy and momentum exchange with the stellar medium. The equations of continuity, momentum, and energy are:

$$\frac{\partial \rho}{\partial t} + \frac{1}{r^2}\frac{\partial}{\partial r}(r^2 \rho u) = 0, \tag{2.1}$$

$$\frac{\partial (\rho u)}{\partial t} + \frac{1}{r^2}\frac{\partial}{\partial r}(r^2 \rho u^2) = -\frac{\partial p}{\partial r} - \rho \frac{\partial \Phi}{\partial r}, \tag{2.2}$$

$$\frac{\partial e}{\partial t} + \frac{1}{r^2}\frac{\partial}{\partial r}[r^2 u(e+p)] = -\rho u \frac{\partial \Phi}{\partial r} + Q_{\nu,e}, \tag{2.3}$$

where r, u, ρ, p, t are radius, fluid velocity, density, pressure and time and e is the sum of internal and kinetic energy densities. The term $Q_{\nu,e}$ denotes the rate of energy gain or loss per unit volume by neutrino heating and cooling. Φ(r) is an effective potential which contains contributions from the gravitational potential and from the momentum transfer to the stellar gas by neutrinos (see Section 2.2).
Closure is provided by specifying an Equation of State (EoS) relating thermodinamic quantities. We employ two different Equations of State, which are described in section 2.1.1.

In the case of nuclear statistical equilibrium (NSE), a third independent variable, the electron fraction Y_e, is sufficient to characterize the composition. For this variable the evolution is computed according to a conservation equation

$$\frac{\partial}{\partial t}(\rho Y_e) + \frac{1}{r^2}\frac{\partial}{\partial r}(r^2 \rho Y_e u) = Q_{\nu,N}, \tag{2.4}$$

where the source term $Q_{\nu,N}$ is the rate of change of the net electron fraction (i.e. the number fraction of electrons minus that of positrons) due to emission and absorption of electron-flavor neutrinos. In case the medium is not in NSE, an equation like Eq. (2.4) has to be solved also for the abundance of each nucleus k, $Y_k \equiv n_k / n_{by}$, using

$$\frac{\partial}{\partial t}(\rho Y_k) + \frac{1}{r^2}\frac{\partial}{\partial r}(r^2 \rho Y_k u) = R_k, \tag{2.5}$$

where n_k and n_{by} are the number density of nucleus k and the baryon number density, respectively, and R_k is a source term that describes the rate of composition changes by nuclear reactions for species k.
Note that PROMETHEUS only solves the left-hand sides of the hydrodynamic Eqs. (2.1)-(2.5) and that the EoS is not evaluated during this procedure. The computation of the terms on the right-hand sides, i.e. the gravitational, neutrino, and burning effects, as well as the evaluation of the EoS and, if necessary, the determination of the NSE composition, are done in operator split steps.

2.1.1 Equations of State

We use two equations of state, both based on the same baryon composition: free nucleons, α particles and a representative heavy nucleus of the iron group (chosen to be ^{54}Mn). Nucleons and nuclei are treated as ideal, nonrelativistic Boltzmann gases; in addition, electrons and positrons contribute as arbitrarily degenerate and arbitrarily relativistic ideal Fermi gases. Photons are in equilibrium with the massive particles and their thermal effects are taken into account.

In the high-temperature regime ($T > 2 \cdot 10^9$ K) we use the EoS of Janka and Müller [1996], which assumes that baryons are in NSE. These four species are also used to compute

the energy source terms resulting from nuclear transmutations. Janka and Müller [1996] found good agreement with the EoS of Lattimer and Swesty [1991] up to densities of about $5 \cdot 10^{13}$ g/cm^3.

In the low-temperature regime we employ the EoS of Timmes and Swesty [2000]. It is based on table interpolation of the Helmholtz free energy for electrons and positrons. The interpolation scheme guarantees perfect thermodynamic consistency, independent of the interpolating function, while the choice of a biquintic Hermite polynomial as the interpolating function results in accurately reproducing the underlying Helmholtz free energy data in the table, and yields derivatives of the pressure, specific entropy, and specific internal energy which are smooth and continuous. The routine is computationally very efficient.

In addition to the small NSE "network", but without feedback to the EoS and the hydrodynamics, we also evolve a 14 species nuclear reaction network to approximately calculate the products of explosive nucleosynthesis, whose spatial distribution we wish to follow [see Kifonidis et al., 2003]. The latter network consists of the 13 α-nuclei from ^{4}He to ^{56}Ni and an additional tracer nucleus to which we channel the flow resulting from the reaction $^{52}\mathrm{Fe}(\alpha,\gamma)^{56}\mathrm{Ni}$ in case the electron fraction Y_e drops below 0.490 and ^{56}Ni ceases to be the dominant nucleus synthesized in the iron group. In this way we can "mark" material that freezes out from NSE at conditions of neutron excess and distinguish it from ^{56}Ni whose yield would otherwise be overestimated.

The 14 species network is solved for temperatures between 10^8 K and $7 \cdot 10^9$ K. Above $7 \cdot 10^9$ K, we assume that nuclei have been disintegrated to α-particles. Of course, the 14 species network is a simplification of the nucleosynthesis processes in a supernova, since it neglects important isotopes and production channels of the considered nuclei.

2.1.2 The Method of Godunov for Non-linear Systems

In this Section the general solution of a non-linear system of hyperbolic partial differential equations like (2.1)-(2.3) is explained. The numerical scheme employed in PROMETHEUS is described in detail in Section 2.1.3.
Consider the general Initial-Boundary Value Problem (IBVP) for non-linear systems of hyperbolic equations in one spatial dimension:

$$\begin{cases} \text{PDEs} & : \ \dfrac{\partial \mathbf{U}}{\partial t} + \dfrac{\partial \mathbf{F}(\mathbf{U})}{\partial x} = 0, \\ \text{ICs} & : \ \mathbf{U}(x,0) = \mathbf{U}^{(0)}(x), \\ \text{BCs} & : \ \mathbf{U}(0,t) = \mathbf{U}_l(t), \quad \mathbf{U}(L,t) = \mathbf{U}_r(t), \end{cases} \tag{2.6}$$

where $\mathbf{U}(x,t)$ is the vector of conserved variables, $\mathbf{F}(\mathbf{U})$ is the vector of fluxes, $\mathbf{U}^{(0)}(x)$ is the initial data at time t = 0, [0, L] is the spatial domain and boundary conditions are, for the moment, assumed to be represented by the boundary functions $\mathbf{U}_l(t)$ and $\mathbf{U}_r(t)$.
Let us assume that the solution of the IBVP (2.6) exists. In order to admit discontinuous solutions an integral form of the conservation laws in (2.6) has to be used:

$$\int_{x_1}^{x_2} \mathbf{U}(x,t_2)dx = \int_{x_1}^{x_2} \mathbf{U}(x,t_1)dx + \int_{t_1}^{t_2} \mathbf{F}(\mathbf{U}(x_1,t))dt - \int_{t_1}^{t_2} \mathbf{F}(\mathbf{U}(x_2,t))dt, \tag{2.7}$$

for any control volume $[x_1, x_2] \times [t_1, t_2]$ in the domain of interest.

Numerical methods replace the *continuous* problem by a *finite* set of *discrete* values. These are obtained by first discretising the domain of the equations into a finite set of points or volumes via a mesh or grid. The corresponding discretization of the equations on the grid

results in discrete values. In the Finite Difference approach one regards these values as *point values* defined at grid points. The Finite Volume approach regards these discrete values as *averages over finite volumes*. The second approach is the most commonly used.

The physics and mathematics embodied in the equations are intimately linked to the discretization procedure. In *upwind* schemes, spatial differencing is performed using mesh points on the side from which information (wind) flows. These schemes are stable under a condition that relates the mesh spacing Δx and the step size Δt, so they cannot vary independently.

The spatial domain [0,L] is discretized into M computing cells or finite volumes $I_i = [x_{i-1/2}, x_{i+1/2}]$ of regular size $\Delta x = L/M$, with i = 1, ..., M. For a given cell I_i the location of the cell centre x_i and the cell boundaries $x_{i-1/2}, x_{i+1/2}$ are given by:

$$x_{i-1/2} = (i-1)\Delta x, \quad x_i = (i-1/2)\Delta x, \quad x_{i+1/2} = i\Delta x. \tag{2.8}$$

The temporal domain [0,T] is generally discretized in steps Δt of variable size: since for non-linear systems wave speeds vary in space and time, the choice of Δt is carried out as marching in time proceeds.
Given general initial data $\widetilde{\mathbf{U}}(x, t^n)$ for (2.6) at time $t = t^n$, in order to evolve the solution to a time $t^{n+1} = t^n + \Delta t$, the Godunov method first assumes a *piecewise constant* distribution of the data. Formally, this is realized by defining *cell averages*

$$\mathbf{U}_i^n = \frac{1}{\Delta x} \int_{x-1/2}^{x+1/2} \widetilde{\mathbf{U}}(x, t^n) dx, \tag{2.9}$$

which produces the desired piecewise constant distribution $\mathbf{U}(x, t^n) = \mathbf{U}_i^n$, for x in each cell $I_i = [x_{i-1/2}, x_{i+1/2}]$, as illustrated in Figure 2.1 for a single component $\mathbf{U}_k$ of the vector of conserved variables. Data now consist of a set $\{\mathbf{U}_i^n\}$ of constant states in terms of the conserved variables. Other variables may be derived to proceed with the implementation of numerical methods, in particular, for the Godunov method the Riemann problem is solved in terms of primitive variables (for example, for the Euler equations primitive variables are density, velocity and pressure).

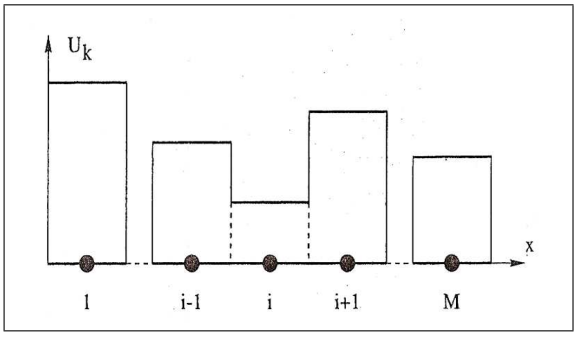

Figure 2.1: Piecewise constant distribution of data at time level n, for a single component of the vector **U**. Credit: Toro [1999]

The next step is to solve the Initial Value Problem (IVP) for the original conservation laws but with the modified initial data $\{\mathbf{U}_i^n\}$. Effectively, this generates local Riemann problems RP($\mathbf{U}_i^n, \mathbf{U}_{i+1}^n$) centered at the intercell boundary positions $x_{i+1/2}$:

$$\begin{cases} \dfrac{\partial \mathbf{U}}{\partial t} + \dfrac{\partial \mathbf{F}(\mathbf{U})}{\partial x} = 0, \\ \\ \mathbf{U}(x,n) = \begin{cases} \mathbf{U}_i^n & \text{if } x \leqslant x_{i+1/2}, \\ \mathbf{U}_{i+1}^n & \text{if } x > x_{i+1/2}. \end{cases} \end{cases} \tag{2.10}$$

The solution of (2.10) is a similarity solution $\mathbf{U}_{i+1/2}(\overline{x}/\overline{t})$ where $\overline{x}$, $\overline{t}$ are defined in Eq. (2.12). It consists of $m+1$ constant states separated by m waves, as shown in Figure 2.2. For each eigenvalue λ_i there is a wave family. For non-linear systems the waves may be discontinuities such as shock waves and contact waves, or smooth transition waves such as rarefactions.

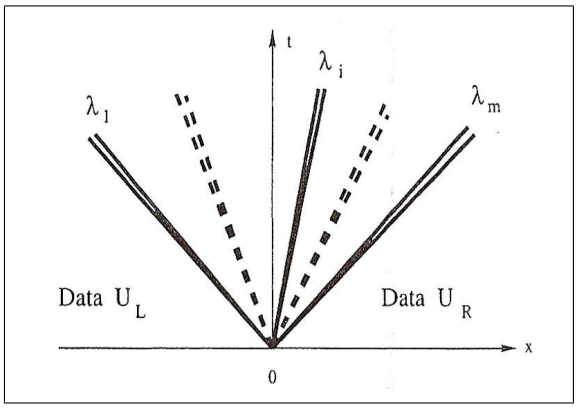

Figure 2.2: Structure of the solution of the Riemann problem for a system of non-linear conservation laws. Credit: Toro [1999]

For a time step Δt that is sufficiently small, to avoid wave interactions, one can define a global solution $\widetilde{\mathbf{U}}(x,t)$ in the strip $0 \leqslant x \leqslant L$, $t^n \leqslant t \leqslant t^{n+1}$ in terms of the local solutions as follows:

$$\widetilde{\mathbf{U}}(x,t) = \mathbf{U}_{i+1/2}(\overline{x}/\overline{t}), \quad x \in [x_i, x_{i+1}], \tag{2.11}$$

where the corespondance between the global (x,t) and local $(\overline{x},\overline{t})$ coordinates is given by:

$$\begin{cases} \overline{x} = x - x_{i+1/2}, & \overline{t} = t - t^n, \\ x \in [x_i, x_{i+1}], & t \in [t^n, t^{n+1}], \\ \overline{x} \in [-\Delta x/2, \Delta x/2], & \overline{t} \in [0, \Delta t]. \end{cases} \tag{2.12}$$

Having found a solution $\widetilde{\mathbf{U}}(x,t)$ in terms of solutions to local Riemann problems, the Godunov method advances the solution to a time $t^{n+1} = t^n + \Delta t$ by defining a new set of average values $\{\mathbf{U}^{n+1}\}$:

$$\mathbf{U}_i^{n+1} = \mathbf{U}_i^n + \frac{\Delta t}{\Delta x}[\mathbf{F}_{i-1/2} - \mathbf{F}_{i+1/2}], \tag{2.13}$$

with intercell numerical flux given again by the solution of the Riemann problem $\mathbf{F}_{i+1/2} = \mathbf{F}(\mathbf{U}_{i+1/2}(0))$ if the time step satisfies the condition

$$\Delta t \leqslant \frac{\Delta x}{S_{max}^n}. \tag{2.14}$$

Therefore, one usually defines the time step as

$$\Delta t = C\frac{\Delta x}{S^n_{max}} \quad \text{where} \quad 0 \leqslant C \leqslant 1. \tag{2.15}$$

For a domain [0,L] discretized into M computing cells, boundary conditions are needed at the boundaries $x = 0$ and $x = L$ as illustrated in Figure 2.3. Numerically, such boundary conditions are expected to provide numerical fluxes $\mathbf{F}_{1/2}$ and $\mathbf{F}_{M+1/2}$. These are required in order to apply the conservative formula (2.13) to update the extreme cells I_1 and I_M to the next time level $n + 1$. The boundary conditions consist in prescribing fictitious data values in the fictitious "ghost cells" I_0 and I_{M+1} adjacent to I_1 and I_M respectively. In this way, boundary Riemann problems RP($\mathbf{U}^n_0, \mathbf{U}^n_1$) and RP($\mathbf{U}^n_M, \mathbf{U}^n_{M+1}$) are solved and the corresponding Godunov fluxes $\mathbf{F}_{1/2}$ and $\mathbf{F}_{M+1/2}$ are computed. The imposition of boundary conditions is, fundamentally, a physical problem. Great care is required in their numerical implementation.

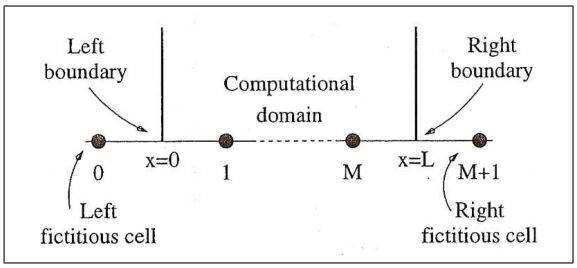

Figure 2.3: Boundary conditions. Fictitious "ghost cells" are created outside the computational domain. Credit: Toro [1999]

The Godunov original method is characterized by a large amount of numerical viscosity, that causes shocks to be smeared over several cells. In order to avoid this drawback, high order spatial polynomial reconstruction is often used. Nevertheless, as demonstrated by Godunov, a higher order spatial reconstruction creates spurious oscillations in the solution near shocks and discontinuities. Therefore, one must introduce some kind of control, like slope limiters that reduce the order of reconstruction to the first in cells where are present such features: in that manner the scheme preserves the monotonicity of the solution.

2.1.3 The Piecewise Parabolic Method

The Piecewise Parabolic Method (PPM) of Colella and Woodward [1984] is a higher-order extension of Godunov's method. The introduction of parabolae as the basic interpolation functions in a zone allows for a more accurate representation of smooth spatial gradients, as well as a steeper representation of captured discontinuities, particularly contact discontinuities.

Applying the notation used in the previous section, we rewrite the system of hyperbolic equations (2.1)-(2.3) as

$$\frac{\partial \mathbf{U}}{\partial t} + \frac{\partial (A\mathbf{F})}{\partial V} = -\frac{\partial \mathbf{H}}{\partial r} + \mathbf{G}, \tag{2.16}$$

where

$$\mathbf{U} = \begin{pmatrix} \rho \\ \rho u \\ e \end{pmatrix}, \quad \mathbf{F}(\mathbf{U}) = \begin{pmatrix} \rho u \\ \rho u^2 \\ u(e+p) \end{pmatrix}, \quad \mathbf{H}(\mathbf{U}) = \begin{pmatrix} 0 \\ p \\ 0 \end{pmatrix}, \quad \mathbf{G} = \begin{pmatrix} 0 \\ \rho g \\ \rho u g \end{pmatrix}. \tag{2.17}$$

Here $V(r) = r^{\alpha+1}/(\alpha+1)$ is a volume coordinate, $\mathrm{A(r)} = \mathrm{r}^\alpha$ and $g = -\partial\Phi/\partial r$.
The PPM scheme constructs a piecewise polynomial interpolating function $\mathbf{U}(r)$ satisfying

the condition (2.9) and constrained in such a way so that no new extrema appear in the interpolation function which do not already appear in the $\{\mathbf{U}_i^n\}$. $\mathbf{U}$ is given by a parabolic profile in each zone:

$$\mathbf{U}(r) = \mathbf{U}_{L,i} + \frac{r - r_{i-1/2}}{\Delta r_i}\left[\Delta\mathbf{U}_i + \mathbf{U}_{6,i}\left(1 - \frac{r - r_{i-1/2}}{\Delta r_i}\right)\right], \quad r_{i-1/2} \leqslant r \leqslant r_{i+1/2}, \tag{2.18}$$

where

$$\Delta\mathbf{U}_i = \mathbf{U}_{R,i} - \mathbf{U}_{L,i}, \quad \mathbf{U}_{6,i} = 6[\mathbf{U}_i^n - (\mathbf{U}_{L,i} + \mathbf{U}_{R,i})/2]. \tag{2.19}$$

$\mathbf{U}_{L,i}$ and $\mathbf{U}_{R,i}$ are calculated by first using an interpolation scheme to calculate $\mathbf{U}_{i+1/2}$, an approximation to the value of $\mathbf{U}$ at $r_{i+1/2}$, subject to the constraint that $\mathbf{U}_{i+1/2}$ does not fall out of range of values given by $\mathbf{U}_i$ and $\mathbf{U}_{i+1}$. The values $\mathbf{U}_{L,i}$ and $\mathbf{U}_{R,i}$ are further modified so that $\mathbf{U}(r)$ is a monotone function on each interval $(r_{i-1/2}, r_{i+1/2})$. It is this step that introduces discontinuities at zone edges.

To calculate $\mathbf{U}_{i+1/2}$ the indefinite integral of $\mathbf{U}$, $\mathcal{U}(r) = \int_r \mathbf{U}(r', t^n)dr'$, is interpolated through the points $(\mathcal{U}_{i+k+1/2}, r_{i+k+1/2})$, $k = 0, \pm1, \pm2$, and differentiated to obtain $\mathbf{U}_{i+1/2} = d\mathcal{U}/dr\,|_{i+1/2}$:

$$\begin{aligned}\mathbf{U}_{i+1/2} = \mathbf{U}_i^n &+ \frac{\Delta r_i}{\Delta r_i + \Delta r_{i+1}}(\mathbf{U}_{i+1}^n - \mathbf{U}_i^n) + \frac{1}{\sum_{k=-1}^{2}\Delta r_{i+k}} \\ &\times\left\{\frac{2\Delta r_{i+1}\Delta r_i}{\Delta r_i + \Delta r_{i+1}}\left[\frac{\Delta r_{i-1} + \Delta r_i}{2\Delta r_i + \Delta r_{i+1}} - \frac{\Delta r_{i+2} + \Delta r_{i+1}}{2\Delta r_{i+1} + \Delta r_i}\right](\mathbf{U}_{i+1}^n - \mathbf{U}_i^n)\right. \\ &\left. - \Delta r_i\frac{\Delta r_{i-1} + \Delta r_i}{2\Delta r_i + \Delta r_{i+1}}\delta_m\mathbf{U}_{i+1} + \Delta r_{i+1}\frac{\Delta r_{i+1} + \Delta r_{i+2}}{\Delta r_i + 2\Delta r_{i+1}}\delta_m\mathbf{U}_i\right\}.\end{aligned} \tag{2.20}$$

Here $\delta_m\mathbf{U}_i$ is the average slope of the parabola in the ith zone and is given by

$$\delta_m\mathbf{U}_i = \begin{cases}\min(|\,\delta\mathbf{U}_i\,|, 2\,|\,\mathbf{U}_{i+1}^n - \mathbf{U}_i^n\,|, 2\,|\,\mathbf{U}_i^n - \mathbf{U}_{i-1}^n\,|)\mathrm{sgn}(\delta\mathbf{U}_i), & \text{if } (\mathbf{U}_{i+1}^n - \mathbf{U}_i^n)(\mathbf{U}_i^n - \mathbf{U}_{i-1}^n) > 0, \\ 0, & \text{otherwise,}\end{cases} \tag{2.21}$$

with

$$\delta\mathbf{U}_i = \frac{\Delta r_i}{\Delta r_{i-1} + \Delta r_i + \Delta r_{i+1}}\left[\frac{2\Delta r_{i-1} + \Delta r_i}{\Delta r_{i+1} + \Delta r_i}(\mathbf{U}_{i+1}^n - \mathbf{U}_i^n) + \frac{\Delta r_i + 2\Delta r_{i+1}}{\Delta r_{i-1} + \Delta r_i}(\mathbf{U}_i^n - \mathbf{U}_{i-1}^n)\right]. \tag{2.22}$$

The value $\mathbf{U}_{i+1/2}$ is assigned to $\mathbf{U}_{L,i}$ and $\mathbf{U}_{R,i-1}$. In order to calculate the states for the Riemann problem, we define averages of the interpolation functions:

$$f_{i+1/2,L}^U(y) = \frac{1}{y}\int_{r_{i+1/2}-y}^{r_{i+1/2}}\mathbf{U}(r)dr = \mathbf{U}_{R,i} - \frac{y}{2\Delta r_i}\left[\Delta\mathbf{U}_i - \left(1 - \frac{2y}{3\Delta r_i}\right)\mathbf{U}_{6,i}\right], \tag{2.23}$$

$$f_{i+1/2,R}^U(y) = \frac{1}{y}\int_{r_{i+1/2}}^{r_{i+1/2}+y}\mathbf{U}(r)dr = \mathbf{U}_{L,i+1} + \frac{y}{2\Delta r_{i+1}}\left[\Delta\mathbf{U}_{i+1} + \left(1 - \frac{2y}{3\Delta r_{i+1}}\right)\mathbf{U}_{6,i+1}\right]. \tag{2.24}$$

Using these interpolation functions, the first guess at the effective left and right states for the Riemann problem is constructed:

$$\begin{aligned}\widetilde{\mathbf{U}}_{i+1/2,L} &= f_{i+1/2,L}^U[V_{i+1/2} - V(\tilde{r}_{i+1/2,L})], \\ \tilde{r}_{i+1/2,L} &= r_{i+1/2} - \max(0, \Delta t(u_i^n + c_i^n)), \\ \widetilde{\mathbf{U}}_{i+1/2,R} &= f_{i+1/2,R}^U[V(\tilde{r}_{i+1/2,R}) - V_{i+1/2}], \\ \tilde{r}_{i+1/2,R} &= r_{i+1/2} + \max(0, -\Delta t(u_{i+1}^n - c_{i+1}^n),\end{aligned} \tag{2.25}$$

where c is the speed of sound, defined by

$$c^2 = \tau^2(pp_e - p_\tau), \quad \tau = 1/\rho. \tag{2.26}$$

These initial guesses are corrected by solving the equations of gas dynamics in characteristic form,

$$\frac{\partial \mathbf{V}}{\partial t} + \mathbf{A}\frac{\partial \mathbf{V}}{\partial r} + \mathbf{G} = 0, \tag{2.27}$$

with

$$\mathbf{V} = \begin{pmatrix} \rho \\ u \\ p \end{pmatrix}, \quad \mathbf{A}(\mathbf{V}) = \begin{pmatrix} u & \rho & 0 \\ 0 & u & 1/\rho \\ 0 & \rho c^2 & u \end{pmatrix}, \quad \mathbf{G}(\mathbf{V}, r, t) = \begin{pmatrix} \alpha\rho \mathrm{u}/\mathrm{r} \\ -g \\ \alpha \mathrm{c}^2 \rho \mathrm{u}/\mathrm{r} \end{pmatrix}, \tag{2.28}$$

yielding the following states for the primitive variables ρ, u and p:

$$\begin{aligned} \rho_{i+1/2,S} &= \left(\frac{1}{\tilde{\rho}_{i+1/2,S}} - \sum_{m=0,+,-} \beta^m_{i+1/2,S} \right)^{-1}, \\ u_{i+1/2,S} &= \tilde{u}_{i+1/2,S} + \widetilde{C}_{i+1/2,S}(\beta^+_{i+1/2,S} - \beta^-_{i+1/2,S}), \\ p_{i+1/2,S} &= \tilde{p}_{i+1/2,S} + \widetilde{C}^2_{i+1/2,S}(\beta^+_{i+1/2,S} + \beta^-_{i+1/2,S}). \end{aligned} \tag{2.29}$$

Here $\widetilde{C}^2_{i+1/2,S} = \Gamma \tilde{p}_{i+1/2,S}\tilde{\rho}_{i+1/2,S}$ and S = L, R. We also have

$$\begin{aligned} \beta^m_{i+1/2,L} &= 0 \text{ if } \lambda_m(\mathbf{U}^n_i) \leqslant 0; \quad \beta^m_{i+1/2,R} = 0 \text{ if } \lambda_m(\mathbf{U}^n_{i+1}) \geqslant 0, \\ \beta^\pm_{i+1/2,S} &= \mp \frac{1}{2\widetilde{C}_{i+1/2,S}} \left[(\tilde{u}_{i+1/2,S} - u^\pm_{i+1/2,S}) \pm \frac{(\tilde{p}_{i+1/2,S} - p^\pm_{i+1/2,S})}{\widetilde{C}_{i+1/2,S}}, \right. \\ &\qquad \left. \pm \Delta t \left(\frac{a u^+_{i+1/2,S} c^\pm_{i+1/2,S}}{r^\pm_{i+1/2,S}} \mp g^\pm_{i+1/2,S} \right) \right] \\ \beta^0_{i+1/2,S} &= \left(\frac{(\tilde{p}_{i+1/2,S} - p^0_{i+1/2,S})}{\widetilde{C}^2_{i+1/2,S}} + \frac{1}{\tilde{\rho}_{i+1/2,S}} - \frac{1}{\rho^0_{i+1/2,S}} \right). \end{aligned} \tag{2.30}$$

Γ is defined, in analogy with the special case of polytropic gases, as

$$\Gamma(\rho, p) \equiv \frac{\rho c^2}{p}. \tag{2.31}$$

For polytropic gases this is equivalent to

$$\gamma(\rho, p) \equiv \frac{p}{e\rho} + 1, \tag{2.32}$$

but this is not true in general. To solve the Riemann problem in the case of a general equation of state, several calls to the equation of state routine would be needed for each time step. To avoid this, we employ the Riemann solver of Colella and Glatz [1985], which is based on a local parametrization of the equation of state.

The idea is that the equation of state can be expressed locally in terms of γ. For the purpose of computing numerical fluxes, γ will be treated as a separate dependent variable; the solution of characteristic equations and Riemann problems will necessarily involve an approximate computation of the jump in γ across such waves. This approach, albeit crude, is justified by the fact that γ is a slowly varying function of the thermodynamic variables for real gases: although ρ, p, e may vary over many orders of magnitude, γ stays in the range $1 \leqslant \gamma \leqslant 5/3$.

Since γ is a function of the thermodynamic state of the fluid, it is natural to consider its dynamics along the streamline characteristic, which we parametrize by σ_0. By definition,

$$\frac{d\gamma}{d\sigma_0} = \frac{\partial\gamma}{\partial\tau}\frac{d\tau}{d\sigma_0} + \frac{d\gamma}{de}\frac{\partial e}{\partial\sigma_0}. \tag{2.33}$$

Using (2.31), (2.32), (2.26) and the first law of thermodynamics, this becomes

$$\frac{d\gamma}{d\sigma_0} = \left(1 - \frac{\gamma}{\Gamma}\right)(\gamma - 1)\frac{1}{p}\frac{dp}{d\sigma_0}. \tag{2.34}$$

In general, it is not possible to specify how γ behaves across a discontinuity without solving the full Rankine-Hugoniot conditions. However, if the jump is not too large, then the jump conditions for γ are well approximated by an integrated form of the characteristic equation (2.34):

$$\gamma_* - \gamma_0 \approx \left(1 - \frac{\overline{\gamma}}{\overline{\Gamma}}\right)(\overline{\gamma} - 1)\frac{1}{\overline{p}}(p_* - p_0) + O(p_* - p_0)^3, \tag{2.35}$$

where $\overline{\gamma}$, $\overline{\Gamma}$ and $\overline{p}$ are suitably centered across the jump.

The above local model leads to the following approximate solution to the Riemann problem. For shock tube initial data, the solution to the Riemann problem is illustrated in Fig. 2.4: the backward facing wave $(\mathbf{U}_{*,L}, \mathbf{U}_L)$ and the forward facing wave $(\mathbf{U}_{*,R}, \mathbf{U}_R)$ may be either shocks or rarefaction waves, while the center wave $(\mathbf{U}_{*,L}, \mathbf{U}_{*,R})$ must be a contact wave across which there is no pressure or velocity jump (i.e. $p_{*,L} = p_{*,R}$ and $u_{*,L} = u_{*,R}$). Thus, the main step in solving the Riemann problem is the computation of the pair (p_*, u_*) which is the unique solution to the jump conditions across the outermost waves of the Riemann fan.

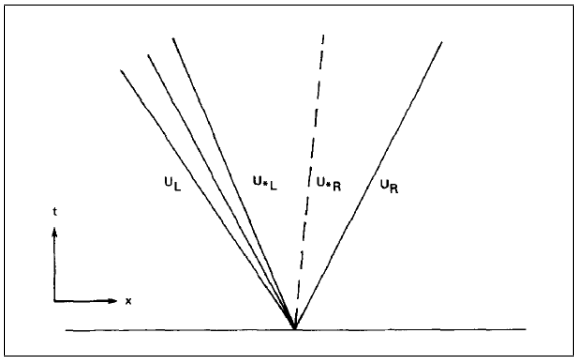

Figure 2.4: The solution of the Riemann problem in phisical space. Credit: Colella and Woodward [1984]

For either a shock or a rarefaction wave, the postwave state is uniquely determined by the prewave state and p_*. In particular the postwave velocity $u_{*,S}$ can be defined as a function of p_* and $\mathbf{U}_S$. The mean Lagrangian wave speeds are defined by

$$W_S = \begin{cases} \dfrac{|p_* - p_S|}{|u_{*,S} - u_S|} & \text{if } u_{*,S} \neq u_S \\ C_S = \rho_S c_S & \text{if } u_{*,S} = u_S. \end{cases} \tag{2.36}$$

At the solution, $u_{*,L} = u_{*,R} = u_*$. We then solve the equation

$$u_{*,L}(p_*) - u_{*,R}(p_*) = 0 \tag{2.37}$$

by applying the secant method:

$$
\begin{aligned}
u^k_{*,S} &= u_S \pm \frac{p^k_* - p_S}{W^k_S} \\
(W^k_S)^2 &= \frac{(p_* - p_S)[p_* + (\gamma_{*,S} - 1)(p_* + p_S)/2]}{p_* \tau_S - \frac{\gamma_{*,S}-1}{\gamma_S - 1} p_S \tau_S} \\
p^{k+1}_* &= p^k_* - (u^k_{*,R} - u^k_{*,L}) \left[\frac{|p^k_* - p^{k-1}_*|}{|u^k_{*,L} - u^{k-1}_{*,L}| + |u^k_{*,R} - u^{k-1}_{*,R}|} \right]
\end{aligned} \tag{2.38}
$$

for k=1,2,... Here γ_* is calculated from Eq. (2.35) with $\overline{\gamma} = (\gamma_L + \gamma_R)/2$, $\overline{\Gamma} = (\Gamma_L + \Gamma_R)/2$ and $\overline{p} = p_*$, and the combination of (S,±) are to be taken as either (L,-) or (R,+). The first two guesses used to start the iteration are obtained using Godunov's scheme.

The final conservative difference step is given by:

$$
\rho^{n+1}_i = \rho^n_i + \Delta t \left[\frac{r^a_{i-1/2} \rho_{*,i-1/2} u_{*,i-1/2} - r^a_{i+1/2} \rho_{*,i+1/2} u_{*,i+1/2}}{\Delta V_i} \right] \tag{2.39}
$$

$$
\begin{aligned}
u^{n+1}_i = \frac{u^n_i \rho^n_i}{\rho^{n+1}_i} + \Delta t \Bigg[& \frac{r^a_{i-1/2} \rho_{*,i-1/2} u^2_{*,i-1/2} - r^a_{i+1/2} \rho_{*,i+1/2} u^2_{*,i+1/2}}{\Delta V_i} \\
& + \frac{p_{*,i-1/2} - p_{*,i+1/2}}{\Delta r_i} + \frac{\rho^n_i g^n_i + \rho^{n+1}_i g^{n+1}_i}{2} \Bigg]
\end{aligned} \tag{2.40}
$$

$$
\begin{aligned}
e^{n+1}_i = e^n_i + \Delta t \Bigg[& \frac{r^a_{i-1/2} u_{*,i-1/2} (e_{*,i-1/2} + p_{*,i-1/2}) - r^a_{i+1/2} u_{*,i+1/2} (e_{*,i+1/2} + p_{*,i+1/2})}{\Delta V_i} \\
& + \frac{\rho^n_i u^n_i g^n_i + \rho^{n+1}_i u^{n+1}_i g^{n+1}_i}{2} \Bigg]
\end{aligned} \tag{2.41}
$$

2.2 Gravity

Relativistic effects are taken into account in our Newtonian hydrodynamics code by using an "effective relativistic gravitational potential" [Rampp and Janka, 2002]. The simulations presented in this thesis employ the improved version of this potential described by Marek et al. [2006] , who found excellent agreement with fully relativistic calculations during core collapse and the first several hundred milliseconds after core bounce (tests for the later neutrino-wind phase can be found in Arcones et al. [2007]).
According to Rampp and Janka [2002] and Marek et al. [2006], the effects of general relativity in a Newtonian hydrodynamics code can be approximated by replacing the Newtonian gravitational potential by a modified Tolman-Oppenheimer-Volkoff (TOV) potential:

$$\Phi_{TOV}(r) = -4\pi G \int_r^\infty \frac{dr'}{r'^2}\left[\frac{m_{TOV}}{4\pi} + \frac{r'^3(p+p_\upsilon)}{c^2}\right]\frac{1}{\Gamma^2}\left(\frac{\rho c^2 + e + p}{\rho c^2}\right), \tag{2.42}$$

where ρ is the rest-mass density, $e = \rho\epsilon$ is the internal energy density with ϵ being the specific internal energy, p is the gas pressure and p_υ is the neutrino pressure.
The "modified TOV mass" m_{TOV} is given by

$$m_{TOV}(r) = 4\pi \int_0^r dr'\, r'^2\left(\rho + \frac{e+E}{c^2} + \frac{\upsilon F}{\Gamma c^2}\right)\Gamma, \tag{2.43}$$

where E and F are the the neutrino energy density and the neutrino flux, respectively.
The fluid velocity υ is identified with the local radial velocity calculated by the Newtonian code and the metric function Γ is given by

$$\Gamma = \sqrt{1 + \frac{\upsilon^2}{c^2} - \frac{2Gm_{TOV}}{rc^2}}. \tag{2.44}$$

The extra factor Γ in Eq. (2.43) compared to the relativistic definition of the TOV mass enters the mass integral for reasons of consistency with the Newtonian hydrodynamics equations and accounts for the fact that in the Newtonian code there is no distinction between local proper volume and coordinate volume (for more details, see Marek et al. [2006]).

There is, however, an important difference of our calculations compared to those performed by Marek et al. [2006]. While the latter included the whole neutron star down to the center, the use of the inner grid boundary at a radius $R_{ib} > 0$ in the present work prevents the evaluation of the integral in Eq. (2.43) within the neutron star core. We solve this problem by starting our calculations with a given value of the modified TOV mass of the core at t = 0, $m_{TOV}(R_{ib}, 0)$, which was provided to us as part of the data set for the initial conditions of our simulations. For t > 0 we then approximately evolve the modified TOV mass according to the expression

$$m_{TOV}(R_{ib}, t) = m_{TOV}(R_{ib}, 0) - \int_0^t L_\upsilon^{ib}(t')dt' - \int_0^t 4\pi R_{ib}^2(t')P_{ib}(t')\frac{dR_{ib}}{dt'}dt', \tag{2.45}$$

where the second term on the right hand side yields the energy loss from the neutron star core by the total neutrino luminosity at the inner boundary, $L_\upsilon^{ib}(t)$, and the last term represents the compression (PdV) work done on the core at the contracting inner boundary. The total modified TOV-mass at radius r is thus given by

$$m_{TOV}(r) = m_{TOV}(R_{ib}, t) + 4\pi \int_0^r dr'\, r'^2\left(\rho + \frac{e+E}{c^2} + \frac{\upsilon F}{\Gamma c^2}\right)\Gamma. \tag{2.46}$$

2.3 Neutrino Transport

The algorithm for solving the equation of radiation transport for neutrinos is the one developed by Scheck et al. [2006]. Here we will summarize the procedure adopted; for a more detailed description, see Appendix D in Scheck et al. [2006].
We start from the equation of radiation transport in spherical symmetry

$$\frac{1}{c}\frac{\partial}{\partial t}I + \mu\frac{\partial}{\partial r}I + \frac{1-\mu^2}{r}\frac{\partial}{\partial \mu}I = S, \tag{2.47}$$

where $I = I(t, r, \epsilon, \mu)$ is the specific intensity, $S = S(t, r, \epsilon, \mu)$ is the source function, ϵ is the neutrino energy, $\mu = \cos\vartheta$ and ϑ is the angle between radiation propagation and radial direction. Solid angle integration yields the zeroth angular moment equation,

$$\frac{1}{c}\frac{\partial}{\partial t}J + \frac{1}{r^2}\frac{\partial}{\partial r}(r^2 H) = S^{(0)} \equiv \frac{1}{2}\int_{-1}^{+1} d\mu S, \tag{2.48}$$

with $\{J, H\}(t, r, \epsilon) = \frac{1}{2}\int_{-1}^{+1} d\mu \mu^{\{0,1\}} I(t, r, \epsilon, \mu)$. Integration over energy leads to

$$\frac{\partial}{\partial t}E + \frac{1}{r^2}\frac{\partial}{\partial r}(r^2 F) = \mathcal{Q}^+ - \mathcal{Q}^-, \tag{2.49}$$

with $\{E, F\}(t, r) = 4\pi\int_0^\infty d\epsilon\{J/c, H\}(t, r, \epsilon)$ being energy density and energy flux, respectively. The source term has been split in an emission rate $\mathcal{Q}^+$ and an absorption rate $\mathcal{Q}^- = \kappa_a cE$, which is proportional to the energy density. The flux factor is defined as the ratio of flux to energy density,

$$f(r, t) = F(r, t)/cE(r, t). \tag{2.50}$$

In neutrino transport simulations solving the full Boltzmann equation (see e.g. Buras et al. [2003], Buras et al. [2006a], Buras et al. [2006b]) this quantity shows only little short-time variability during most phases of the supernova evolution. Therefore $\partial f/\partial t = 0$ is an acceptably good approximation. With $L = 4\pi r^2 F = 4\pi r^2 fcE$ one can now rewrite Eq. (2.49) as

$$\frac{\partial}{\partial t}L + c_{eff}\frac{\partial}{\partial r}L = 4\pi r^2 c_{eff}(\mathcal{Q}^+ - \mathcal{Q}^-), \tag{2.51}$$

where an effective speed of neutrino propagation has been introduced as $c_{eff} = cf$. Provided c_{eff} were known, the solution of Eq. (2.51) requires considerably less effort than the numerical integration of Eq. (2.47). For vanishing source terms $\mathcal{Q}^+$ and $\mathcal{Q}^-$ the neutrino energy or number density is just advected along characteristics $r(t) = r_0 + c_{eff}t$. Although c_{eff} depends through $f(r, t)$ on the solution of the transport problem (Eq. (2.50)), neutrino transport calculations in the neutrino-decoupling layer of forming neutron stars reveal that it can be well fitted by a r-dependent function which depends on the steepness of the density profile [see Janka, 1991]:

$$f_\nu(\tau_\nu) = \begin{cases} \dfrac{(1+D)/2}{1+(1+D)(1-D^2)^{(n+1)/2}}, & \text{if } \tau_\nu < \tau_{\nu,1}, \\ (\tau_\nu/\tau_{\nu,1})^m/4, & \text{if } \tau_\nu > \tau_{\nu,1}. \end{cases} \tag{2.52}$$

Here $\nu \in \{\nu_e, \bar{\nu}_e, \nu_x\}$, $D = \sqrt{1-(R_\nu/r)^2}$, τ_ν is the optical depth, the neutrinosphere radius R_ν is defined by $\tau_\nu(R_\nu) = \tau_{\nu,1} = 1.1$, the power-law index m is chosen such that $f_\nu(10) = 1/25$, and n is defined by a local power-law fit of the density profile around the neutrinosphere, $\rho(r) \propto r^{-n}$.

Assuming further that the (medium dependent) coefficients $\mathcal{Q}^+$ and $\tilde{\kappa} \equiv \kappa_a/f = 4\pi r^2 \mathcal{Q}/L$ are constant between two points (r, t) and (r^*, t^*), which are connected by a characteristic line, i.e.,

$$r^* = r - c_{eff}(t - t^*), \tag{2.53}$$

Eq. (2.51) can be integrated analitically to yield

$$L(r,t) = L(r^*,t^*)\mathrm{e}^{-\tilde{\kappa}c_{eff}(t-t^*)} + \frac{4\pi\mathcal{Q}^+}{\tilde{\kappa}^3}\left\{\left[1-\mathrm{e}^{-\tilde{\kappa}c_{eff}(t-t^*)}\right]\left[1+(\tilde{\kappa}r^*-1)^2\right]\right.$$
$$\left. + \tilde{\kappa}c_{eff}(t-t^*)\left[2\tilde{\kappa}r^* + \tilde{\kappa}c_{eff}(t-t^*) - 2\right]\right\}, \tag{2.54}$$

where $L(r, t)$ and $L(r^*, t^*)$ are the luminosity values at both ends of the characteristic line. We use Eq. (2.54) to construct a numerical scheme to solve Eq. (2.51) in the general case: we assume that the luminosity is known at the cell interfaces of a one-dimensional radial grid for a time t^{n-1}, and that the cell-averaged values of the quantities needed to compute the emission rate $\mathcal{Q}^+$ and absorption coefficient $\tilde{\kappa}$ are also known for that time. As a further simplification we do not allow neutrinos to propagate in negative radial direction (actually this is granted by defining a non-negative function for the flux factor). Then the luminosities at $t^n = t^{n1} + \Delta t$ for each zone interface (starting at the innermost zone) can be computed using Eq. (2.54). In doing so we have to distinguish between two cases (see Fig. 2.5): if $c_{eff}\Delta t > \Delta r$, we can use point A as the starting point of the integration, $(r^*, t^*) = (r_{i-1}, t_A)$. The luminosity at this point is derived from a linear interpolation between $L(r_{i-1}, t^{n-1})$ and $L(r_{i1}, t^n)$ (which is already known, as we are integrating outwards). If $c_{eff}\Delta t \leqslant \Delta r$, we use point B, the luminosity at this point being given by a linear interpolation between $L(r_{i-1}, t^{n-1})$ and $L(r_i, t^{n-1})$.

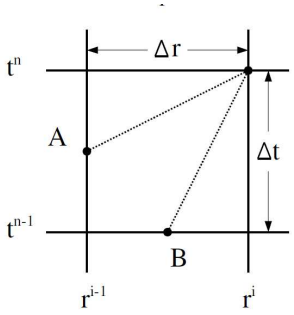

Figure 2.5: The solution at (r_i, t^n) is computed from the data at a point (r^*, t^*) located on the same characteristic line. Depending on the grid spacing, Δr, the time step, Δt, and the effective speed of neutrino propagation, c_{eff}, either point A or point B must be used. The solution there can be obtained by interpolation in time or space, respectively. Credit: Scheck et al. [2006]

For time integration we use a predictor-corrector method: the transport routine is called two times. In the first (predictor) step the luminosities, emission rates and absorption coefficients of the last time step $[L^{n-1}, \mathcal{Q}^{n-1}, \kappa^{n-1}]$ are used to compute preliminary values $(\widetilde{\mathcal{Q}}^n, \tilde{\kappa}^n)$ for the neutrino-medium coupling at the next time level. In the second (corrector) step the final values $[L^n, \mathcal{Q}^n, \kappa^n]$ are calculated using $[L^{n-1}, (\mathcal{Q}^{n-1} + \widetilde{\mathcal{Q}}^n)/2, (\kappa^{n-1} + \tilde{\kappa}^n)]$ as input.

Equation (2.51) is solved not only for the energy luminosity $L = L_e$, but also for the number luminosity $L_n = 4\pi r^2 F_n = 4\pi r^2 fcn$ (n is the particle density and f is assumed to be

the same flux factor as for the energy transport). Furthermore the equation has to be integrated for three neutrino types, ν_e, $\bar{\nu}_e$, and ν_x (the latter denoting ν_μ, $\bar{\nu}_\mu$, ν_τ, and $\bar{\nu}_\tau$, which are treated identically).

To integrate Eq. (2.54) outwards, time-dependent boundary conditions are required for the luminosities $L_{e,\nu}$ and $L_{n,\nu}$, where $\nu = \nu_e, \bar{\nu}_e, \nu_x$.
Scheck et al. [2006] assumed $L_{e,\nu}$ and $L_{n,\nu}$ to be constant for a time interval of typically 1 s, and to decay subsequently with a power-law dependence in time. For the simulations presented in this paper, we have developed a simple, analytic two-zone model for the cooling of the neutron star, based on the physical constraints of energy conservation and the virial theorem, which is presented in Section 2.3.1.

For treating the spectral dependence, we make the assumption that the neutrino phase space distribution function can be factorised into a product of an angle-dependent function and an energy-dependent term, which we assume to be of Fermi-Dirac shape. This is certainly a problematic simplification in view of the fact that the neutrino interactions with the stellar medium are strongly energy-dependent. Nevertheless, this neutrino transport treatment represents a practical approximation which is able to reproduce basic features of more detailed transport solutions and yields agreement with those even beyond the purely qualitative level [see Scheck et al., 2006].

For calculating the neutrino-matter interaction rates the reactions taken into account are: charged-current processes with neutrons and protons, thermal electron-positron pair creation, annihilation and neutrino scattering off nuclei, nucleons, electrons and positrons. The equations for the reaction rates and neutrino source terms can be found in appendix D.5 and D.6 of Scheck et al. [2006].

2.3.1 Boundary Condition

In our simulations we replace the inner core of the neutron star (usually roughly 1.1 $M_\odot$ of baryonic matter) by an inner Lagrangian boundary of our grid, whose prescribed contraction is supposed to mimic the shrinking of the nascent neutron star as it loses energy and lepton number by neutrino emission. Using this inner boundary, which typically is located at a ν_e optical depth of more than 100 and a density of $\rho_{ib} \gtrsim 10^{13}$ g/cm^3, allows us to apply the simple neutrino transport approximation described above. Three parameters serve us to describe the motion of the inner boundary: R^i_{ib}, R^f_{ib}, and t_0. The initial radius R^i_{ib} is the radius of the inner core that we chose to excise from the postbounce models we start our simulations from, R^f_{ib} is the final radius of this core for time $t \to \infty$, and t_0 is the timescale of an exponential contraction according to the expression

$$R_{ib}(t) = R^f_{ib} + (R^i_{ib} - R^f_{ib})e^{-t/t_0}. \tag{2.55}$$

Because of the contraction and postbounce accretion of the proto-neutron star, the density and optical depth in the layers near the inner grid boundary can increase to such large values that the application of our transport approximation becomes inefficient by the required very fine zoning, and the equation of state fails to describe the dense stellar matter. For this reason, we have to set a rather large final radius and rather slow contraction of the neutron star: we typically choose R^f_{ib}=20 km and t_0=0.4, which yield an evolution of our inner grid boundary similar to the "standard boundary contraction" of Scheck et al. [2006]. We have then developed a simple analitical model for the neutrino emission of the proto-neutron star by considering a core that is, in general, different from the one excised from the computational grid.

Figure 2.6 shows a simple sketch of our model: an inner core of radius R_c (in general different from the radius of the inner grid boundary) and mass M_c accretes the mass contained in a thick layer around it and emits neutrinos. This core is also shrinking in time to mimic the contraction of the PNS.

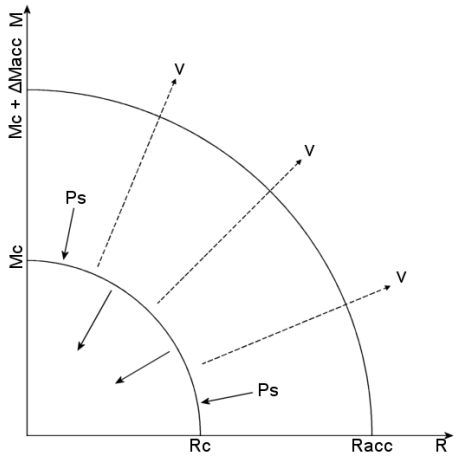

Figure 2.6: Model for the neutrino emission from the inner boundary.

Since the core is in hydrostatic equilibrium we can apply the virial theorem, taking into account by the surface term S the fact that the pressure P_s at radius R_c is not zero:

$$E_g + 3(\Gamma - 1)E_i + S = 0, \quad \text{with} \quad S = -\int_{core} \nabla \cdot (\mathbf{x}P) d^3x = -4\pi R_c^3 P_s. \tag{2.56}$$

The total energy of the inner core is then:

$$E_{tot} = E_g + E_i = \frac{3\Gamma - 4}{3(\Gamma - 1)} E_g - \frac{S}{3(\Gamma - 1)}, \quad \text{with} \quad E_g \simeq -\frac{2}{5}\frac{GM_c^2}{R_c} \tag{2.57}$$

for a homogeneus core inside R_c.
The energy of the core evolves with time because of neutrino losses and of PdV work done on its surface:

$$\frac{dE_{tot}}{dt} = \dot{E}_{tot} = -L^c_{\nu,tot} - P_s \frac{dV_c}{dt} = -L^c_{\nu,tot} - 4\pi P_s R_c^2 \dot{R}_c = -L^c_{\nu,tot} + S\frac{\dot{R}_c}{R_c}. \tag{2.58}$$

In order to use this equation to coin a formula for the neutrino luminosity as a function of time we need to know the surface pressure P_s. Since we use a hydrodynamical inner boundary that is in general bigger than the core radius R_c we cannot get this value from the code, and thus have developed an estimate.
If we consider a region in the accretion layer between inner core (with mass M_c and radius R_c) and outer radius r_{acc}, containing the mass Δm_{acc}, pressure equilibrium gives:

$$\frac{dP}{dm} = -\frac{GM}{4\pi r^4} \quad \Rightarrow \quad \frac{P_{acc} - P_s}{\Delta m_{acc}} \simeq -a\frac{GM_c}{4\pi R_c^4}, \tag{2.59}$$

where $0 < a \leqslant 1$. Since the pressure gradient is very steep, $P_{acc} \ll P_s$ and:

$$P_s \simeq a\frac{GM_c \Delta m_{acc}}{4\pi R_c^4}, \quad S = -4\pi R_c^3 P_s \simeq -a\frac{GM_c \Delta m_{acc}}{R_c}. \tag{2.60}$$

We can now solve equation (2.58) for the neutrino luminosity:

$$L^c_{\nu,tot} = \dot{E}_{tot} + S\frac{\dot{R}_c}{R_c} = \frac{3\Gamma - 4}{3(\Gamma - 1)}\dot{E}_g - \frac{\dot{S}}{3(\Gamma - 1)} + S\frac{\dot{R}_c}{R_c}, \tag{2.61}$$

where we have assumed $\partial\Gamma/\partial t = 0$. Applying Eq. (2.60) we obtain

$$L^c_{\nu,tot} = -\frac{2}{5}\frac{3\Gamma - 4}{3(\Gamma - 1)}\frac{GM_c^2\dot{R}_c}{R_c^2} - \frac{3\Gamma - 4}{3(\Gamma - 1)}\frac{aGM_c\Delta m_{acc}\dot{R}_c}{R_c^2} - \frac{aGM_c\Delta\dot{m}_{acc}}{3(\Gamma - 1)R_c}. \tag{2.62}$$

The total neutrino luminosity is then distributed to the different neutrino species:

$$L_{e,\nu_e}(R_{ib}, t) = L^c_{\nu,tot}K_{\nu_e}, \tag{2.63}$$

$$L_{e,\bar{\nu}_e}(R_{ib}, t) = L^c_{\nu,tot}K_{\bar{\nu}_e}, \tag{2.64}$$

$$L_{e,\nu_x}(R_{ib}, t) = L^c_{\nu,tot}K_{\nu_x}, \tag{2.65}$$

where the constants K_ν denote the fractional contributions of the individual luminosities to the total neutrino luminosity. They fulfill the requirement

$$K_{\nu_e} + K_{\bar{\nu}_e} + 4K_{\nu_x} = 1. \tag{2.66}$$

We also prescribe the mean energies of neutrinos entering the computational grid at the inner boundary, $\langle\epsilon_\nu\rangle^{ib}$, with $\nu \in \{\nu_e, \bar{\nu}_e, \nu_x\}$. Since the inner boundary is usually located in the optically thick region, we can assume that neutrinos and matter are in thermodynamic equilibrium, thus:

$$\langle\epsilon_\nu\rangle^{ib} = k_B T_\nu^{ib}\mathcal{F}_3(\eta_\nu^{ib})/\mathcal{F}_2(\eta_\nu^{ib}) = k_B T^{ib}\mathcal{F}_3(\eta_\nu^{ib})/\mathcal{F}_2(\eta_\nu^{ib}), \tag{2.67}$$

with the Fermi integrals defined as

$$\mathcal{F}_n(\eta) = \int_0^\infty x^n f_{FD}(x, \eta)dx, \quad f_{FD}(x, \eta) = \frac{1}{1 + \exp(x - \eta)}. \tag{2.68}$$

We have explored two choices for η_ν^{ib}. Since we are assuming thermodynamical equilibirum, the first choice was to set them equal to the equilibrium values:

$$\eta_{eq,\nu_e} = (\mu_e + \mu_p - \mu_n)/k_B T, \quad \eta_{eq,\bar{\nu}_e} = -\eta_{eq,\nu_e}, \quad \eta_{eq,\nu_x} = 0, \tag{2.69}$$

[see Janka, 1991]. However, as the temperature and density in the inner boundary increase, the equilibrium degeneracy parameters for ν_e and $\bar{\nu}_e$ approach zero [see e.g. Shen et al., 2011], so we have also tried setting $\eta_{\nu_e} = \eta_{\bar{\nu}_e} = 0$. We have found minimal difference in the fluxes and mean energies of the neutrinos emerging from the neutron star depending on the choice of η_ν, thus we have decided to set $\eta_{\nu_e} = \eta_{\bar{\nu}_e} = \eta_{\nu_x} = 0$ for simplicity.

With this choices for the neutrino mean energies, we can calculate the total lepton number lost by the neutron star core until time t:

$$\Delta Y_{e,core} = \frac{1}{N_{b,core}}\int_0^t \left(\frac{L_{e,\nu_e}(R_{ib}, t')}{\langle\epsilon_{\nu_e}\rangle} - \frac{L_{e,\bar{\nu}_e}(R_{ib}, t')}{\langle\epsilon_{\bar{\nu}_e}\rangle}\right)dt' = \frac{(K_{\nu_e} - K_{\bar{\nu}_e})\mathcal{F}_2(0)}{k_B N_{b,core}\mathcal{F}_3(0)}\int_0^t \frac{L^c_{\nu,core}(t')}{T^{ib}(t')}dt'. \tag{2.70}$$

This constrains our choice of K_{ν_e} and $K_{\bar{\nu}_e}$. Since $\Delta Y_{e,core}$ must be positive, $K_{\nu_e} > K_{\bar{\nu}_e}$. We have found good agreement with detailed simulations by setting $K_{\nu_e} = 0.20$ and $K_{\bar{\nu}_e} = 0.15$. K_{ν_x} follows from Eq. (2.66).

We have some freedom in choosing the parameters appearing in Eq. (2.62).
$\mathbf{\Gamma}$, the adiabatic index, depends on the still unknown equation of state for dense matter. The assumption $\partial\Gamma/\partial t = 0$ is rather crude, since this value varies between 1.5 and 3 [see Shen et al., 2011, Lattimer and Swesty, 1991], however we have found that increasing Γ

from 2 to 3 results in an increase of less than 10% of the emerging neutrino luminosities, thus we expect that the error introduced by assuming Γ=const. is of the same order of magnitude.

For the calculation of $\mathbf{\Delta m_{acc}}$ we prescribe $\mathbf{r_{acc}}$ by choosing the radius at which $\rho = 10^{10}$ g/cm^3, which happens typically around $\sim 2 \div 3 R_{ib}$. Since both the pressure and the density gradients in the core are very steep, this is usually sufficient to have $P_{acc} \ll P_S$.

a is a scaling parameter and should have values between 0 and 1. The role of a in Eq. (2.62) is to weight the contribution of accretion luminosity on the total luminosity emitted from the core. If $a \sim 1$, the amount of energy emitted in neutrinos will be dominated by accretion, thus, if the remaining parameters are kept constant, it will be greater for more massive stars. The other limit, $a \sim 0$, means that the energy released in neutrinos depends only on the model used for the core and, if this model is the same for different progenitors, it will be constant for all progenitors. We have tested different values of a ranging from 0.5 to 1, and we find that they can lead to differences of up to ~30% on the explosion energy (depending on the progenitor considered), while other observables considered like the remnant mass and the mass of nickel ejected vary much less as a function of a (not more than 10%). We have thus decided to adopt intermediate values, usually 0.5 or 0.6.

Finally, we need to prescribe the time behaviour of $\mathbf{R_c}$ (and consequently of $L^c_{\nu,core}$). We have tested three different functional forms for this parameter: the same function used for the contraction of the inner grid boundary,

$$R_c(t) = R_{c,fin} + (R_{c,ini} - R_{c,fin}) e^{-t/t_0}, \tag{2.71}$$

a similar function but with two exponentials,

$$R_c(t) = R_{c,fin} + \frac{1}{2}(R_{c,ini} - R_{c,fin})(e^{-t/t_1} + e^{-t/t_2}), \tag{2.72}$$

and a power-law function

$$R_c(t) = R_{c,fin} + (R_{c,ini} - R_{c,fin}) \left(\frac{t + t_L}{t_L} \right)^p, \tag{2.73}$$

where $p < 0$ and t_L=1 s, in order to have $R_c(0) = R_{c,ini}$.
We found that using an exponential law for the time evolution of the core radius leads to a very quick decline of the neutrino luminosities, which in turn means that the total energy emitted in neutrinos is too low (a "standard" neutron star with a mass of about 1.4 $M_\odot$ should radiate roughly $3 \cdot 10^{53}$ erg in neutrinos of all flavours), while we get more reasonable values with the power-law function. Hence we prescribe the time evolution of R_c according to Eq. (2.73), where the power p is usually $-3.5 \leqslant p \leqslant -2.5$.
$R_{c,ini}$ is set equal to the initial inner boundary radius, R^i_{ib}, thus M_c is equal to the mass of the excised core (tipycally 1.1 $M_\odot$). $R_{c,fin}$ is adjusted in order to release enough energy in neutrinos to produce explosions, and is usually set to 5-6 km. Such a low value is probably unrealistic for the 1.1 $M_\odot$ mass shell, however it is required to release enough neutrinos to compensate the high inner boundary radius of the grid. We are currently working on further improvement to the neutrino transport routine which should allow us to use a less dramatic value.

Chapter 3

Progenitor Structure and Properties

The progenitors employed for the calculations presented in this work are taken from a set of nonrotating stars of solar metallicity calculated by Woosley et al. [2002]. This set is composed by 98 progenitors, which cover the mass range 11-28 $M_\odot$ in steps of 0.2 $M_\odot$, and the mass range 28-40 $M_\odot$ in steps of 1.0 $M_\odot$. Additionally, we cover the mass range 10-11 $M_\odot$ with three stars of initial mass of 10.0, 10.2 and 10.8 $M_\odot$ (A. Heger, private communication).

A massive star spends about 90% of its life burning hydrogen and most of the rest burning helium. These relatively quiescent phases, where convection and radiation transport dominate over neutrino emission, also determine what follows during the advanced burning stages and explosion. Once the central temperature exceeds $\sim 5 \cdot 10^8$ K, neutrino losses from pair annihilation dominate the energy budget; radiative diffusion and convection remain important to the star's structure and appearance, but it is neutrino losses that, globally, balance the power generated by gravitational contraction and nuclear reactions. Indeed, the advanced burning stages of a massive star can be envisioned overall as the neutrino-mediated Kelvin-Helmholtz contraction of a carbon-oxygen core, punctuated by occasional delays when the burning of a nuclear fuel provides enough energy to balance neutrino losses. Burning can go on simultaneously in the center of the star and in multiple shells, and the structure and composition can become quite complex. Owing to the extreme temperature sensitivity of the nuclear reactions, however, each burning stage occurs at a nearly unique value of temperature and density.

Except for a range of transition masses around 8-10 $M_\odot$ (not considered in this work), each massive star ignites a successive burning stage at its center using the ashes of the previous stage as fuel for the next. Four distinct burning stages follow helium burning, characterized by their principal fuel: carbon, neon, oxygen, and silicon. Only two of these - carbon burning and oxygen burning - occur by binary fusion reactions. The other two require the partial photodisintegration of the fuel by thermal photons.
Because the late stages transpire very quickly, the surface evolution fails to keep pace and "freezes out". If the star is a red supergiant, then the Kelvin-Helmholtz time scale for its hydrogen envelope is approximately 10000 years. Once carbon burning has started, the luminosity and effective emission temperature do not change until the star explodes. Wolf-Rayet stars, the progenitors of type-Ib supernovae, continue to evolve at their surface right up to the time of core collapse.
The presupernova star is thus characterized by an iron core of roughly the Chandrasekhar mass surrounded by active burning shells and the accumulated ashes of oxygen, neon,

carbon, and helium burning. If the star has not lost its hydrogen envelope along the way, most of the radius and an appreciable part of the mass may still consist of unburned hydrogen and helium.

In addition to the complex interplay among thermal neutrino losses, degeneracy, and nuclear energy generation, the core structure is sensitive to the location and timing of numerous episodes of convective burning. Each stage of core or shell burning redistributes the entropy in such a way as to create regions where its radial derivative is small. Since the burning typically ignites at the bottom of a region of unburned fuel where the entropy is initially the least, the greatest rises in entropy occur at the bottoms of convective shells. These discontinuities serve as barriers to the outward penetration of subsequent convection zones. Since a typical star of 15 $M_\odot$ may have four stages of convective carbon burning (core burning plus three stages of shell burning) and two or three stages each of neon, oxygen, and silicon burning, the distribution of the composition becomes complicated. Indeed the location of the bases of convective shells and even the masses of iron cores in presupernova stars of variable mass may be quite nonmonotonic.

For the empirical mass-loss rates currently adopted by the groups that model the presupernova evolution, all solar metallicity stars initially more massive than about 35 $M_\odot$ are thought to end their lives as hydrogen-free objects of roughly 5 $M_\odot$ [see Woosley et al., 2002]. This not only prevents the very massive stars ($M > 100\ M_\odot$) from exploding through the pair-formation mechanism, but also limits the mass of the iron core produced at the end of their thermonuclear evolution to values below 2 $M_\odot$ and drastically increases the probability for a successful hydrodynamic supernova explosion compared with the situation without mass loss. Due to the lack of hydrogen, those supernovae would be classified as type Ib or Ic.

The density profiles of some progenitors of our sample are shown in Figure 3.1 (left panel). The end of the stellar atmosphere is recognisable by a sharp decline in density. As the mass of the star increases, the atmosphere is more and more reduced by mass loss. The right panel shows the entropy profiles. A sudden increase in the entropy profile marks the location of each composition interface.

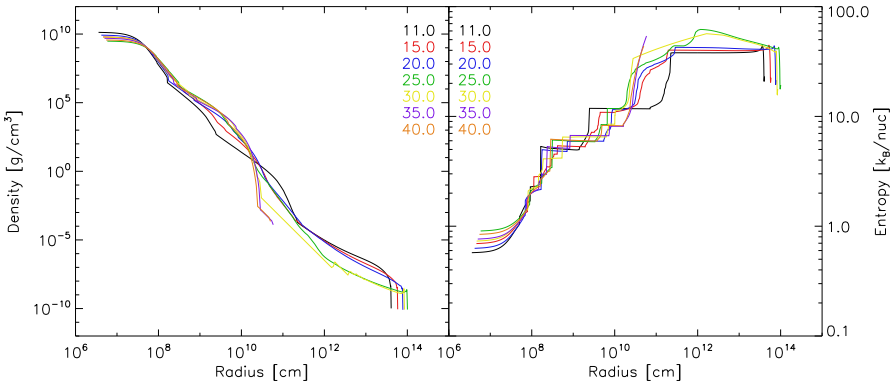

Figure 3.1: Radial profiles at time of collapse for different progenitors. *Left panel.* Density. *Right panel.* Specific entropy.

In order to carry on the calculations to sufficiently large times for the determination of the fallback (usually 10^6 s, about 12 days), the region outside the star is filled with a wind-like medium, with T=1100 K, $\rho \propto r^{-2}$ and zero velocity. In Figure 3.2 we show the resulting

density profile for a low-mass star (left panel) and for a high-mass Wolf-Rayet star (right panel). Placing the outer boundary at a radius where the density is 10^{-12} g/cm^3 is usually sufficient for our calculations.

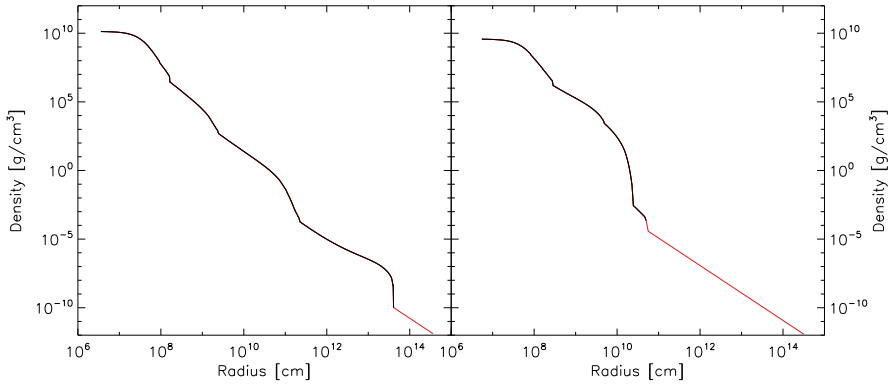

Figure 3.2: Density profiles of two progenitors. The red line marks the extension to the original model of Woosley et al. [2002]. *Left panel.* 11 $M_\odot$ model. *Right panel.* 40 $M_\odot$ model.

The presupernova structure plays a great role in determining the evolution of the supernova shock. According to the analytic blast wave solutions of Sedov [1959], the front shock decelerates whenever it travels through a region of increasing ρr^3, whereas it accelerates in regions of decreasing ρr^3. Every time the shock decelerates, it leaves behind a positive pressure gradient which slows down the post-shock layers. If the material post-shock is still in sonic contact with the shock, the deceleration occurs smoothly; otherwise, a reverse shock forms.

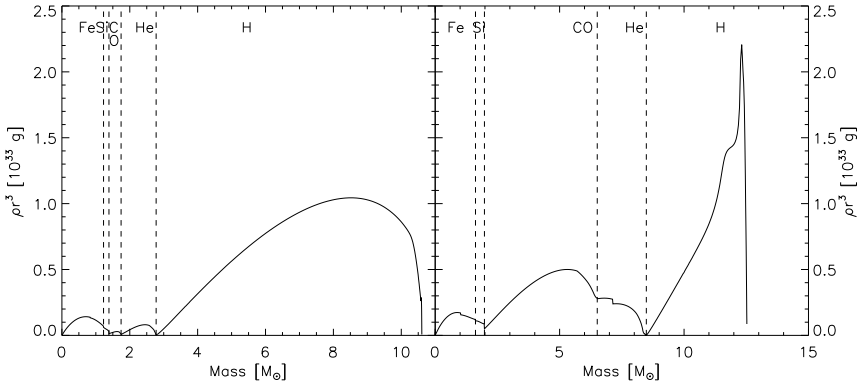

Figure 3.3: ρr^3 for different progenitors. The composition of each shell is given on top of the plot and the location of composition interfaces, where ρr^3 drops, is marked with vertical dashed bars. *Left panel.* 11 $M_\odot$ model. *Right panel.* 25 $_\odot$ model.

We plotted this quantity for different progenitors in Figures 3.3 and 3.4. For low-mass models ($M_0 \lesssim 15$ $M_\odot$), the carbon-oxygen and helium shells are not very massive and the only region where ρr^3 increases significantly is the hydrogen shell. For these stars we expect little or no fallback at early times, and more fallback when the shock enters the hydrogen shell and the reverse shock forms.
For intermediate mass models, up to about 22 $M_\odot$, the carbon-oxygen and helium shells

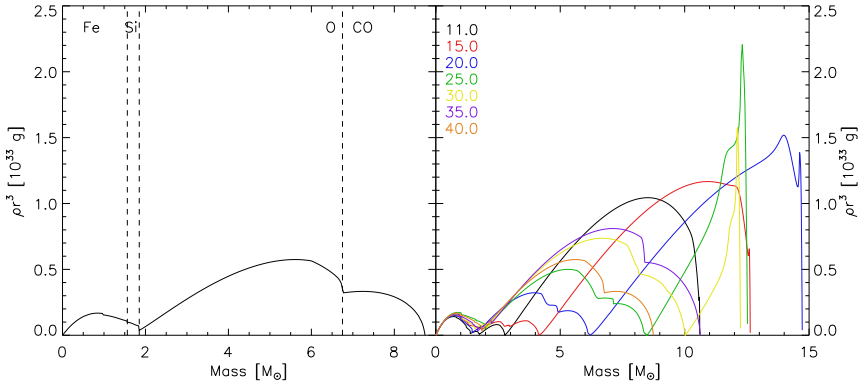

Figure 3.4: ρr^3 for different progenitors. The composition of each shell is given on top of the plot and the location of composition interfaces, where ρr^3 drops, is marked with vertical dashed bars. *Left panel.* 40 $M_\odot$ model. *Right panel.* Comparison of different models.

increase in size and become massive enough to cause some fallback; however the hydrogen shell is still the region where most fallback will occur. For more massive stars (of solar metallicity), mass loss reduces considerably the size of the hydrogen shell up to the point where the reverse shock is too weak to travel back to the compact remnant, or does not develop at all. However the carbon-oxygen shell of these stars is very massive and significant fallback can be triggered in this region.

Table 3.1 summarizes the properties of all presupernova models. The table gives the Zero Age Main Sequence (ZAMS) mass of the star, the mass M_{final} at the time of collapse, the mass of the iron core (defined as the location where the electron fraction Y_e becomes greater than or equal to 0.497), the mass coordinate where an entropy of $S/N_A k = 4$ is reached (which is typically the base of the oxygen-burning shell), the mass of the carbon-oxygen core, the mass of the helium core, the compactness parameter $\xi_{2.5}$ defined in Chapter 1, the radius of the star at the time of collapse R_{final}, measured in units of solar radius and the radius of the extended model R_{ext} that we use as outer boundary for the simulations (again measured in units of solar radius).

ZAMS [$M_\odot$]	M_{final} [$M_\odot$]	Fe Core [$M_\odot$]	$M_{S=4}$ [$M_\odot$]	CO Core [$M_\odot$]	He Core [$M_\odot$]	$\xi_{2.5}$	R_{final} [$R_\odot$]	R_{ext} [$R_\odot$]
10.0	1.580	1.287	1.317	1.580	---	0.0005	7.943	3548
10.2	10.20	1.214	1.376	1.462	2.067	0.0018	39.19	220
10.8	10.42	1.259	1.485	1.696	2.706	0.0033	562.6	5015
11.0	10.61	1.227	1.386	1.744	2.776	0.0040	586.4	5227
11.2	10.81	1.247	1.302	1.784	2.842	0.0052	594.9	5303
11.4	11.00	1.328	1.342	1.807	2.877	0.0059	596.3	5314
11.6	11.12	1.216	1.365	1.766	2.825	0.0049	581.9	5186
11.8	11.05	1.359	1.560	1.747	2.753	0.0036	569.8	5078
12.0	10.92	1.272	1.535	1.993	3.020	0.0165	636.1	5669
12.2	10.92	1.535	1.545	2.100	3.158	0.0222	674.7	6013
12.4	11.02	1.271	1.568	2.170	3.247	0.0281	679.5	5397
12.6	11.13	1.294	1.432	2.212	3.308	0.0306	685.6	5446
12.8	11.26	1.388	1.437	2.271	3.380	0.0297	695.6	5526
13.0	11.35	1.341	1.449	2.338	3.459	0.0416	709.4	5635
13.2	11.49	1.389	1.622	2.399	3.529	0.0494	741.3	5888
13.4	11.58	1.407	1.638	2.467	3.610	0.0597	754.6	5994

ZAMS [$M_\odot$]	M_{final} [$M_\odot$]	Fe Core [$M_\odot$]	$M_{S=4}$ [$M_\odot$]	CO Core [$M_\odot$]	He Core [$M_\odot$]	$\xi_{2.5}$	R_{final} [$R_\odot$]	R_{ext} [$R_\odot$]
13.6	11.71	1.422	1.648	2.529	3.679	0.0710	757.3	6015
13.8	11.84	1.423	1.591	2.591	3.745	0.0806	773.9	5479
14.0	11.96	1.435	1.668	2.648	3.816	0.0961	788.9	5585
14.2	12.08	1.495	1.678	2.708	3.889	0.1117	801.0	5671
14.4	12.23	1.502	1.693	2.770	3.956	0.1252	814.4	5765
14.6	12.37	1.544	1.697	2.834	4.028	0.1285	823.6	5830
14.8	12.48	1.540	1.753	2.901	4.101	0.1362	834.9	5910
15.0	12.63	1.553	1.721	2.960	4.167	0.1499	842.6	5964
15.2	12.71	1.407	1.809	3.037	4.250	0.1606	852.8	6037
15.4	12.88	1.422	1.836	3.101	4.317	0.1760	860.5	6091
15.6	13.00	1.351	1.444	3.172	4.392	0.1702	892.7	5632
15.8	13.10	1.350	1.461	3.239	4.467	0.1588	901.0	5684
16.0	13.24	1.360	1.475	3.312	4.541	0.1543	912.7	5758
16.2	13.41	1.362	1.479	3.376	4.612	0.1664	920.0	5804
16.4	13.53	1.380	1.492	3.445	4.687	0.1586	931.5	5877
16.6	13.71	1.388	1.501	3.515	4.766	0.1615	930.1	5868
16.8	13.83	1.400	1.507	3.586	4.844	0.1595	940.6	5289
17.0	13.83	1.402	1.511	3.658	4.926	0.1617	957.7	5385
17.2	14.07	1.416	1.527	3.729	4.998	0.1681	952.6	5357
17.4	14.20	1.407	1.533	3.808	5.074	0.1612	956.8	5380
17.6	14.34	1.420	1.554	3.879	5.147	0.1675	970.5	5457
17.8	14.45	1.410	1.866	3.956	5.225	0.2077	995.8	5599
18.0	14.49	1.389	1.476	4.031	5.311	0.2021	1010.9	5064
18.2	14.57	1.405	1.499	4.115	5.392	0.1757	1002.5	5637
18.4	14.82	1.496	1.857	4.172	5.456	0.1882	1021.1	5117
18.6	14.85	1.413	1.539	4.250	5.537	0.1730	1038.1	5202
18.8	15.04	1.405	1.525	4.323	5.609	0.1686	1042.7	5225
19.0	15.03	1.586	1.918	4.393	5.689	0.1947	1040.7	5215
19.2	15.08	1.487	1.905	4.450	5.757	0.1946	1063.8	5331
19.4	15.22	1.373	1.823	4.552	5.856	0.1890	1066.0	5342
19.6	13.36	1.465	1.603	4.888	6.239	0.1197	1163.6	5197
19.8	14.53	1.445	1.532	4.775	6.109	0.1368	1126.9	5033
20.0	14.72	1.457	1.461	4.887	6.211	0.1273	1123.1	5016
20.2	14.46	1.465	1.586	5.005	6.338	0.1055	1158.2	5173
20.4	14.80	1.507	1.680	5.041	6.372	0.1960	1148.0	5128
20.6	14.02	1.546	1.810	5.225	6.575	0.2826	1196.8	4764
20.8	14.34	1.535	1.793	5.260	6.605	0.2774	1196.0	4761
21.0	12.99	1.461	2.016	5.524	6.965	0.2173	1246.4	4962
21.2	13.55	1.483	1.915	5.515	6.908	0.1918	1243.1	4948
21.4	14.79	1.509	1.532	5.443	6.796	0.2302	1200.6	4779
21.6	13.62	1.459	1.622	5.671	7.062	0.1825	1260.6	5018
21.8	14.77	1.485	1.920	5.596	6.954	0.1910	1222.5	4866
22.0	14.41	1.440	1.546	5.717	7.078	0.1661	1256.2	5000
22.2	13.21	1.613	1.985	5.951	7.372	0.3579	1302.7	4622
22.4	14.75	1.488	1.667	5.828	7.192	0.2020	1266.8	4494
22.6	14.67	1.533	1.785	5.890	7.261	0.2578	1275.8	4526
22.8	14.34	1.627	2.001	6.039	7.405	0.3680	1300.6	4614
23.0	12.99	1.613	2.147	6.334	7.729	0.4373	1369.8	4331
23.2	15.07	1.636	2.025	6.054	7.419	0.3780	1293.4	4589
23.4	13.88	1.599	2.142	6.327	7.717	0.4296	1353.2	4801
23.6	13.72	1.658	2.120	6.424	7.813	0.4242	1371.1	4335
23.8	14.79	1.648	2.096	6.362	7.715	0.4143	1349.9	4789
24.0	14.00	1.662	2.132	6.558	7.929	0.4300	1405.6	4444
24.2	13.89	1.650	2.144	6.632	7.994	0.4364	1413.0	4468
24.4	13.17	1.610	2.109	6.788	8.165	0.4202	1415.8	4477
24.6	13.45	1.608	2.089	6.833	8.196	0.4117	1420.5	4491

ZAMS [$M_\odot$]	M_{final} [$M_\odot$]	Fe Core [$M_\odot$]	$M_{S=4}$ [$M_\odot$]	CO Core [$M_\odot$]	He Core [$M_\odot$]	$\xi_{2.5}$	R_{final} [$R_\odot$]	R_{ext} [$R_\odot$]
24.8	13.10	1.596	2.013	6.962	8.333	0.3714	1436.9	4543
25.0	12.52	1.619	1.978	7.126	8.484	0.3217	1446.9	4575
25.2	13.11	1.631	1.984	7.123	8.469	0.3589	1470.6	4650
25.4	14.14	1.609	2.046	7.015	8.371	0.3894	1458.7	4612
25.6	14.12	1.626	1.993	7.095	8.445	0.3647	1471.3	4652
25.8	12.36	1.555	1.834	7.417	12.36	0.2495	1482.2	4177
26.0	12.93	1.608	1.930	7.520	8.774	0.3386	1492.8	4207
26.2	12.23	1.537	1.718	7.657	12.23	0.2320	1477.4	4163
26.4	12.54	1.554	1.717	7.696	12.54	0.2391	1489.5	4197
26.6	13.17	1.538	1.701	7.571	8.923	0.2291	1510.3	4256
26.8	12.98	1.545	1.715	7.621	12.98	0.2341	1510.7	4257
27.0	12.44	1.506	1.679	7.209	12.44	0.2328	1482.1	4177
27.2	12.75	1.506	1.680	7.185	12.75	0.2352	1523.3	4293
27.4	13.03	1.534	1.720	7.914	13.03	0.2449	1536.4	4330
27.6	12.78	1.531	1.719	7.994	12.78	0.2474	1522.4	4290
27.8	12.56	1.515	1.704	8.166	12.56	0.2462	1497.1	4219
28.0	12.66	1.503	1.671	8.220	12.66	0.2359	1516.2	4273
29.0	12.61	1.536	1.543	7.575	12.61	0.2003	1330.7	2366
30.0	12.24	1.460	1.571	9.116	12.24	0.2240	1224.4	4874
31.0	11.71	1.447	1.584	10.28	11.71	0.1755	994.4	5591
32.0	11.99	1.479	1.671	10.26	11.99	0.1979	1112.7	4970
33.0	11.43	1.511	1.735	11.10	11.43	0.2275	3.022	2139
34.0	11.77	1.527	1.786	11.50	11.77	0.2500	0.887	3146
35.0	10.63	1.487	1.683	10.63	---	0.2057	0.840	4726
36.0	10.30	1.484	1.700	10.30	---	0.2070	1.193	4232
37.0	9.714	1.464	1.923	9.714	---	0.2855	0.789	4977
38.0	9.264	1.518	1.685	9.264	---	0.2434	0.969	3856
39.0	8.541	1.634	1.993	8.541	---	0.3625	0.754	4755
40.0	8.739	1.563	1.850	8.739	---	0.2654	0.722	4554

Table 3.1: Properties of the progenitor employed in this work.

For the neutrino-driven explosions we need to start from a model in the postbounce phase. Therefore, the original progenitors from Woosley et al. [2002] are run through collapse and bounce by Andreas Marek and Lorenz Hüdepohl with the VERTEX code [Buras et al., 2006a], up to a few ms postbounce.

Chapter 4

Comparison of Explosions Initiated by Pistons with Explosions Initiated by Neutrino Heating

4.1 Introduction

Since our understanding of the explosion mechanism of core-collapse supernovae is still incomplete and self-consistent calculations do not, as yet, yield explosions, in the study of nucleosynthesis and light curves of core collapse supernovae shock waves have to be initiated artificially.
Two methods to initiate a shock wave inside a presupernova model have been applied in the literature: "thermal bombs", used by Nomoto and collaborators (Shigeyama et al. [1988]; Hashimoto et al. [1989]; Thielemann et al. [1990]; Nakamura et al. [2001]; Nomoto et al. [2006]), and "pistons", used by Woosley and collaborators (Woosley and Weaver [1986]; Woosley and Weaver [1995]; Woosley et al. [2002]; Woosley and Heger [2007]; Zhang et al. [2008]). Aufderheide et al. [1991] have reviewed these methods, discussing the various parameters used and their effect on the nucleosynthesis results.

In the "thermal bomb" approach, the temperature of the innermost few zones of the star is greatly elevated, which in turn increases the pressure and pushes the surrounding material away. The free parameters for this model are the initial energy deposited, the volume of this deposition and the time during collapse when the bomb is started.

In the "piston" approach, the shock wave is produced by moving one mass shell in the star, the "piston", with a highly supersonic velocity. Its motion is given by a ballistic trajectory defined by

$$\frac{du}{dt} = -f\frac{GM_{pis}}{r^2}, \tag{4.1}$$

where u is the velocity of the piston, M_{pis} is the mass enclosed by the piston and f is a factor which accounts for the reduction in G due to the pressure gradient within the star. The piston is initially placed at a radius R_0 and is given an initial velocity u_0.
Usually the piston is held fixed at the maximum radius reached instead of being allowed to move back, in order to avoid artificial enhancement of the fallback. The free parameters of this approach are u_0, M_{pis}, f and the time during collapse when the piston is started.

With the piston the energy of the shock wave can only be determined *a posteriori*, contrary to the case of the thermal bomb.

Aufderheide et al. [1991] used the Nomoto and Hashimoto [1988] 20 $M_\odot$ star to compare these two methods of inducing shock waves. They studied the effect of initiating the shock at two different times during the collapse of the core (at the beginning of the collapse and at a time when all the iron core had fallen through the accretion shock) and of varying the parameter f for the piston models and they calibrated the free parameters in order to get explosion energies of about 1 foe. They concluded that the different explosion mechanism lead to uncertainties of about 30% on the nucleosinthetic yields and that the mass cut could not be constrained very precisely with such models.

They also compared the peak temperatures produced by each mechanism with an analytic expression derived assuming that the energy of the shock is dominated by radiation, and that temperature and density are uniform behind the shock. They concluded that, with either way of initiating the explosions, the peak temperatures are incorrect in the early history of the shock and this has a great impact on the explosive nucleosynthesis results, especially concerning the production of ^{56}Ni which was always overproduced in their calculations. This happened because, in the early phases of the explosion, the energy was not partitioned correctly and either too much energy was in internal energy (for the thermal bomb method), or too much energy was in kinetic energy (for the piston method).

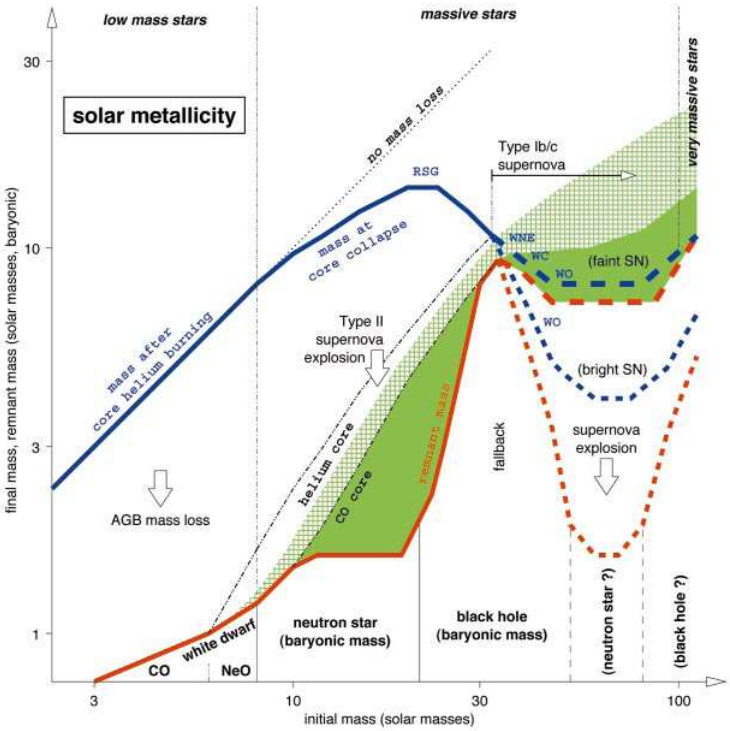

Figure 4.1: Initial-final mass function of nonrotating stars of solar composition. Credit: Woosley et al. [2002].

Nevertheless, such methods have been used to study the explosions of massive stars for decades and to derive the products of explosive nucleosynthesis and the mass function of the remnants produced.
Woosley et al. [2002] summarize the current picture of the outcome of core-collapse for

single nonrotating stars of solar metallicity in the diagram shown in Figure 4.1. They predict neutron star formation up to an initial mass of ~21 $M_\odot$, then black hole formation (via fallback), and two possible scenarios for stars of initial mass around 50 $M_\odot$, depending on the uncertain mass loss rate of Wolf-Rayet stars: if the mass loss is high enough there can be a "window" of neutron stars, otherwise only black holes are formed.

It is clear then that the currently favored methods to induce artificial explosions have several drawbacks: the mass cut and the explosion energy have to be imposed by hand, and the details of the models close to the location of the mass cut (nucleosynthesis, fallback) cannot be trusted. Furthermore ad hoc assumptions are made for the collapse phase, which will influence the stellar structure at bounce.
In order to get more reliable predictions of the remnant mass and nickel production, with the aim of better understanding the link between progenitors and supernovae, we have tried to improve the modeling of the explosion by employing a physically motivated prescription to artificially induce the explosion of the star, namely neutrino heating. In this chapter we will compare the results of piston-driven models with those of neutrino-driven models and show that many properties of the models are greatly affected by the way the explosion is triggered and that neutrino heating leads to considerable differences in the predictions.

4.2 Simulation of the explosion

4.2.1 Piston-driven explosions

We have implemented the piston method following the prescriptions of Woosley and Weaver [1995], Woosley et al. [2002] and Woosley and Heger [2007]. The piston is placed at a constant Lagrangian mass coordinate and is first moved inward for 0.45 s, then it is moved outward with a given initial velocity, u_0, that is adjusted in order to get the desired explosion energy. The piston velocity as a function of time is given by the following formula:

$$\frac{dr}{dt} = \begin{cases} v_0 - a_0 t & t < 0.45\ s, \\ \sqrt{u_0^2 + 2fGM_{pist}(1/r - 1/r_{min})} & t \geqslant 0.45\ s,\ r < 10^9\ cm, \\ 0 & t \geqslant 0.45\ s,\ r \geqslant 10^9\ cm, \end{cases} \tag{4.2}$$

where v_0 is the initial velocity of the shell where the piston is located, a_0 is a constant acceleration calculated in order to reach the minimum radius, r_{min} = 500 km, in 0.45 s (so $a_0 = 2(r_0 - r_{min} + 0.45v_0)/(0.45)^2$, with r_0 being the initial piston radius), M_{pist} is the mass enclosed by the piston and f is chosen in order to ensure that the piston coasts to an asymptotic radius ($dr/dt = 0$) of 10^9 cm (thus, $f = -u_0^2/[2GM_{pist}(10^{-9}\mathrm{cm}^{-1} - 1/r_{min})]$). The piston is then held at the maximum radius.

The free paramenters, i.e. the initial piston location (the so called "mass cut") and the explosion energy, cannot be arbitrary but are coinstrained by observations, as discussed in Woosley and Heger [2007]. In order to yield realistic values for remnant masses and nickel production, the piston mass should lie between the iron core mass (defined as the point where the electron fraction Y_e reaches 0.495) and the mass of the base of the oxygen shell (defined as the point where the dimensionless entropy S/N_Ak is equal to 4), while the explosion energy is constrained to be 1-2 B.
We have explored both choices for the piston mass (the models labeled 'PA' are the ones with the piston located at the edge of the iron core, while the models labeled 'PB' have the piston at the base of the oxygen shell), while we have set the explosion energy to be roughly 1.2 B for each model.

We employ a numerical grid of 1000 logarithmically spaced zones and we perform the calculations in two stages. In the first stage, the inner boundary of the grid coincides with the piston location. In order to retain a good resolution near the center, when the piston reaches the minimum radius $r_{min} = 5 \cdot 10^7$ cm we remap the model to a new grid, which is again composed by 1000 zones but is finer near the inner boundary (the size of the first cell is $\Delta r_1 = 0.01 * r_{ib}$ and then the cells are logarithmically spaced). Likewise, when the piston stops at the maximum radius $r_{max} = 10^9$ cm, we remap to a new grid which is built in the same way.
In order to carry on the calculation to sufficiently large times for the determination of the fallback, the original model is extended to a larger radius and the region outside the star is filled with a wind-like medium, as described in Chapter 3. The outer boundary is placed at R_{ext}, which is given for each model in Table 3.1. For the calculations presented in this Chapter we have employed a smaller progenitor set, taking the progenitors in steps of 1 $M_\odot$.

MacFadyen et al. [2001] have studied the effect of different boundary conditions on the amount of fallback in piston-driven explosions and they conclude that the inner boundary should be kept closed for the first 100 s in order to not remove pressure support from the model while the explosion is still developing. In a more realistic calculation this pressure support would be expected to be provided by the neutrino-driven wind, but in piston-driven models it is necessary to mimic this behaviour with a reflecting inner boundary. For this reason, we employ a reflecting inner boundary condition for the first 100 s, then we switch to an open boundary.
The first stage of the calculation is run to $t = 10^5$ s, then we remap to a new grid, moving the inner boundary to $r_{ib} = 10^{10}$ cm, in order to save computing time. The outer boundary is kept the same and we employ again 1000 logarithmically spaced radial zones. The second stage of the calculation is run to at least $t = 10^6$ s, or longer if needed for the fallback determination.

4.2.2 Neutrino-driven explosions

The boundary condition employed to initiate neutrino-driven explosions is described in detail in Section 2.3.1.
The free parameters of this model have been set to

- $\Gamma = 3$
- $a = 0.5$
- $R_{c,min} = 5$ km

while p has been calibrated for each model in order to get a net explosion energy (i.e. after subtracting the binding energy of the mantle of the star) of about 1.2 B for all cases.

Similarly to piston-driven explosions, we run the calculation in two stages. In the first stage we simulate the first 15 seconds of the explosion with neutrino physics. The grid is composed by 1000 logarithmically spaced zones, the inner boundary is placed at a mass coordinate of 1.1 $M_\odot$ and contracted to a minimum radius of 20 km, and the outer boundary is placed at $2 \cdot 10^{10}$ cm. The inner boundary is closed and hydrostatic equilibrium is enforced, while the outer boundary is open.
After 15 seconds, when the explosion has been launched and the neutrino luminosity from the PNS has become negligible, we switch off neutrino transport and remap to a larger grid ($r_{ib} = 10^9$ cm, $r_{ob} = R_{ext}$ given in Table 3.1). The inner boundary is left open from this moment to the end of the simulation. Once again, when the time reaches $t = 10^5$ s, we remap again to a larger inner boundary ($r_{ib} = 10^{10}$ cm) and continue the simulation

until at least $t = 10^6$ s, or longer if needed.

The initial models used for the calculations presented in this work are taken from the nonrotating solar metallicity set of Woosley et al. [2002] and are described in Chapter 3.

4.3 Hydrodynamics of some reference cases

In order to discuss the major features of piston-driven explosions, we have selected two progenitors as reference cases: a 15 $M_\odot$ progenitor, representative of low-mass stars, and a 25 $M_\odot$ model, representative of high-mass stars. We will compare the effects of different choices in the boundary location for the piston-driven models, and we will compare the results of initiating the explosions with a piston or with neutrinos.
The models representing low-mass stars are shown in section 4.3.1, while the models representing high-mass stars are shown in section 4.3.2.

4.3.1 Evolution of the 15.0 $M_\odot$ models

The model that we chose as representative of low-mass stars is a star with initial mass of 15.0 $M_\odot$. This star ends its life with a mass of 12.6 $M_\odot$, an iron core of 1.55 $M_\odot$, a silicon core of 1.72 $M_\odot$, a helium shell of 1.21 $M_\odot$ and a hydrogen shell of 8.5 $M_\odot$.

In Figures 4.2 and 4.3 we show the evolution of model P15A. For this model the piston is located at the edge of the deleptonized core, at 1.55 $M_\odot$.
Figure 4.2 displays radial profiles of density (left) and velocity (right) at different times. After the explosion is launched, a steep density profile forms close to the inner boundary and about 0.1 $M_\odot$ of matter fail to escape and remain close to the boundary with little or zero velocity. As soon as the boundary is open, at 100 s, this material feels the gravitational pull of the compact remnant in the center and develops negative velocity, quickly falling through the inner boundary on the compact remnant. Later on, when the main shock travels through the hydrogen shell, a reverse shock forms (it can be seen in the velocity profiles from 30000 s) and travels back towards the compact remnant. The reverse shock brings back another 0.12 $M_\odot$ of matter, increasing the final remnant mass to 1.80 $M_\odot$.

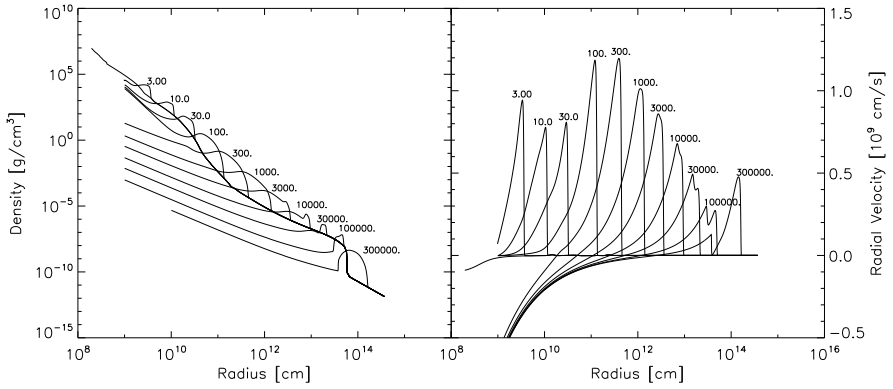

Figure 4.2: Evolution of model P15A. *Left panel.* Density as a function of radius at different times. *Right panel.* Radial velocity as a function of radius at different times.

Figure 4.3 gives the remnant mass (left) and the total mass of nickel on the grid (right) as functions of time.

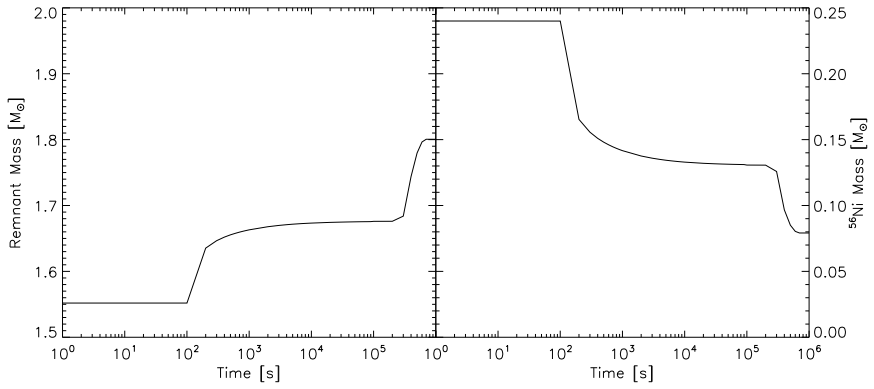

Figure 4.3: Evolution of model P15A. *Left panel.* Baryonic remnant mass as a function of time. *Right panel.* Total mass of ^{56}Ni on the grid as a function of time.

In the remnant mass plot one can see clearly that fallback happens at two distinct times. There is an "early" fallback, which consists of the material that remains close to the piston, which is accreted on the compact remnant very quickly after the opening of the boundary (100 s). Then there is "late" fallback, which consists of matter that is decelerated down to negative velocity by the reverse shock that forms when the front shock travels through the hydrogen shell. This late fallback happens usually well after 100000 s.
As is shown in the right panel of Figure 4.3, a lot of nickel forms at the beginning of the simulation. However most of this nickel remains close to the inner boundary and falls back on the compact remnant, and some more is brought back by the reverse shock: in the end only 0.08 $M_\odot$ of nickel are ejected.

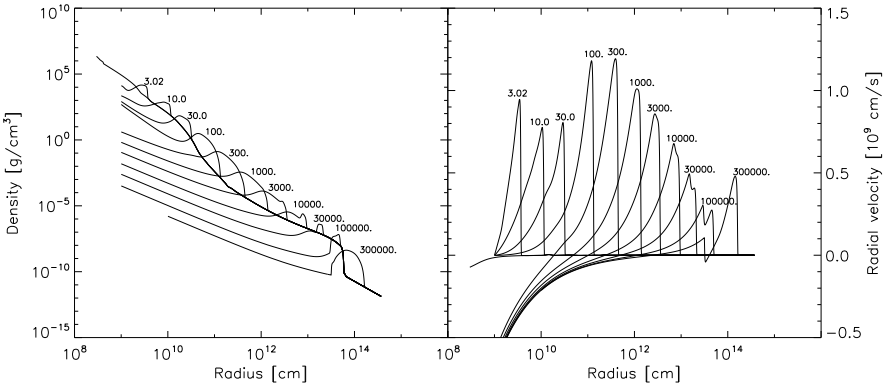

Figure 4.4: Evolution of model P15B. *Left panel.* Density as a function of radius at different times. *Right panel.* Radial velocity as a function of radius at different times.

When the piston is placed at the base of the oxygen shell, at 1.72 $M_\odot$, the material ahead of the shock is much less dense and bound, therefore the shock is more efficient in pushing matter far away from the inner boundary. The amount of "early" fallback is greatly reduced (only 0.02 $M_\odot$). The reverse shock still brings back a significant amount of matter (0.15 $M_\odot$), and the final remnant mass is 1.88 $M_\odot$ (see Figure 4.5).
Since the piston is placed further out in radius, much less nickel is produced compared to model P15A. Some of this nickel still falls back through the inner boundary (and some more is brought back by the reverse shock), so the final amount ejected is 0.05 $M_\odot$.

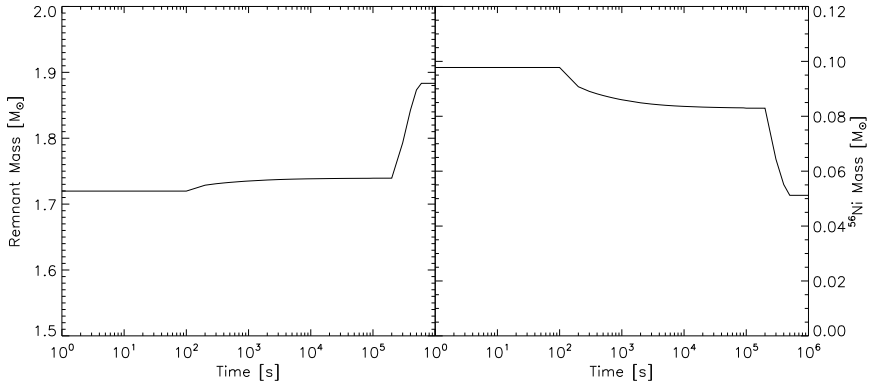

Figure 4.5: Evolution of model P15B. *Left panel.* Baryonic remnant mass as a function of time. *Right panel.* Total mass of ^{56}Ni on the grid as a function of time.

When the explosion is triggered by neutrino heating, the resulting structure is considerably different, as can be seen in Figure 4.6 where we plotted the evolution of density and velocity in model N15.

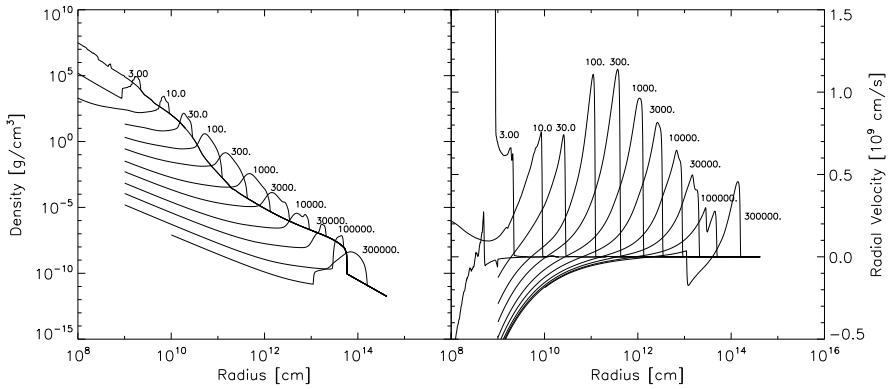

Figure 4.6: Evolution of model N15. *Left panel.* Density as a function of radius at different times. *Right panel.* Radial velocity as a function of radius at different times.

Neutrino heating pushes a dense shell of matter through the mantle of the star, while for the explosion energy considered here, $\sim 1.2 \cdot 10^{51}$ erg, little or no mass remains close to the inner boundary, where the density profile is much flatter than in the corresponding piston-driven model. For this reason the amount of mass that falls back early is minimal (even for more massive stars, as shown in Section 4.3.2) and the only way that fallback happens is via the reverse shock created when the front shock enters the hydrogen shell.

In Figure 4.8 we have plotted the accretion rate on the compact remnant (left panel) and the peak temperatures (right panel) for the three models presented above.
The early accretion rate for piston-driven models is two to three orders of magnitude greater than that of the corresponding neutrino-driven model, but this difference disappears at late times when the reverse shock arrives at the remnant.
On the other hand, initiating the explosion with a piston produces peak temperatures that are too low, at least in the early history of the shock, as already found by Aufderheide

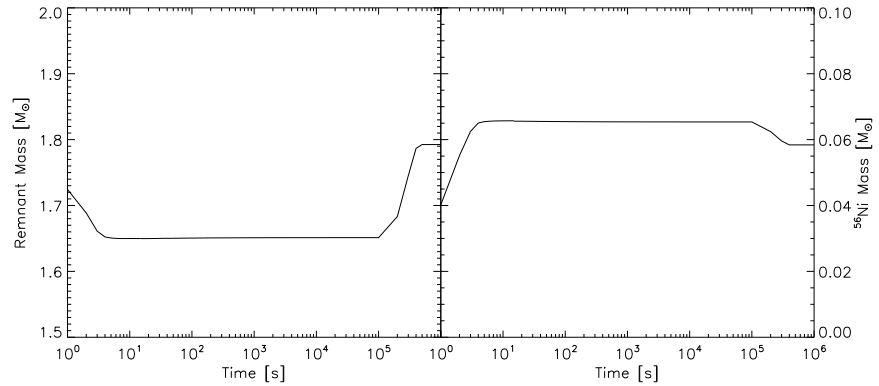

Figure 4.7: Evolution of model N15. *Left panel.* Baryonic remnant mass as a function of time. *Right panel.* Total mass of ^{56}Ni on the grid as a function of time.

et al. [1991]. This has an important effect on the nucleosinthesys, especially for nuclei produced in the vicinity of the mass cut (the most important being ^{56}Ni). Neutrino-driven models produce nickel only in a very narrow mass region, whereas piston-driven models produce much more nickel (see right panel of Fig. 4.8).

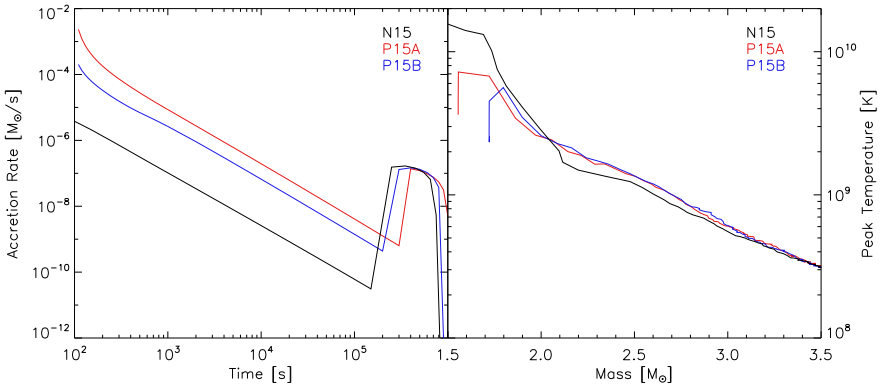

Figure 4.8: *Left panel.* Accretion rate on the compact remnant as a function of time for the 15 $M_\odot$ progenitor exploded with different methods. *Right panel.* Peak temperature as a function of time for the 15 $M_\odot$ progenitor exploded with different methods.

4.3.2 Evolution of the 25.0 $M_\odot$ models

The evolution of heavier stars is somewhat different. For such stars most of the fallback happens at early times (within the first 15-20 minutes of the explosion), because the material ahead of the shock is much more bound than in low-mass stars and the energy transported by the shock initiated with a piston is not enough to unbind it. For this reason, a significant amount of that matter remains close to the inner boundary and starts to fall back as soon as the boundary is open.
On the other hand, the hydrogen shell of these stars is less massive than that of low-mass stars because of mass loss in the presupernova evolution, so the reverse shock is significantly weaker than for lower mass stars. For stars more massive than 22-24 $M_\odot$ the reverse shock is not strong enough to travel back to the compact remnant.

Our reference model for high-mass stars has a ZAMS mass of 25.0 $M_\odot$, and loses a significant amount of its mantle during the presupernova evolution, dying with only 12.5 $M_\odot$, made up as follows: an iron core of 1.62 $M_\odot$, a silicon core of 1.98 $M_\odot$, a carbon-oxygen shell of 4.5 $M_\odot$, a helium shell of 2.0 $M_\odot$ and a hydrogen envelope of 4.0 $M_\odot$.

The evolution of the model exploded with the piston at the edge of the iron core, P25A, is shown in Figures 4.9 and 4.10. In this case the final remnant mass is 2.38 $M_\odot$. Most of the nickel produced falls back and only 0.012 $M_\odot$ are ejected.

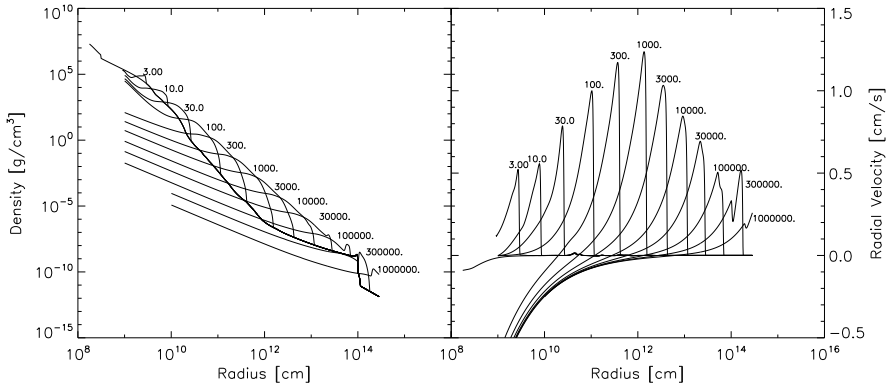

Figure 4.9: Evolution of model P25A. *Left panel.* Density as a function of radius at different times. *Right panel.* Radial velocity as a function of radius at different times.

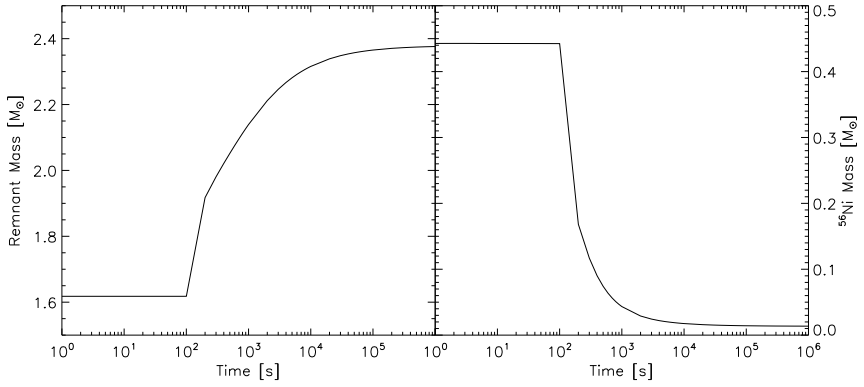

Figure 4.10: Evolution of model P25A. *Left panel.* Baryonic remnant mass as a function of time. *Right panel.* Total mass of ^{56}Ni on the grid as a function of time.

When the piston is located at the base of the oxygen shell, at 1.98 $M_\odot$ (model P25B, Figures 4.11 and 4.12), the fallback is significantly lower and the final remnant mass is 2.25 $M_\odot$. In this case a little more nickel is ejected: 0.02 $M_\odot$.

The evolution of the reverse shock can be seen in the right panel of Figs. 4.9 and 4.11. The reverse shock forms later than in the P15 models, around 100000 s, and by the time the shock exits from the grid, 1000000 s, the reverse shock is still moving out in radius and no material has acquired negative velocity. Its eventual arrival on the compact remnant

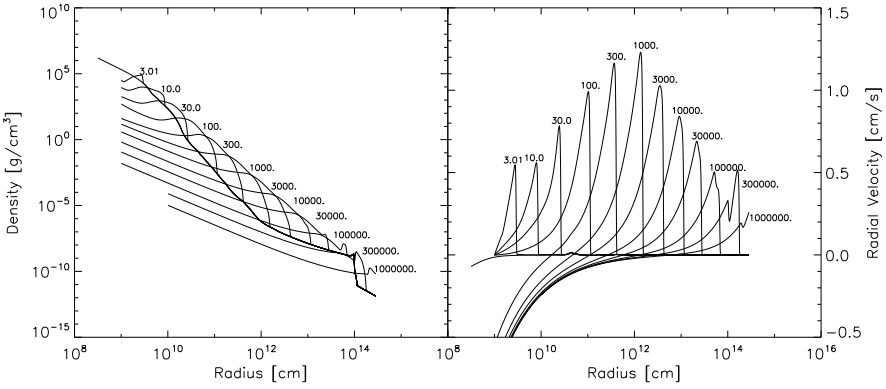

Figure 4.11: Evolution of model P25B. *Left panel.* Density as a function of radius at different times. *Right panel.* Radial velocity as a function of radius at different times.

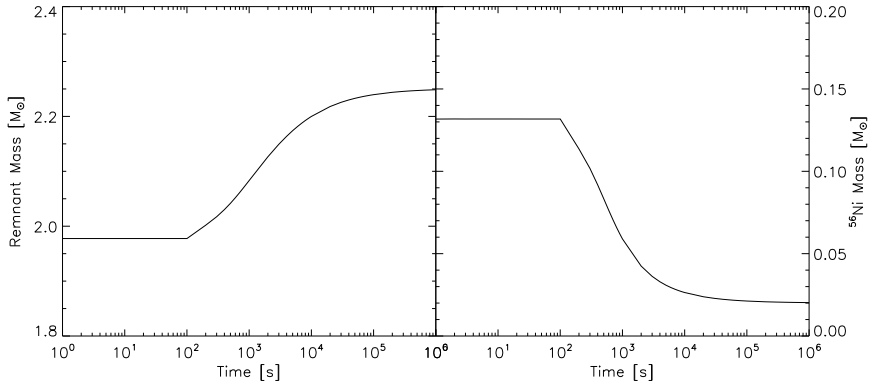

Figure 4.12: Evolution of model P25B. *Left panel.* Baryonic remnant mass as a function of time. *Right panel.* Total mass of ^{56}Ni on the grid as a function of time.

will have little or no effect on the final remnant mass.

The relation between P25A and P25B is exactly opposite to the relation between P15A and P15B, where the remnant mass was larger and Ni ejection lower for the model with the piston located further out (P15B). As we will see in Section 4.4.1, this is a general trend: in low- and intermediate-mass stars the early fallback is relatively small even for pistons located near the edge of the iron core, thus the remnant mass is bigger when the piston is located farther out; at the same time this choice leads to lower peak temperatures and thus lower nickel production. For massive stars, placing the piston at the edge of the iron core leads to considerably more massive fallback, thus to significantly bigger remnants and to (almost) no ejection of nickel.

Once again, the picture is considerably different when the star is exploded employing neutrino heating. Figure 4.13 shows the density and velocity profiles at different times. Like the case of model N15, a dense shell of matter is pushed through the mantle of the star by neutrino heating, leaving behind an almost flat density profile close to the inner boundary. There is almost no early fallback (only 0.01 M$_\odot$ of matter) and the final remnant mass is 1.87 M$_\odot$, considerably smaller than both piston models. The amount of nickel

ejected is slightly more than 0.1 $M_\odot$: almost 10 times more than in the piston models (see Figure 4.14).
In Figure 4.15 we compare the accretion rate and peak temperatures of models P25A, P25B and N25. Like in the case of the low-mass models, the piston mechanism produces much higher accretion rates and lower peak temperatures.

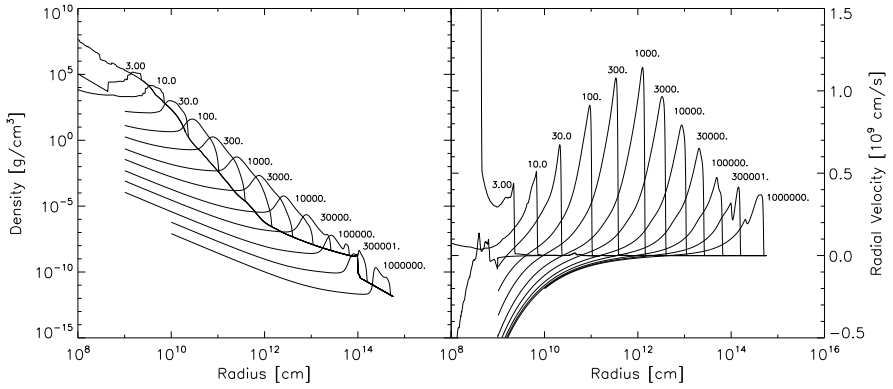

Figure 4.13: Evolution of model N25. *Left panel.* Density as a function of radius at different times. *Right panel.* Radial velocity as a function of radius at different times.

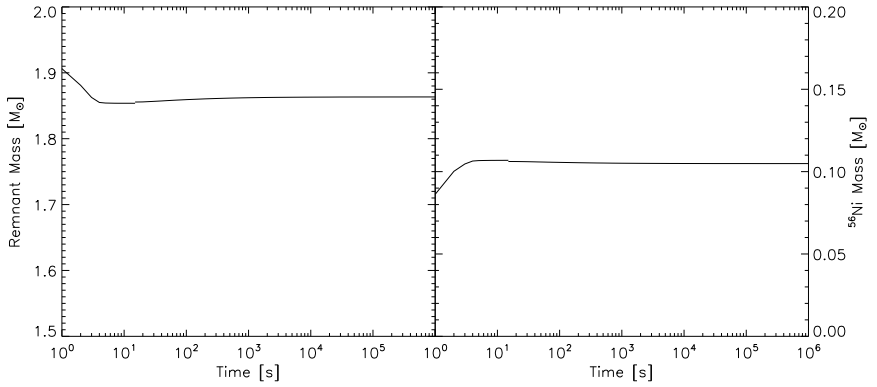

Figure 4.14: Evolution of model N25. *Left panel.* Baryonic remnant mass as a function of time. *Right panel.* Total mass of ^{56}Ni on the grid as a function of time.

In order to have significant fallback in a neutrino driven explosion, the explosion energy needs to be much lower than 1 B. This is the case of the model shown in Figures 4.16 and 4.17, a 37.0 $M_\odot$ star from the set of models computed in Chapter 5, which explodes with an energy of 0.4 B. The energy released by neutrinos is not enough to unbind all the mantle and a lot of matter falls back onto the compact remnant. However this fallback takes more time to develop than in piston-driven models (no significant fallback happens in the first 5-10 minutes of the neutrino-driven explosion) because matter was first accelerated outwards and then decelerated. Even if the final remnant, with a mass of 6.5 $M_\odot$, is clearly a black hole, 5 $M_\odot$ are ejected in a "normal" supernova event. However the luminosity from such an explosion would not show the characteristic "radioactive tail" because all the nickel that was produced in the explosion falls back.

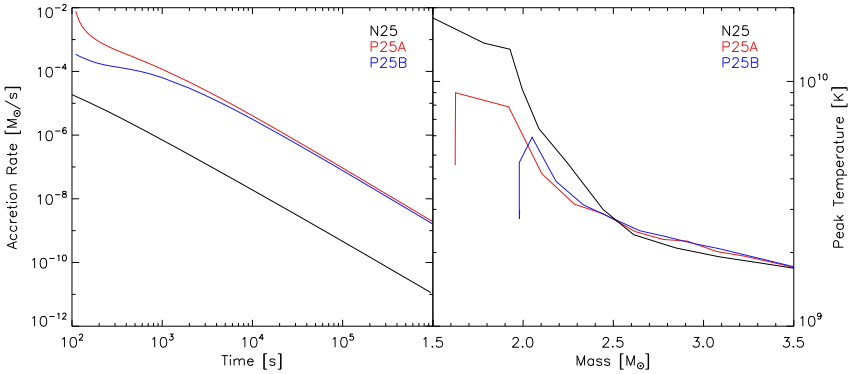

Figure 4.15: *Left panel.* Accretion rate on the compact remnant as a function of time for the 25 $M_\odot$ progenitor exploded with different mechanisms. *Right panel.* Peak temperature as a function of time for the 25 $M_\odot$ progenitor exploded with different mechanisms.

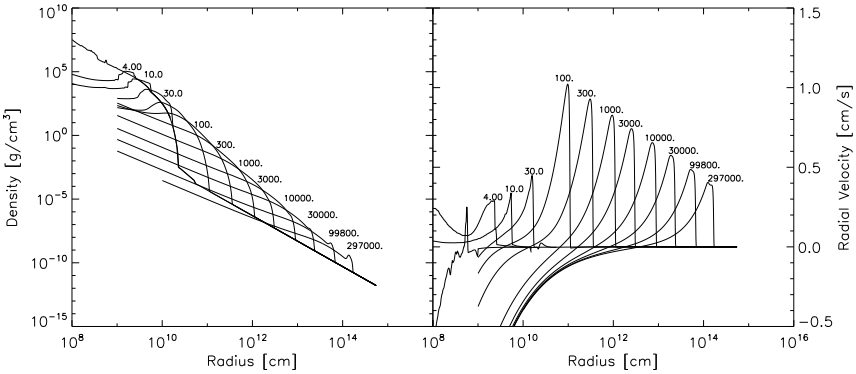

Figure 4.16: Evolution of a 37.0 $M_\odot$ star exploded by neutrino heating, with an explosion energy of 0.4 B. *Left panel.* Density as a function of radius at different times. *Right panel.* Radial velocity as a function of radius at different times.

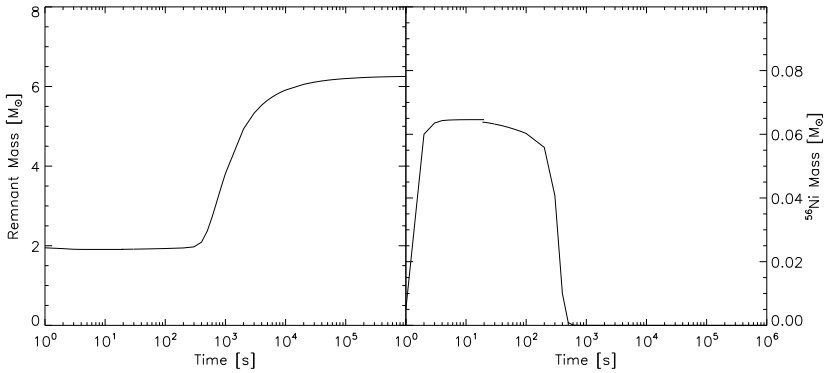

Figure 4.17: Evolution of a 37.0 $M_\odot$ star exploded by neutrino heating, with an explosion energy of 0.4 B. *Left panel.* Baryonic remnant mass as a function of time. *Right panel.* Total mass of ^{56}Ni on the grid as a function of time.

4.4 Results for solar-metallicity progenitor set

4.4.1 Remnants and fallback for piston-driven explosions

The results for the full set of models exploded by pistons are shown in Figures 4.18 and 4.19. When the piston is placed at the edge of the deleptonized core, the fallback is very massive, especially for progenitors more massive than $\sim 20\ M_\odot$.

Since there is still uncertainty about the equation of state of nuclear matter and consequently on what is the maximum neutron star mass allowed, it is difficult to say which of these remnants are black holes [see for instance Bauswein et al., 2012].
The most massive neutron star observed has a (gravitational) mass of $1.97\ M_\odot$ [Demorest et al., 2010], corresponding to a baryonic mass of about $2.2\ M_\odot$ (the exact value depends on the EoS). Therefore, the maximum neutron star mass must be at least $\sim 2.2\ M_\odot$. If this is the case, many stars of initial mass greater than $22\ M_\odot$ would form black holes via fallback, however five models, namely P27A, P28A, P29A, P31A and P38A would form neutron stars.
The upper limit for the maximum (baryonic) neutron star mass is roughly $3.0\ M_\odot$: in this case, only the model P37A would leave behind a black hole, while all the others would form neutron stars.
Nevertheless, fallback brings back a lot of nickel for the massive stars. While the supernovae will eject most of the progenitor mass, their luminosity will drop quickly with time since there is almost no contribution from ^{56}Ni decay. The piston models are compatible with speculations that *faint SNe* are associated with fallback and massive progenitors.

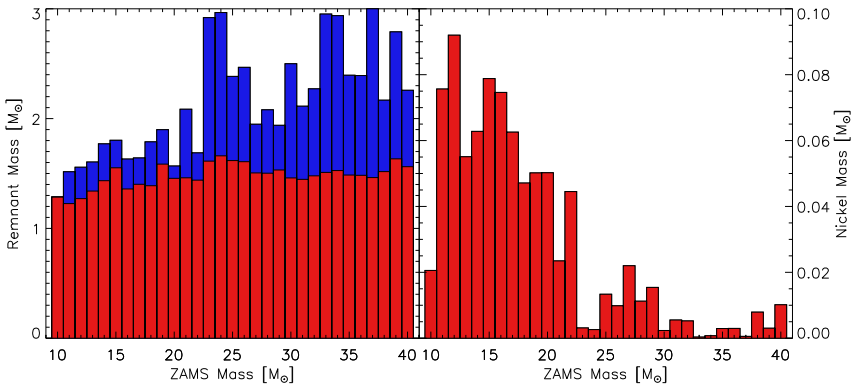

Figure 4.18: Results for piston located at the edge of the iron core (set PA). *Left panel.* Baryonic remnant mass as function of ZAMS mass. *Right panel.* Nickel ejection as function of ZAMS mass.

The scenario is somewhat different for the set of models PB, exploded with a piston located at the base of the oxygen burning shell. In this case the fallback is considerably smaller than in set PA, but the initial remnant mass is greater. For progenitors with ZAMS mass lower than about $20\ M_\odot$ then the final remnant mass is usually greater than that of set PA, while the opposite happens for more massive progenitors. Similar considerations hold for the nickel ejection: the amount of nickel ejected is (generally) lower for low-mass progenitors, due to the lower peak temperatures of models PB, and higher for more massive progenitors, due to less fallback.
Once again the exact fraction of remnants which are black holes depends on the uncertain maximum mass for neutron stars: for $M_{NS}^{max} = 2.2\ M_\odot$ we would have 13 black holes, for $M_{NS}^{max} = 3.0\ M_\odot$ none of the models computed would for a black hole and for intermediate

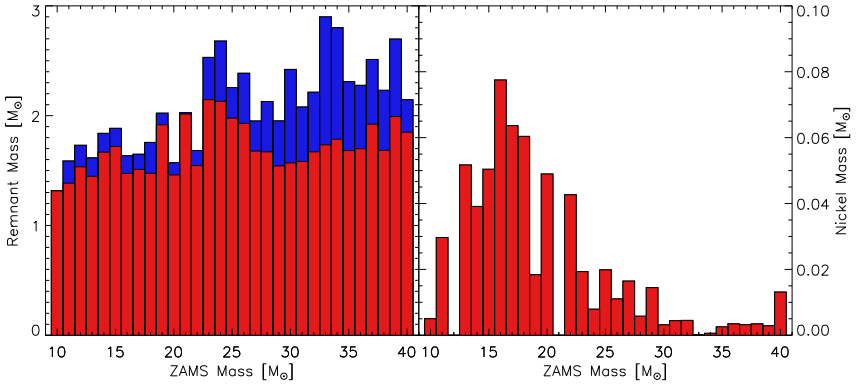

Figure 4.19: Results for piston located at the base of the oxygen shell (set PB). *Left panel.* Baryonic remnant mass as function of ZAMS mass. *Right panel.* Nickel ejection as function of ZAMS mass.

values we expect that the number of black holes formed is slightly lower than for set PA.

It is somewhat difficult to compare our piston models to those of Woosley and collaborators, since they have not published detailed results from the progenitor sequence that we have employed.
We have tried to compare our results to those of Zhang et al. [2008] and MacFadyen et al. [2001], who employ solar metallicity stars whose properties are not very different from our sample and an Eulerian code (although the explosion is always calculated with the Lagrangian code KEPLER and only linked to the Eulerian code at later times). We find that our piston models tend to develop more fallback than the models published in these works, for similar explosion energies. We believe that the difference originates from different density profiles close to the inner boundary: KEPLER produces much flatter density profiles (see Fig. 1 in Zhang et al. [2008] and Fig. 4 in MacFadyen et al. [2001]), possibly because of insufficient resolution near the origin at times when most mass is far away from the inner boundary (A. Heger, private communication).

The results for the piston models, together with the values of the parameters adopted for each model, are listed in Table 4.1.

	Model sequence PA					Model sequence PB				
ZAMS $M_\odot$	u_0 10^9 cm/s	E_{exp} B	M_{pis} $M_\odot$	M_{end} $M_\odot$	M_{Ni} $M_\odot$	u_0 10^9 cm/s	E_{exp} B	M_{pis} $M_\odot$	M_{end} $M_\odot$	M_{Ni} $M_\odot$
10.0	4.750	1.160	1.287	1.288	0.021	7.188	1.160	1.317	1.317	0.005
11.0	2.172	1.213	1.226	1.516	0.076	4.541	1.224	1.385	1.587	0.030
12.0	2.328	1.152	1.271	1.557	0.092	6.688	1.153	1.534	1.730	0.000
13.0	2.313	1.195	1.340	1.604	0.055	3.500	1.190	1.448	1.616	0.052
14.0	1.922	1.238	1.435	1.770	0.063	3.688	1.241	1.668	1.839	0.039
15.0	2.203	1.239	1.552	1.802	0.079	3.531	1.243	1.720	1.885	0.050
16.0	2.203	1.233	1.359	1.631	0.075	2.969	1.228	1.474	1.635	0.077
17.0	2.281	1.183	1.402	1.641	0.063	3.250	1.192	1.510	1.649	0.064
18.0	2.016	1.196	1.389	1.788	0.047	2.313	1.195	1.475	1.756	0.060
19.0	2.063	1.190	1.585	1.899	0.050	5.688	1.204	1.917	2.023	0.018
20.0	3.469	1.185	1.456	1.568	0.050	3.500	1.176	1.461	1.571	0.049
21.0	1.750	1.270	1.461	2.082	0.024	6.188	1.251	2.015	2.027	0.000
22.0	2.406	1.193	1.440	1.686	0.045	3.438	1.195	1.545	1.681	0.043
23.0	1.375	1.274	1.613	2.912	0.003	2.906	1.257	2.146	2.526	0.020
24.0	1.422	1.251	1.661	2.956	0.003	2.906	1.239	2.131	2.672	0.008
25.0	1.719	1.300	1.618	2.380	0.014	3.688	1.290	1.978	2.252	0.020
26.0	1.750	1.334	1.607	2.471	0.010	3.398	1.340	1.930	2.390	0.011

ZAMS $M_\odot$	u_0 10^9 cm/s	E_{exp} B	M_{pis} $M_\odot$	M_{end} $M_\odot$	M_{Ni} $M_\odot$	u_0 10^9 cm/s	E_{exp} B	M_{pis} $M_\odot$	M_{end} $M_\odot$	M_{Ni} $M_\odot$
27.0	2.250	1.278	1.505	1.951	0.022	3.984	1.269	1.678	1.954	0.016
28.0	2.281	1.265	1.503	2.084	0.011	3.906	1.251	1.671	2.123	0.006
29.0	3.344	1.315	1.532	1.942	0.015	3.375	1.301	1.543	1.948	0.015
30.0	2.234	1.269	1.460	2.504	0.002	2.625	1.266	1.570	2.426	0.003
31.0	2.469	1.244	1.447	2.117	0.005	3.906	1.243	1.583	2.083	0.004
32.0	2.203	1.285	1.479	2.276	0.005	3.719	1.271	1.671	2.218	0.004
33.0	1.969	1.134	1.510	2.962	0.000	3.531	1.125	1.734	2.909	0.000
34.0	1.984	1.274	1.527	2.947	0.001	3.688	1.281	1.785	2.810	0.001
35.0	2.172	1.265	1.486	2.400	0.003	3.781	1.262	1.682	2.364	0.002
36.0	2.094	1.235	1.484	2.397	0.003	3.688	1.241	1.699	2.281	0.003
37.0	1.844	1.218	1.463	3.010	0.001	3.750	1.180	1.922	2.518	0.003
38.0	2.250	1.239	1.517	2.172	0.008	3.813	1.230	1.684	2.236	0.003
39.0	1.641	1.282	1.633	2.796	0.003	3.219	1.265	1.991	2.703	0.003
40.0	1.844	1.252	1.562	2.261	0.010	4.000	1.254	1.850	2.148	0.013

Table 4.1: Explosion energy, remnant mass, nickel ejected and choice of parameters for all models exploded with pistons.

4.4.2 Remnants and fallback for neutrino-driven explosions

Figure 4.20 shows the results for our sequence N, exploded with enhanced neutrino heating from the inner boundary. Since neutrino heating is much more efficient in unbinding the matter outside of the core, because of the push of the neutrino-driven wind phase, there is almost no "early" fallback and the remnants are much smaller than those of the sets PA and PB (for the same explosion energy). The amount of nickel ejected is also greater and all models would be seen as "canonical" supernovae, with the usual tail in the luminosity created by nickel decay. None of the models exploded with neutrinos with an explosion energy of $1.2 \cdot 10^{51}$ erg forms a black hole.

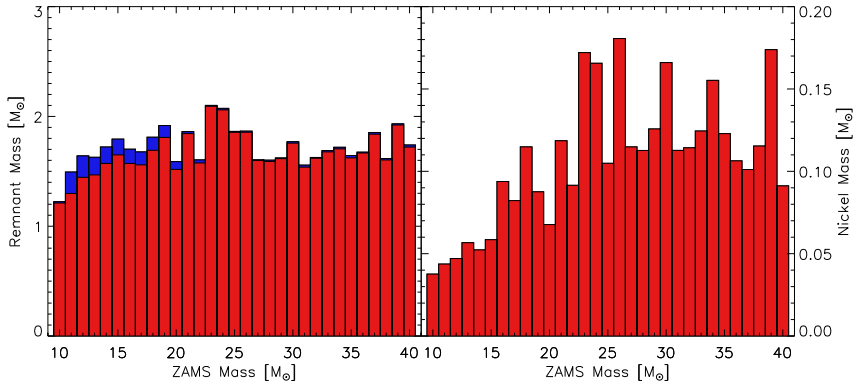

Figure 4.20: Results for neutrino-driven explosions. *Left panel.* Baryonic remnant mass as function of ZAMS mass. *Right panel.* Nickel ejection as function of ZAMS mass.

Figure 4.21 shows the total energy emitted in neutrinos at the inner boundary (left panel) and at 500 km (right panel) for each model. This quantity can be regarded as an indication of how "difficult" it is to explode a given star with our boundary condition, or rather of how likely it is for a given star to explode with $\sim 1.2 \cdot 10^{51}$ erg. For some models (N18, N19, N21, N23, N24, N25, N26, N30, N37, N39) the neutrino energy input required to explode the star with the given energy is much greater than for the neighbour models: it is possible that at least some of these stars would not explode, or would explode less

energetically, in a realistic scenario.

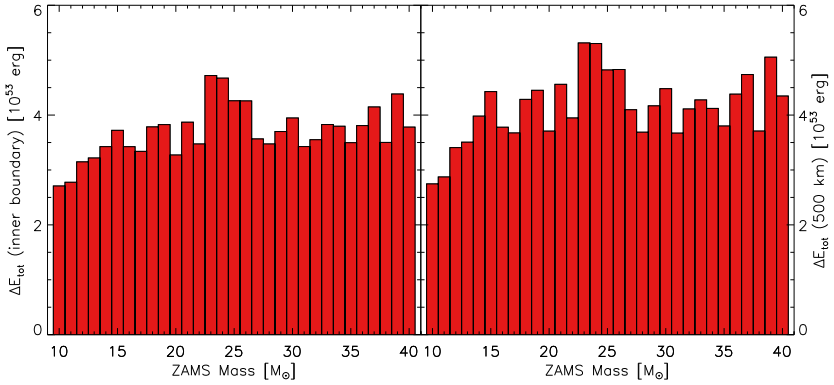

Figure 4.21: Total energy release as function of ZAMS mass. *Left panel.* Measured at the inner boundary. *Right panel.* Measured at 500 km.

The results of the neutrino-driven models, together with the parameters adopted for the explosions, are summarized in table 4.2.

	Model sequence N				
ZAMS $M_\odot$	p	E_{exp} B	$M_{15\ s}$ $M_\odot$	M_{end} $M_\odot$	M_{Ni} $M_\odot$
10.0	-2.44	1.168	1.212	1.223	0.038
11.0	-2.50	1.216	1.298	1.494	0.044
12.0	-2.84	1.152	1.445	1.641	0.047
13.0	-2.75	1.189	1.468	1.628	0.057
14.0	-2.55	1.240	1.572	1.721	0.052
15.0	-2.63	1.239	1.650	1.793	0.058
16.0	-3.01	1.232	1.572	1.701	0.093
17.0	-2.93	1.194	1.559	1.677	0.082
18.0	-3.43	1.192	1.692	1.801	0.115
19.0	-3.48	1.195	1.809	1.917	0.086
20.0	-2.79	1.178	1.517	1.589	0.068
21.0	-3.65	1.259	1.844	1.862	0.119
22.0	-2.92	1.187	1.576	1.604	0.091
23.0	-3.44	1.269	2.093	2.100	0.172
24.0	-3.31	1.243	2.060	2.073	0.166
25.0	-3.15	1.282	1.856	1.863	0.105
26.0	-3.21	1.337	1.856	1.866	0.181
27.0	-2.75	1.277	1.599	1.605	0.115
28.0	-2.92	1.257	1.590	1.601	0.113
29.0	-3.24	1.305	1.616	1.622	0.126
30.0	-3.66	1.266	1.757	1.770	0.166
31.0	-2.92	1.235	1.538	1.556	0.113
32.0	-2.90	1.280	1.619	1.626	0.114
33.0	-2.87	1.131	1.677	1.689	0.124
34.0	-3.07	1.278	1.705	1.719	0.155
35.0	-2.88	1.262	1.622	1.644	0.123
36.0	-2.88	1.237	1.667	1.675	0.106
37.0	-3.61	1.196	1.838	1.853	0.101
38.0	-2.89	1.227	1.604	1.616	0.115
39.0	-3.22	1.276	1.922	1.932	0.174
40.0	-2.85	1.253	1.721	1.740	0.091

Table 4.2: Explosion energy, remnant mass, nickel ejected and choice of parameters for all models exploded with neutrino heating.

4.5 Conclusions

We have presented calculations of supernova explosions for massive stars of solar metallicity, initiated with two different methods: enhanced neutrino heating and pistons. We have adjusted the parameters in order to have "canonical" explosion energies of roughly 1.2 B and we have compared for each model the effect of different methods of initiating the explosion. We have found that when neutrino heating is taken into account, the structure of the exploding shells, especially the regions closer to the core, is considerably different from the models exploded with pistons. This in turn leads to different results for the remnant masses and the nickel production. In particular we have found that neutrino heating is much more efficient in unbinding the material of the star envelope and that in this case the amount of matter that fails to escape and falls back on the compact remnant is greatly reduced, especially in stars more massive than about ~20 $M_{\odot}$. This also means that more heavy elements are ejected in the case of neutrino-driven explosions. We conclude than that in order to make reliable predictions of the final remnant mass and of the nucleosynthesis yields of a supernova explosions one should not neglect the effect of neutrinos.

Chapter 5

Explosion and Remnant Systematic for Neutrino-driven Explosions

5.1 Simulation Setup

The analytic model for the cooling of the proto-neutron star employed to initiate neutrino-driven explosions is described in detail in Section 2.3.1.
The free parameters of this model have been calibrated in order to reproduce the observed properties (explosion energy, remnant mass and nickel ejected) of SN1987A, with a suitable progenitor of our set. We have computed explosions for different progenitors in the mass range 18-20 $M_\odot$ and found that the observables were best reproduced by the progenitor of initial mass 19.8 $M_\odot$, exploded with this choice of parameters:

- Γ = 3,
- a = 0.6,
- $R_{c,min}$ = 6 km,
- p = -3.00.

The evolution of the calibration model is shown in Section 5.2.
This choice of parameters was then employed for all the models computed.

Similarly to the models presented in Chapter 4, we run the calculations in two stages. In the first stage we simulate the first 8-20 seconds of the explosion with neutrino transport. The grid is composed by 1000 logarithmically spaced zones, the inner boundary is placed at a mass coordinate of 1.1 $M_\odot$ and contracted to a minimum radius of 20 km, and the outer boundary is placed at $1.5 \cdot 10^{10}$ cm. The inner boundary is closed and hydrostatic equilibrium is enforced, while the outer boundary is open.
We switch off neutrino transport and remap to a larger grid when the shock has reached a radius of 10^{10} km, which happens at a different time for each model, usually between 8 and 20 s. The neutrino luminosity is very low at this time, therefore the difference in the models introduced by the different time at which we switch off neutrinos is negligible.
The new grid has an inner radius $r_{ib} = 10^9$ cm and an outer radius $r_{ob} = R_{ext}$ given in Table 3.1. The inner boundary is left open from this moment to the end of the simulation. Once again, when the time reaches $t = 10^5$ s, we remap again to a larger inner boundary ($r_{ib} = 10^{10}$ cm) and continue the simulation until at least $t = 10^6$ s, or longer if needed.

The initial models used for the calculations presented in this work are taken from the nonrotating solar metallicity set of Woosley et al. [2002] and are described in Chapter 3.

5.2 Evolution of the calibration model

In Figure 5.1 we show a mass-shell plot for the space-time evolution of the calibration model in the first stage of the computation.

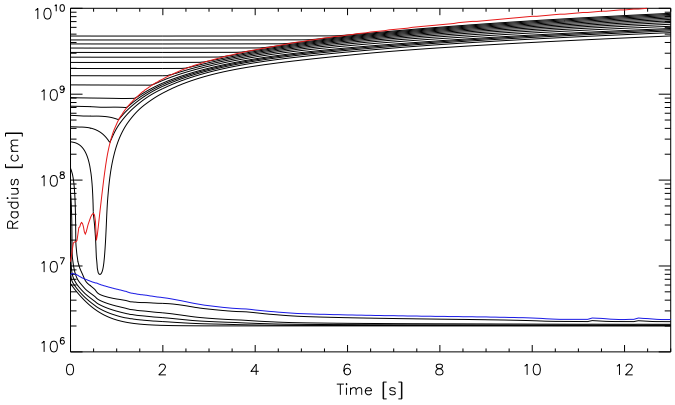

Figure 5.1: Mass shell plot for the evolution of the calibration model. The explosion occurs about 0.6 s after bounce. The red line marks the supernova shock, the blue line marks the neutron star radius and the black line marks the grid inner boundary. Mass shells are plotted every 0.1 $M_\odot$ between 1.1 and 2.0 $M_\odot$, then every 0.2 $M_\odot$ between 2.0 and 4.0 $M_\odot$.

The explosion sets in about 0.6 s after bounce. At this time the stalled shock is revived by neutrino heating and starts continuous expansion with an average velocity of roughly 8000 km/s. On its way out the shock reverts the infall of the swept-up matter. When the shock reaches the radius of 100000 km (at about 12.5 s), we switch to the second stage of the simulation.
Figure 5.2 displays the ν_e (solid line) and $\bar{\nu}_e$ (dashed line) luminosities (left panel) and mean energies (middle panel) emitted by the nascent neutron star, and the total energy released in neutrinos (right panel), all quantities measured at a radius of 500 km.

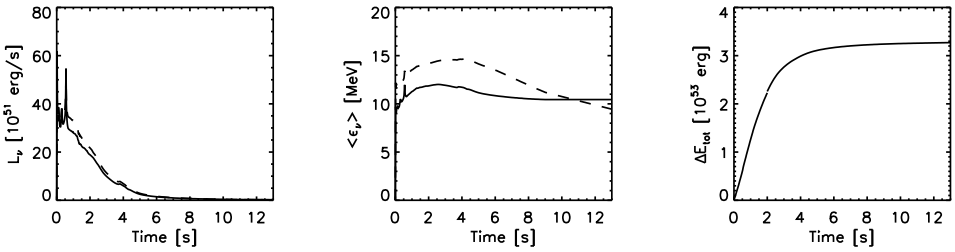

Figure 5.2: Luminosities *(left)* and mean energies *(middle)* of ν_e *(solid line)* and $\bar{\nu}_e$ *(dashed line)*, and total energy radiated in neutrinos of all flavors *(right)*, for the calibration model as a function of time, measured outside of the nascent neutron star (at a radius of 500 km).

The peaks that can be seen in the luminosity are characteristic of the accretion phase, during which the shock develops the so-called "oscillatory radial instability" [Fernández,

2012] and neutrinos are emitted in bursts every time that the shock retreats. After the explosion sets in at about 0.6 s, the luminosity decreases quickly. The same behaviour can be seen in the mean energy plot (middle panel). The neutrino mean energies increase during the first one-two seconds of postbounce evolution because the inner grid boundary and the neutron star radius contract. Consequently, the outer layers of the neutron star heat up due to the conversion of gravitational energy to internal energy by compression. After two-three seconds the contraction is almost over and the decay of the boundary luminosities leads to less energy being transported into these layers, which therefore begin to cool down, causing the mean energies of the radiated neutrinos to decline.
Figure 5.3 displays the time evolution of the three quantities that we compare to SN1987A observables: remnant mass (left panel), nickel mass (middle panel) and explosion energy (right panel).

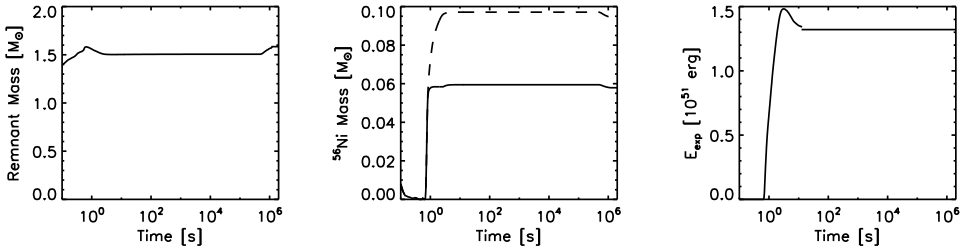

Figure 5.3: Baryonic remnant mass *(left)*, minimum *(solid line)* and maximum *(dashed line)* of the uncertainty range for the nickel mass *(middle)* and explosion energy *(right)*, for the calibration model as functions of time. The final values of these quantities reproduce reasonably well the values extrapolated by observational data of SN1987A.

The final remnant mass is 1.584 $M_\odot$, the amount of nickel ejected is about 0.076 $M_\odot$ and the explosion energy is 1.321 B. These numbers agree reasonably well with the values extrapolated by observational data of SN1987A [Arnett et al., 1989], therefore we adopted this model for the calibration of our set of explosions.

5.3 Results for the full set of progenitors

Figure 5.4 shows the explosion energy as a function of the ZAMS mass. Significant variability between stars of similar ZAMS mass is visible: some of the models do not explode, whereas others explode with fairly high explosion energy. We find failed explosions even for some stars of relatively low mass (down to 15.2 $M_\odot$) and we can identify two mass windows in the ZAMS domain where the stars of the employed set of progenitor models appear to be particularly hard to explode: one between 15 and 16 $M_\odot$ and the other around 23-26 $M_\odot$. Not surprisingly, these models also have quite big iron and silicon cores (see Figs. 5.20 and 5.22).
We note that almost all the low-mass models (mass below 15 $M_\odot$), with only three exceptions, explode with an energy between 1.5 and 2 B, which is very high, contrary to what detailed calculations find for this mas range [see e.g. Marek and Janka, 2009]. We believe that this is the consequence of having to employ a high boundary luminosity in order to explode the more massive calibration model with an energy of 1.3 B, and that further improvements of the modeling (e.g. taking into account multidimensional effects) will allow to reduce the boundary luminosity and get more reasonable explosion energies for low-mass star. Nevertheless, the high explosion energy does not prevent these models to have significant fallback (between 0.2 and 0.3 $M_\odot$, see Fig. 5.6) and does not affect by more than a few percent the amount of nickel ejected.

We also note that there is not an upper stellar mass limit for explosions with the explored range of solar-metallicity stars, where we get an explosion even for the 40 $M_\odot$ progenitor.

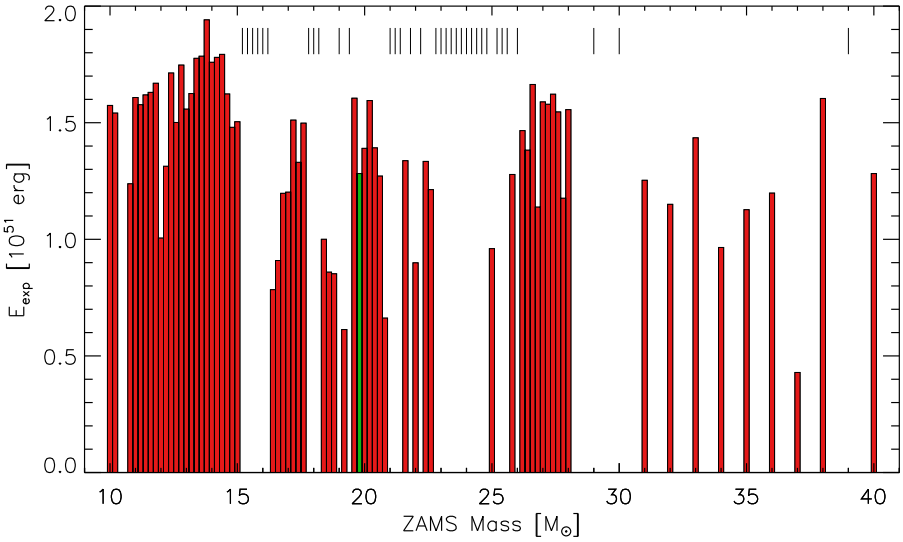

Figure 5.4: Explosion energy as a function of ZAMS mass. Non-exploding computed models are indicated by short vertical bars near the top of the plot. The calibration model is indicated with a green bar.

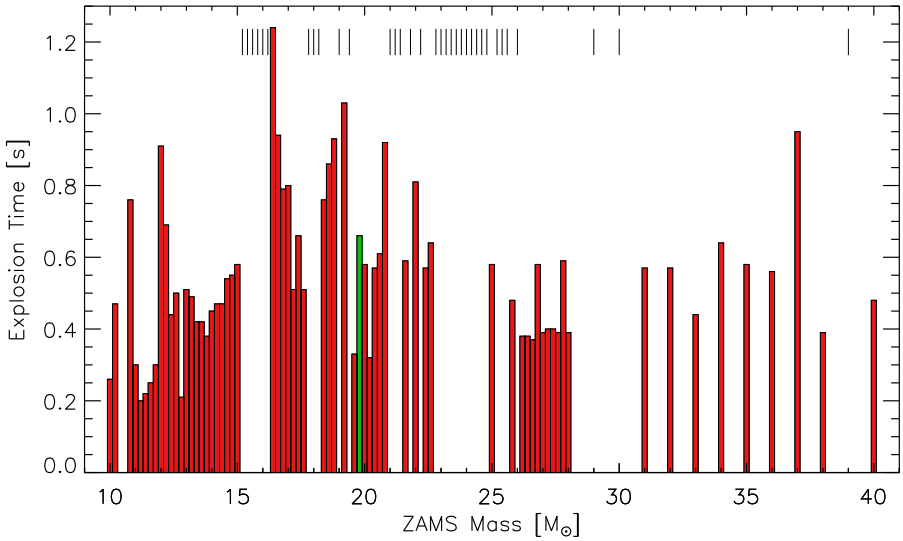

Figure 5.5: Explosion times as a function of ZAMS mass. Non-exploding computed models are indicated by short vertical bars near the top of the plot. The calibration model is indicated with a green bar.

Figure 5.5 displays the time at which the explosion sets in, which is defined as the time when the shock radius reaches 500 km, since all recent simulations find that if the shock expands up to roughly 500 km it will not retreat anymore and the explosion will be

launched [see e.g. Marek and Janka, 2009].
Fryer et al. [2012], by analizing the time evolution of the energy stored in the convective region, predict that explosions will be less energetic the longer they are delayed. While we do find that, in general, the explosions that happen later are less energetic, this is not true for all cases. For instance, models N11.0 and N11.2 have almost the same explosion energy, but there is a difference of more than 0.1 s between the explosion times; the same happens for models N18.4 and N18.6; model N16.6 has one of the more delayed explosions, with 0.9 s between bounce and explosions, and still has an explosion energy of 0.9 B which we would not define low (and is definitely higher than the 0.5 B of model N20.8, or the 0.4 B of model N37.0, both exploding with a similar delay); models N20.4 and N20.6 explode more or less at the same time, but there is a difference of 0.2 B in the explosion energy and the same is true for models N26.4 and N26.6, where the explosion energy difference is about 0.3 B.

In Figure 5.6 we have plotted the final remnant mass distribution as a function of the ZAMS mass. The initial remnant mass, measured at the time of the remap between the two stages of the simulation, is indicated by red bars, while the blue bars indicate the amount of fallback.
The distribution is broad and the remnant mass is not a monotonic function of the initial mass. It is interesting to note, as already discussed in Chapter 4, that we find significant fallback (between 0.2 and 0.3 $M_\odot$) for low- and intermediate-mass stars, and almost no fallback (less than 0.1 $M_\odot$) for more massive stars, with the only exception of model N37.0, which explodes with a very low explosion energy ($\sim$ 0.4 B) and forms a black hole with a mass of 6.5 $M_\odot$ via fallback. This model has been analyzed in detail in Section 4.3.2.

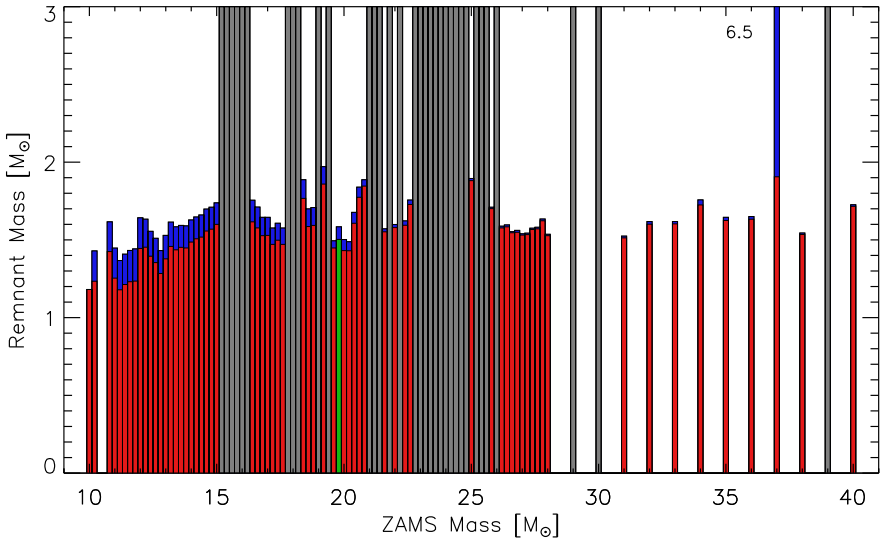

Figure 5.6: Remnant mass as a function of ZAMS mass. The blue bars on top of the red ones indicate the fallback mass. All remnants with mass greater than 3 $M_\odot$ are black holes produced via direct collapse of a non-exploding star. The only model which forms a black hole via fallback is N37.0. Red bars indicate models that explode, grey bars indicate models that do not explode. The calibration model is marked by a green bar.

Figure 5.7 displays the total energy emitted in neutrinos, as a function of the ZAMS mass. This distribution follows closely that of the remnant mass.
Finally, Figure 5.8 shows the mass of nickel that is ejected in the explosion. Since our

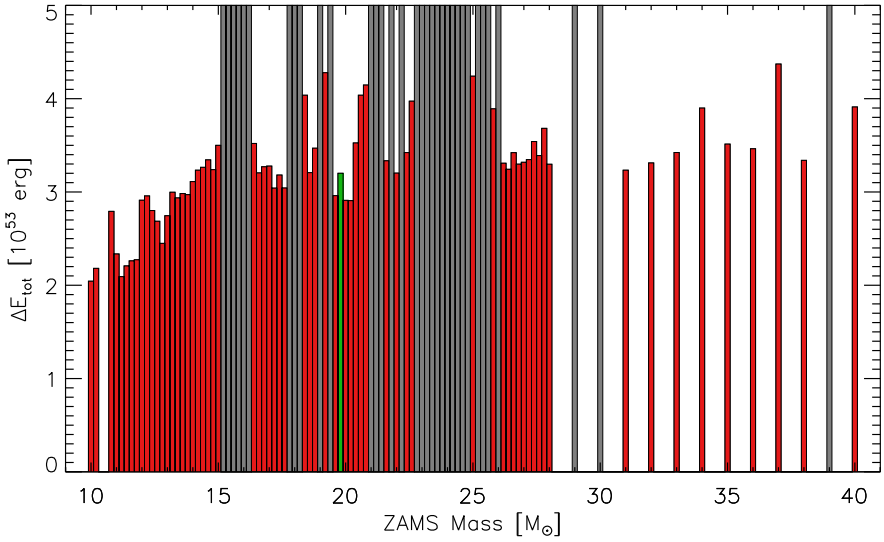

Figure 5.7: Total energy emitted in neutrinos as a function of ZAMS mass. Red bars indicate models that explode, grey bars indicate models that do not explode. The calibration model is marked by a green bar.

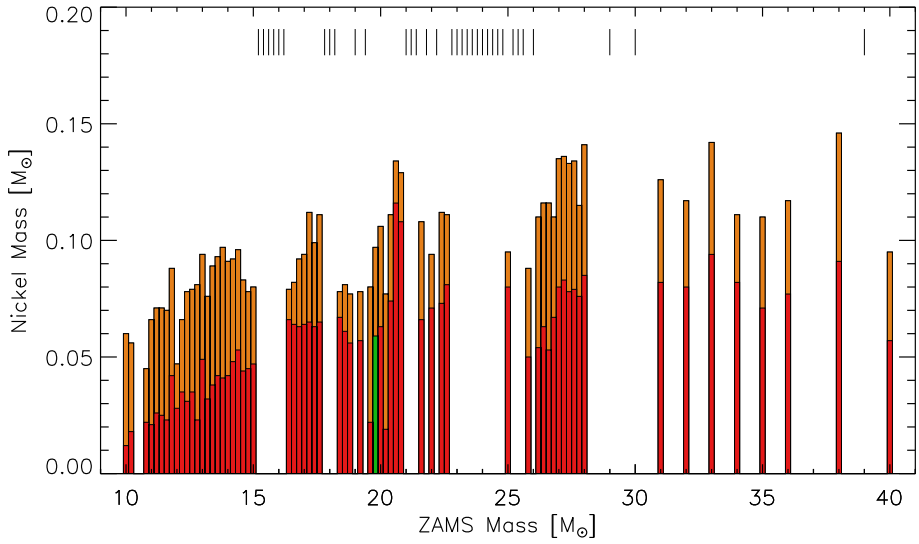

Figure 5.8: Mass of ^{56}Ni ejected in the explosion as a function of ZAMS mass. The red and orange bars indicate minima and maxima of the uncertainty range. Non-exploding computed models are indicated by short vertical bars near the top of the plot. The calibration model is indicated with a green bar.

simplified neutrino transport treatment does not allow to calculate the electron fraction Y_e very precisely, the red and orange bars indicate minima and maxima of the uncertainty range, respectively. We again find some variability, up to factors of 2-3, between progenitors of similar initial mass. Model N37.0, although exploding, does not eject any nickel since all the nickel produced falls back onto the compact remnant: this model is compatible with speculations that faint supernovae are associated with fallback and massive

progenitors.

In order to calculate the initial mass function for compact objects, we integrate the remnant mass distribution shown in Fig. 5.6 over a Salpeter initial mass function with exponent 2.35 and map the result into bins of 0.1 $M_\odot$.
Two peaks can be distinguished in the distribution, one for neutron stars, centered around $\sim$ 1.6 $M_\odot$, and one for black holes, centered around $\sim$ 13.8 $M_\odot$. No remnant is produced between the maximum neutron star mass of 2 $M_\odot$ and the minimum black hole mass of 6.5 $M_\odot$.

This result is very different from what found with piston explosions of solar metallicity stars, where no gap is produced and the tipycal black hole mass is around 3 $M_\odot$ [Zhang et al., 2008]. The reason is that in the case of explosions initiated with pistons black holes can only be formed via fallback, which for their choices of mass cut and explosion energy is never more massive than 2-4 $M_\odot$, whereas in neutrino-driven calculations black holes are mostly formed via direct collapse of the core and in this case there in no source of energy that can expel the outermost layers of the star, which will collapse on the compact remnant, forming black holes with a mass around $\sim$ 10 $M_\odot$.

Fryer et al. [2012] find that the distribution of remnant masses depends on the explosion mechanism considered. Their "rapid" explosion mechanism, according to which the explosion occur less than 0.25 s after bounce, produces very few remnants in the region 2-5 $M_\odot$ and black holes up to a maximum mass around $\sim$ 15 $M_\odot$, whereas the "delayed" explosion mechanism produces much more remnants between 2-5 $M_\odot$ and a maximum black hole mass of about 9 $M_\odot$. Therefore our results agree better with the rapid explosion model of Fryer et al. [2012], although according to their definition our explosions are delayed. This is possibly due to the assumptions of Fryer et al. [2012], which do not reproduce the effects of neutrino heating with sufficient accuracy.

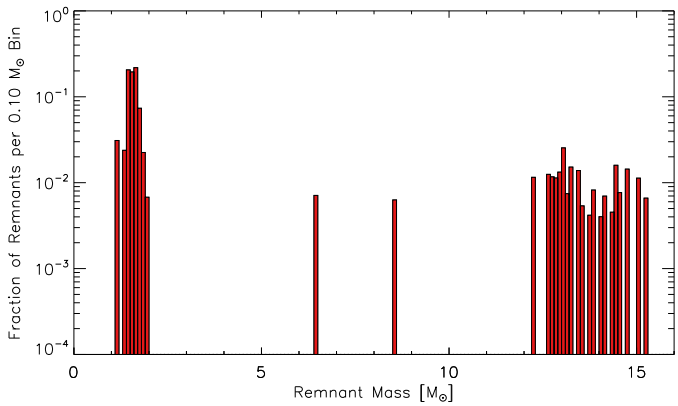

Figure 5.9: Distribution of baryonic remnant masses from explosions of single stars of solar metallicity. Neutron stars and black holes form two separate peaks, with a clear gap between the maximum neutron star mass of 2 $M_\odot$ and the minimum black hole mass of 6.5 $M_\odot$.

The results presented in Figures 5.4-5.8 are summarized in Table 5.1, where we list the explosion time, energy, the initial and final remnant mass, the minimum and maximum of the uncertainty range for the mass of nickel ejected and the total energy emitted in neutrinos, measured at 500 km.

ZAMS [$M_\odot$]	t_{exp} [s]	E_{exp} [B]	$M_{remnant,ini}$ [$M_\odot$]	$M_{remnant,fin}$ [$M_\odot$]	$M_{nickel,min}$ [$M_\odot$]	$M_{nickel,max}$ [$M_\odot$]	ΔE_{tot} [100 B]
10.00	0.260	1.574	1.181	1.181	0.012	0.060	2.043
10.20	0.470	1.541	1.234	1.429	0.018	0.056	2.181
10.80	0.760	1.238	1.425	1.616	0.022	0.045	2.792
11.00	0.300	1.608	1.254	1.447	0.021	0.066	2.335
11.20	0.200	1.577	1.179	1.367	0.026	0.071	2.092
11.40	0.220	1.619	1.213	1.408	0.025	0.071	2.207
11.60	0.250	1.630	1.231	1.432	0.023	0.070	2.261
11.80	0.300	1.669	1.235	1.442	0.042	0.088	2.273
12.00	0.910	1.005	1.445	1.642	0.028	0.047	2.911
12.20	0.690	1.313	1.453	1.633	0.035	0.066	2.957
12.40	0.440	1.713	1.395	1.555	0.031	0.078	2.801
12.60	0.500	1.501	1.354	1.510	0.035	0.079	2.686
12.80	0.210	1.747	1.284	1.431	0.023	0.081	2.449
13.00	0.510	1.558	1.378	1.529	0.049	0.094	2.745
13.20	0.490	1.625	1.458	1.614	0.032	0.076	2.997
13.40	0.420	1.776	1.436	1.584	0.038	0.089	2.936
13.60	0.420	1.785	1.452	1.593	0.042	0.093	2.983
13.80	0.380	1.941	1.448	1.590	0.041	0.097	2.971
14.00	0.450	1.759	1.486	1.628	0.042	0.091	3.111
14.20	0.470	1.780	1.507	1.647	0.048	0.092	3.233
14.40	0.470	1.793	1.518	1.660	0.053	0.096	3.264
14.60	0.540	1.623	1.557	1.698	0.044	0.083	3.344
14.80	0.550	1.480	1.569	1.710	0.045	0.078	3.239
15.00	0.580	1.504	1.600	1.738	0.047	0.080	3.500
15.20	---	0.000	2.574	12.71	0.000	0.000	6.007
15.40	---	0.000	2.626	12.88	0.000	0.000	6.171
15.60	---	0.000	2.623	13.00	0.000	0.000	6.118
15.80	---	0.000	2.566	13.10	0.000	0.000	5.852
16.00	---	0.000	2.543	13.24	0.000	0.000	5.697
16.20	---	0.000	2.622	13.41	0.000	0.000	6.027
16.40	1.240	0.784	1.616	1.755	0.066	0.079	3.520
16.60	0.940	0.909	1.577	1.711	0.064	0.082	3.204
16.80	0.790	1.197	1.527	1.645	0.063	0.092	3.270
17.00	0.800	1.202	1.529	1.645	0.064	0.094	3.277
17.20	0.510	1.511	1.471	1.576	0.065	0.112	3.041
17.40	0.660	1.330	1.498	1.607	0.063	0.099	3.181
17.60	0.510	1.498	1.471	1.576	0.065	0.111	3.042
17.80	---	0.000	2.924	14.45	0.000	0.000	7.356
18.00	---	0.000	2.895	14.49	0.000	0.000	6.947
18.20	---	0.000	2.727	14.57	0.000	0.000	6.340
18.40	0.760	1.000	1.767	1.887	0.067	0.078	4.037
18.60	0.860	0.859	1.586	1.699	0.061	0.081	3.207
18.80	0.930	0.852	1.593	1.708	0.056	0.077	3.469
19.00	---	0.000	2.844	15.03	0.000	0.000	6.681
19.20	1.030	0.613	1.859	1.971	0.057	0.078	4.278
19.40	---	0.000	2.837	15.22	0.000	0.000	6.738
19.60	0.330	1.605	1.448	1.494	0.022	0.080	2.960
19.80	**0.660**	**1.282**	**1.503**	**1.584**	**0.059**	**0.097**	**3.200**
20.00	0.580	1.390	1.431	1.502	0.063	0.106	2.910
20.20	0.320	1.595	1.430	1.488	0.019	0.077	2.907
20.40	0.570	1.392	1.607	1.677	0.074	0.111	3.525
20.60	0.610	1.271	1.774	1.839	0.116	0.134	4.037
20.80	0.920	0.662	1.846	1.887	0.108	0.129	4.146
21.00	---	0.000	2.993	12.99	0.000	0.000	7.299
21.20	---	0.000	2.853	13.55	0.000	0.000	6.720
21.40	---	0.000	3.263	14.79	0.000	0.000	8.223

ZAMS [$M_\odot$]	t_{exp} [s]	E_{exp} [B]	$M_{remnant,ini}$ [$M_\odot$]	$M_{remnant,fin}$ [$M_\odot$]	$M_{nickel,min}$ [$M_\odot$]	$M_{nickel,max}$ [$M_\odot$]	ΔE_{tot} [100 B]
21.60	0.590	1.337	1.552	1.571	0.066	0.108	3.334
21.80	---	0.000	2.839	14.77	0.000	0.000	6.629
22.00	0.810	0.899	1.579	1.599	0.071	0.094	3.202
22.20	---	0.000	3.679	13.21	0.000	0.000	9.391
22.40	0.570	1.334	1.594	1.622	0.073	0.112	3.422
22.60	0.640	1.213	1.728	1.756	0.081	0.111	3.973
22.80	---	0.000	3.710	14.34	0.000	0.000	9.461
23.00	---	0.000	3.856	12.99	0.000	0.000	9.679
23.20	---	0.000	3.783	15.07	0.000	0.000	9.830
23.40	---	0.000	3.856	13.88	0.000	0.000	9.609
23.60	---	0.000	3.878	13.72	0.000	0.000	9.619
23.80	---	0.000	3.866	14.79	0.000	0.000	9.713
24.00	---	0.000	3.887	14.00	0.000	0.000	9.781
24.20	---	0.000	3.857	13.89	0.000	0.000	9.302
24.40	---	0.000	3.846	13.17	0.000	0.000	9.308
24.60	---	0.000	3.847	13.45	0.000	0.000	9.372
24.80	---	0.000	4.260	13.10	0.000	0.000	15.41
25.00	0.580	0.960	1.881	1.895	0.080	0.095	4.241
25.20	---	0.000	3.880	13.11	0.000	0.000	10.09
25.40	---	0.000	3.900	14.14	0.000	0.000	10.01
25.60	---	0.000	3.856	14.12	0.000	0.000	9.720
25.80	0.480	1.278	1.701	1.710	0.050	0.088	3.891
26.00	---	0.000	3.834	12.93	0.000	0.000	9.879
26.20	0.380	1.466	1.577	1.588	0.054	0.110	3.308
26.40	0.380	1.382	1.584	1.596	0.063	0.116	3.243
26.60	0.370	1.664	1.546	1.553	0.053	0.116	3.421
26.80	0.580	1.138	1.549	1.561	0.067	0.110	3.298
27.00	0.390	1.589	1.531	1.539	0.080	0.135	3.318
27.20	0.400	1.579	1.534	1.543	0.083	0.136	3.347
27.40	0.400	1.622	1.567	1.575	0.078	0.133	3.541
27.60	0.390	1.546	1.571	1.581	0.079	0.134	3.390
27.80	0.590	1.176	1.623	1.634	0.076	0.115	3.682
28.00	0.390	1.556	1.527	1.536	0.085	0.141	3.297
29.00	---	0.000	3.097	12.61	0.000	0.000	7.741
30.00	---	0.000	3.239	12.24	0.000	0.000	7.956
31.00	0.570	1.253	1.513	1.524	0.082	0.126	3.233
32.00	0.570	1.150	1.601	1.618	0.080	0.117	3.311
33.00	0.440	1.435	1.603	1.618	0.094	0.142	3.423
34.00	0.640	0.965	1.725	1.757	0.082	0.111	3.899
35.00	0.580	1.127	1.625	1.645	0.071	0.110	3.513
36.00	0.560	1.198	1.633	1.650	0.077	0.117	3.463
37.00	0.950	0.429	1.906	6.465	0.000	0.000	4.371
38.00	0.390	1.604	1.535	1.544	0.091	0.146	3.339
39.00	---	0.000	3.875	8.541	0.000	0.000	10.01
40.00	0.480	1.282	1.716	1.726	0.057	0.095	3.911

Table 5.1: Results for the full set of progenitors exploded with neutrino heating, with parameters calibrated in order to reproduce SN1987A observables with model N19.8 (highlighted in boldface).

5.3.1 Comparison of models with similar initial mass and different outcome

In order to understand the significant variability observed in the explosion energy (Fig. 5.4), we have analyzed many cases of stars of similar initial mass and different outcome (one does not explode while the other does).

N15.0 and N15.2. The evolution of the shock in the two models is similar for the first 0.3 s (Fig. 5.10, left panel), then the accretion rate of model N15.0 starts declining. As soon as the shock crosses the location of the composition interface between the silicon shell and the oxygen-enriched Si layer (black dot-dashed line in Fig. 5.10), the sudden increase in entropy causes the accretion rate to drop and the explosion is launched. For model N15.2, even if the neutrino luminosities are higher (see Fig. 5.11), the accretion rate remains higher and no explosion develops.

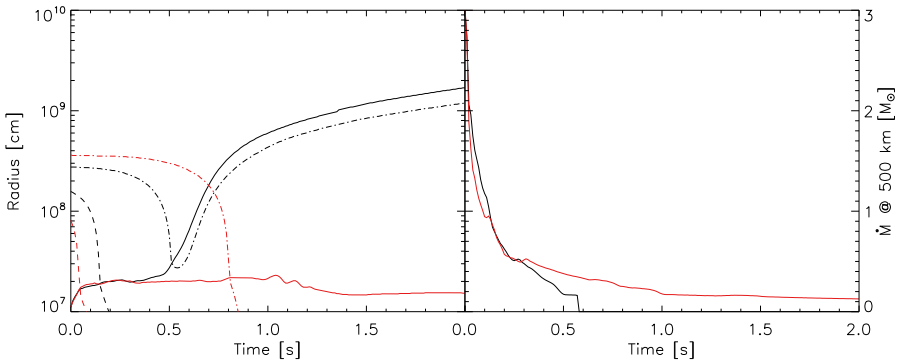

Figure 5.10: Shock radius *(left panel)* and mass accretion rate *(right panel)* as functions of time for models N15.0 (black) and N15.2 (red). In the left panel, the dashed lines mark the trajectory of the edge of the iron core and the dot-dashed lines mark the trajectory of the base of the oxygen burning shell. The explosion for model N15.0 develops when the latter is accreted because of the corresponding drop of the accretion rate.

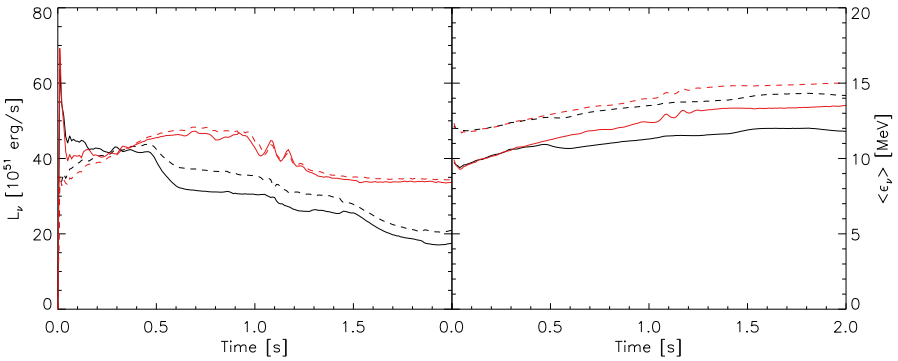

Figure 5.11: Neutrino luminosities *(left panel)* and mean energies *(right panel)* for models N15.0 (black) and N15.2 (red). The solid lines indicate electron neutrinos, the dashed lines electron antineutrinos.

N16.2 and N16.4. In this case the differences between the two models are marginal. The accretion rate of model N16.4 is slightly lower than that of model N16.2. The explosion of model N16.4 happens very late (more than 1 s after bounce) and is aided by the

development of the oscillatory radial instability of the shock, which has been showed to reduce the amount of neutrino energy required for the explosion [Fernández, 2012].
Given the small differences between the two models, it is possible that a small change of the boundary conditions would lead to an explosion also for model N16.2.

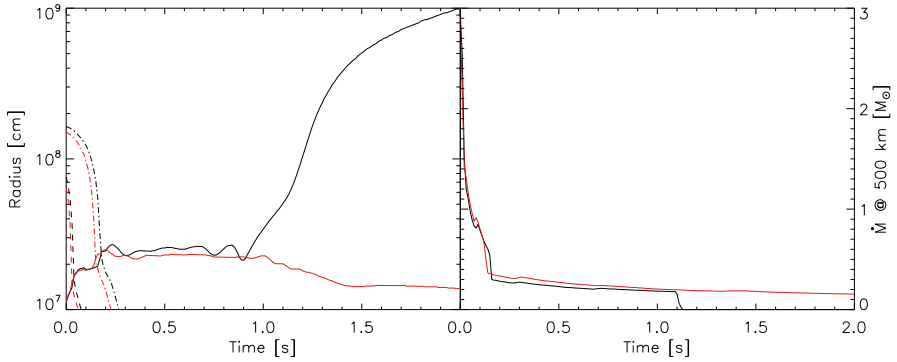

Figure 5.12: Shock radius *(left panel)* and mass accretion rate *(right panel)* as functions of time for models N16.4 (black) and N16.2 (red). In the left panel, the dashed lines mark the trajectory of the edge of the iron core and the dot-dashed lines mark the trajectory of the base of the oxygen burning shell.

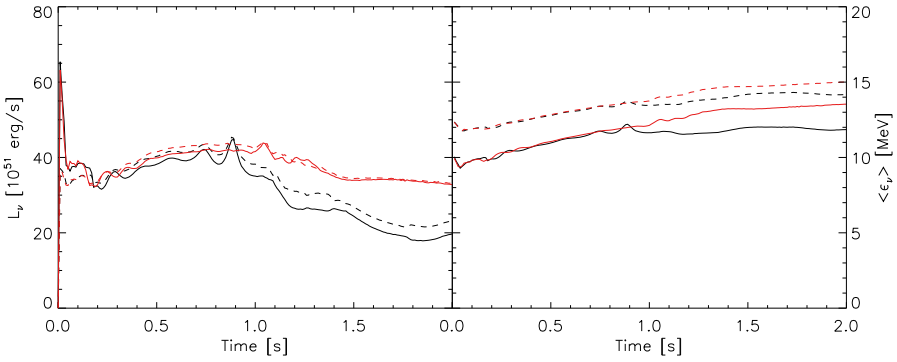

Figure 5.13: Neutrino luminosities *(left panel)* and mean energies *(right panel)* for models N16.4 (black) and N16.2 (red). The solid lines indicate electron neutrinos, the dashed lines electron antineutrinos.

N17.6 and N17.8. This case is very similar to the comparison of N15.0 and N15.2. When the shock of model N17.6 crosses the composition interface between silicon and oxygen, the mass accretion rate drops dramatically and eventually the explosion sets in, whereas for model 17.8 the high accretion rate prevents the shock from moving farther out in radius.

N18.2 and N18.4. In the first 0.6 s of evolution of the models, the conditions are actually less favorable for an explosion of model N18.4 than model N18.2 (smaller shock radius, higher accretion rate, see Fig. 5.16). The accretion of the composition interface happens exactly at the right time to revert this situation and cause an explosion.
The situation is opposite for model N18.2. In this case the accretion of the composition interface happens at a very early time, when neutrinos have not yet deposited enough energy to drive the explosion. Then the situation remains unchanged until eventually the

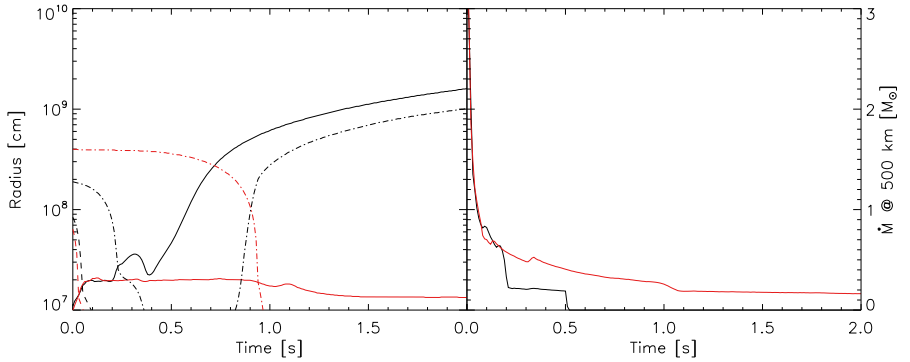

Figure 5.14: Shock radius *(left panel)* and mass accretion rate *(right panel)* as functions of time for models N17.6 (black) and N17.8 (red). In the left panel, the dashed lines mark the trajectory of the edge of the iron core and the dot-dashed lines mark the trajectory of the base of the oxygen burning shell.

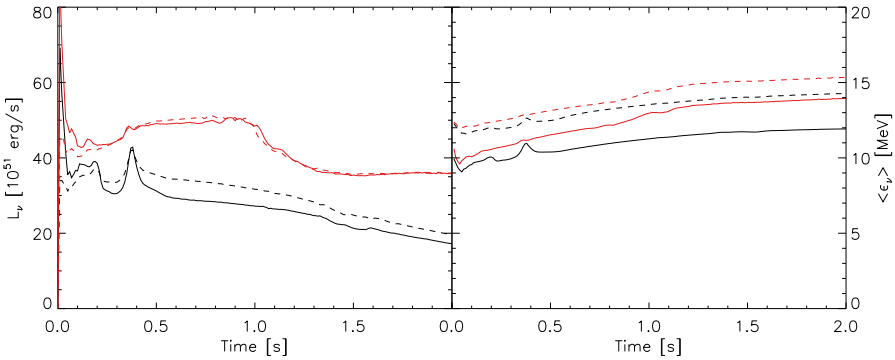

Figure 5.15: Neutrino luminosities *(left panel)* and mean energies *(right panel)* for models N17.6 (black) and N17.8 (red). The solid lines indicate electron neutrinos, the dashed lines electron antineutrinos.

shock reimplodes.

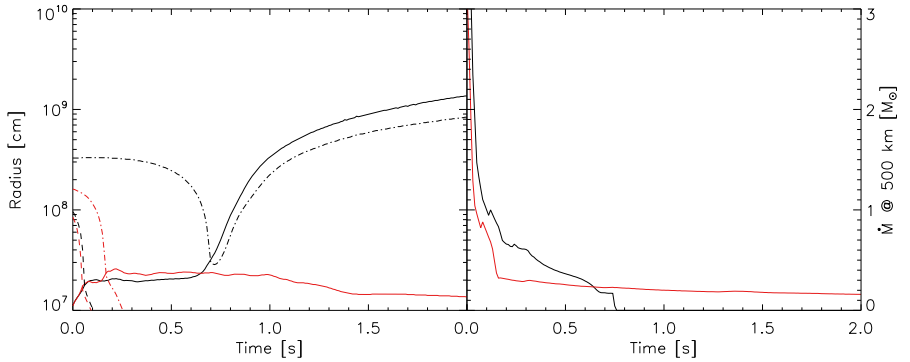

Figure 5.16: Shock radius *(left panel)* and mass accretion rate *(right panel)* as functions of time for models N18.4 (black) and N18.2 (red). In the left panel, the dashed lines mark the trajectory of the edge of the iron core and the dot-dashed lines mark the trajectory of the base of the oxygen burning shell.

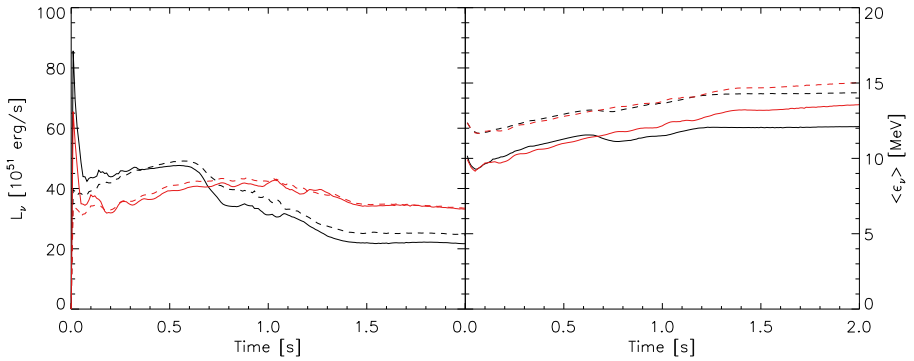

Figure 5.17: Neutrino luminosities *(left panel)* and mean energies *(right panel)* for models N18.4 (black) and N18.2 (red). The solid lines indicate electron neutrinos, the dashed lines electron antineutrinos.

N22.6 and N22.8. In this case both models develop the oscillatory radial instability of the shock, however in the case of model N22.6 the accretion rate is lower and the shock moves farther out, and after one oscillation the explosion is launched, whereas in the case of model N22.8 the higher accretion rate damps the oscillations and there is no explosion.

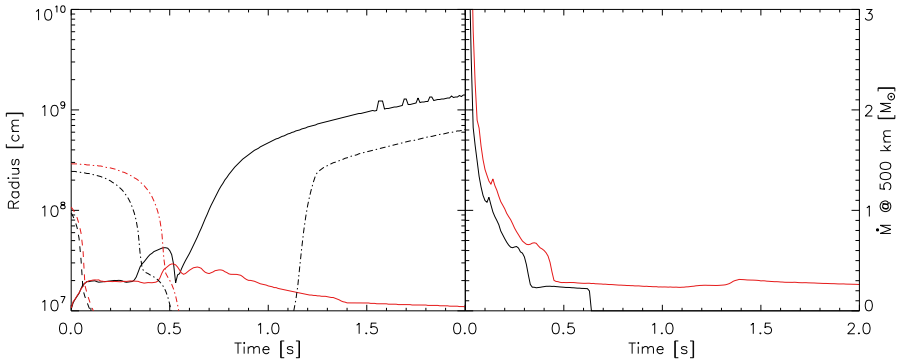

Figure 5.18: Shock radius *(left panel)* and mass accretion rate *(right panel)* as functions of time for models N22.6 (black) and N22.8 (red). In the left panel, the dashed lines mark the trajectory of the edge of the iron core and the dot-dashed lines mark the trajectory of the base of the oxygen burning shell.

We have analyzed several cases of models of similar ZAMS mass and different outcome, and we find that an explosion takes place for favorable combinations of mass accretion rate and neutrino heating, which depends on neutrino $(\nu_e, \bar{\nu}_e)$ luminosities.
In many progenitors an entropy decline at the location of shell interfaces can be supportive of an explosion because the mass accretion rate drops when such feature is accreted by the shock. However this must happen at a time when the energy deposited by neutrinos is sufficient to launch the explosion.
Many models show shock oscillations characteristic of the oscillatory radial instability [Fernández, 2012], that can lead to runaway.

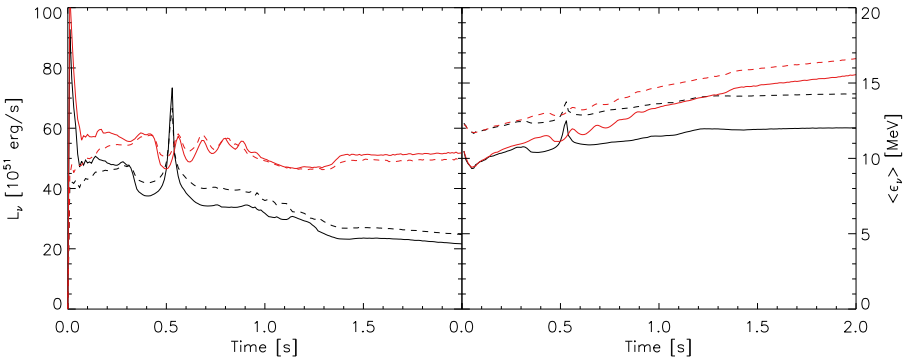

Figure 5.19: Neutrino luminosities *(left panel)* and mean energies *(right panel)* for models N22.6 (black) and N22.8 (red). The solid lines indicate electron neutrinos, the dashed lines electron antineutrinos.

5.3.2 Connection with progenitor properties

We have tried to link the outcome of the core-collapse simulations to properties of the progenitor at the beginning of collapse, in order to understand if the state of a given star can be somehow predicted by its state at the beginning of collapse.
Figure 5.20 shows the mass of the iron core (defined as the location where the electron fraction Y_e increases above 0.497) as a function of the initial mass. We have indicated with red bars the models that explode, and with grey bars the models that do not explode. Many models which do not explode have the most massive iron cores (e.g., all the non-exploding models between 22 and 26 $M_\odot$ and model N39.0). However, the models between 15.2 and 16.4 $M_\odot$ do not explode despite having iron cores less massive than neighbouring stars (e.g. the 14.6, 14.8 and 15.0 $M_\odot$ progenitors). Therefore the iron core alone is not a univocal indicator of the fate of a given star.

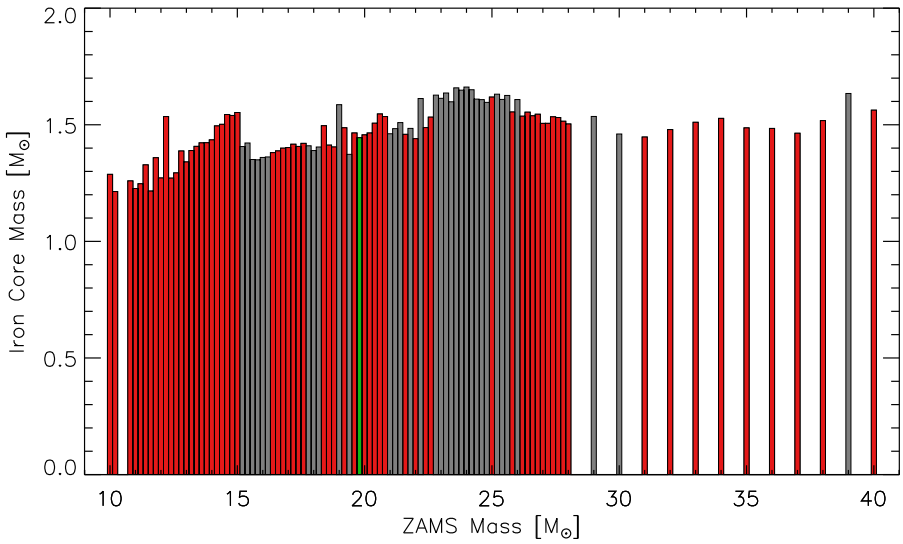

Figure 5.20: Mass of the iron core as a function of ZAMS mass for all progenitors at the onset of collapse. Red bars indicate models that explode, grey bars indicate models that do not explode. The calibration model is marked by a green bar.

Figure 5.21 gives the binding energy of the material outside the iron core. This energy must be overcome by the shock in order to have a successful explosion.
From this plot it is more clear why some models like N15.2 and N15.4 do not explode: despite having not very massive iron cores, the binding energy of the material outside the iron core is greater than that of neighbour exploding models. However, this quantity still does not explain why models like N18.2, N19.0 and N19.4 do not explode while models N18.4 and N19.2, with fatter iron cores and more bound material on top of those, do explode.

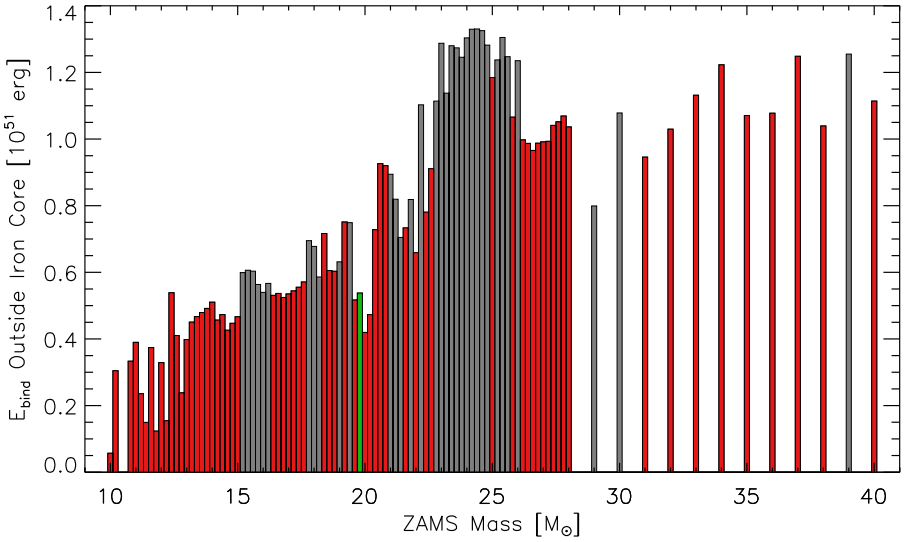

Figure 5.21: Binding energy of matter outside of the iron core as a function of ZAMS mass for all progenitors at the onset of collapse. Red bars indicate models that explode, grey bars indicate models that do not explode. The calibration model is marked by a green bar.

Figure 5.22 displays the mass of the composition interface between the silicon shell and the oxygen-enriched silicon layer, defined as the location where the dimensionless entropy $S/N_a k$ is equal to 4, as a function of the ZAMS mass. The same considerations already given for the previous two plots apply here: while for some models a high value of this quantity correlates to non-explosions, this is not true for all cases.

The last parameter that we have studied is the "progenitor compactness" $\xi_{2.5}$, defined by O'Connor and Ott [2011] as the ratio $\xi_{2.5} = 2.5/[R(M_{bary} = 2.5M_\odot)/(10^8 cm)]$. This quantity is small if 2.5 $M_\odot$ are contained in a large radius, i.e. the progenitor is not very "compact", whereas it is large if such mass is contained in a very small radius. O'Connor and Ott [2011] conclude that this quantity allows first order estimates of the outcome of core-collapse and that for values of $\xi_{2.5}$ below roughly 0.45 the star will explode, whereas it will collapse to a black hole for values above 0.45.
We have plotted $\xi_{2.5}$ as a function of initial mass in Figure 5.23. Of all the progenitor properties that we have analyzed, this quantity gives the best estimate of the outcome of core-collapse: most of the non-exploding models lie in regions of local maxima for $\xi_{2.5}$. However there are still a few exceptions (e.g. N21.0, N21.2, N31.0), and we do not find an absolute value of $\xi_{2.5}$ which can be used as a threshold between explosions and not-explosions like found by O'Connor and Ott [2011]; actually all the progenitors of our set have values of $\xi_{2.5}$ equal to or lower than 0.45, therefore we cannot confirm that this value is a good estimator for the fate of core-collapse.

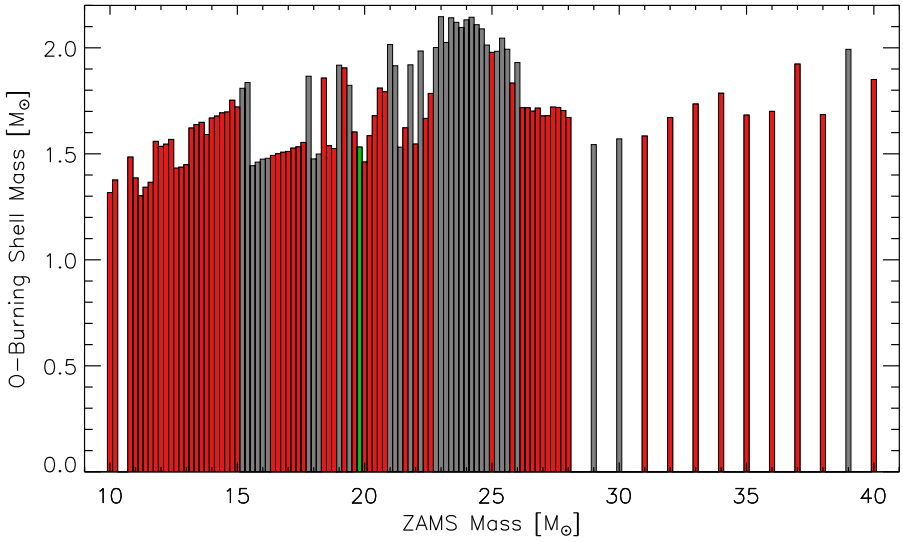

Figure 5.22: Mass of the location of the base of the oxygen-burning shell as a function of the initial mass for all progenitors at the onset of collapse. Red bars indicate models that explode, grey bars indicate models that do not explode. The calibration model is marked by a green bar.

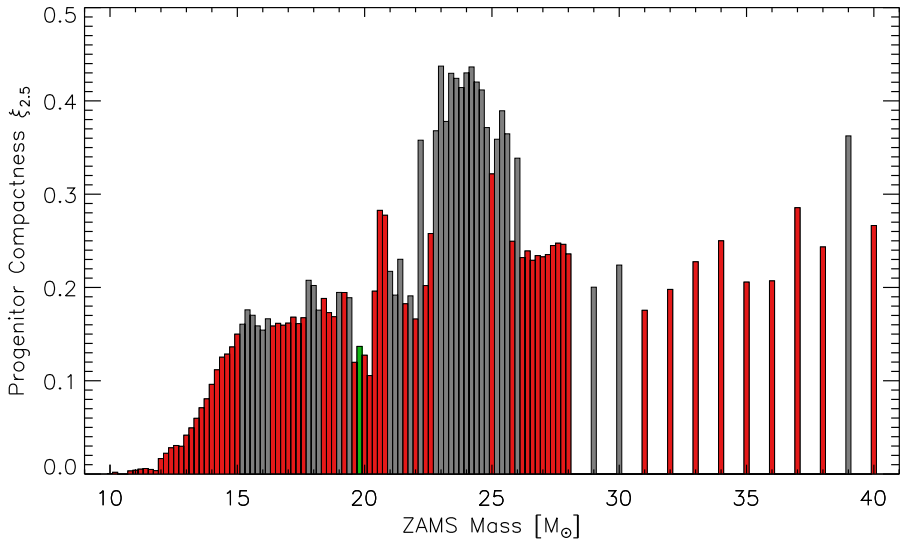

Figure 5.23: Progenitor compactness $\xi_{2.5}$ as a function of ZAMS mass for all progenitors at the onset of collapse. Red bars indicate models that explode, grey bars indicate models that do not explode. The calibration model is marked by a green bar.

One might argue that the difference is caused by the fact that O'Connor and Ott [2011] calculate $\xi_{2.5}$ at the time of bounce while we calculate it at the time of onset of collapse. However for the set of progenitors considered here there is hardly any difference in calculating $\xi_{2.5}$ at these two different times, as can be seen comparing our values of $\xi_{2.5}$ (given in Table 3.1) with those of O'Connor and Ott [2011] (see the second group of models in

Table 1).

We have compared the results of our set with several progenitor properties in order to understand wether the fate of a given star can be predicted based on some property at the onset of collapse. We have found that there is not a simple or a few progenitor properties that can be used to predict the possibility of an explosion, which depends on the detailed structure of the progenitor and on a delicate interplay of different factors during the evolution (mass accretion rate, neutrino heating, shock instabilities).

5.4 Conclusions

In this Chapter we have presented the results of spherically symmetric explosion simulations for a set of about 100 progenitor stars of solar metallicity. The explosions were initiated by means of a neutrino-heating scheme that depends on parametrized neutrino quantities (luminosities and mean spectral energies) based on an analytic cooling model of the high-density core of the nascent neutron star. The free parameters of this model were calibrated in order to reproduce the observed properties of SN1987A, namely the explosion energy, the remnant mass and the mass of nickel ejected, with a suitable progenitor of the employed set (here chosen to be the 19.8 $M_\odot$ star). The evolution of the explosion models was followed beyond shock breakout from the stellar surface.

Because of strong star-to-star variations of the progenitor structure at the onset of collapse, we find a great variability of supernova properties (such as explosion energy, compact remnant mass, and ejected nickel mass) even in narrow progenitor-mass windows. However there is not a single or a few progenitor properties which can be used to predict the possibility of an explosion, which depends on the detailed structure of the progenitor and on a delicate interplay of different factors during the evolution (favorable combination of mass accretion rate and neutrino heating, development of shock instabilities).

Our novel approach and results allow to establish better links of theoretical explosion models with observations.

Conclusions

In this thesis I have presented a novel approach to the study of the connection between progenitors and the properties of core-collapse supernovae and their compact remnants. Such connection has been studied for more than thirty years, mainly with simulations in which the explosions were initiated by means of completely artificial mechanisms, such as thermal energy deposition or pistons. Such mechanisms have the severe drawback of imposing by hand the mass cut and the explosion energy, therefore they can greatly influence the outcome of core-collapse.

The novel approach presented in this thesis is based on a physically motivated mechanism to initiate the explosions, namely neutrino heating. Deposition of energy by neutrinos has been proposed as a mechanism to drive explosions already in the 1960s, and although the viability of this explosion mechanism is still under debate, it is clear that neutrino heating plays an important role in core collapse [Janka et al., 2007]. Moreover, recent sophisticated multidimensional simulations with detailed neutrino treatment are at least near the critical conditions for a success of the neutrino-driven mechanism [Buras et al., 2006b, Marek and Janka, 2009, Müller et al., 2012]. Therefore, adopting this approach is likely to be a step towards more realistic modeling of the explosions.
The explosions are thus initiated by means of a neutrino-heating scheme that depends on parametrized neutrino quantities (luminosities and mean spectral energies) based on an analytic cooling model of the high-density core of the nascent neutron star.

In Chapter 4 I have compared the proposed method with the piston method commonly adopted in literature, and I have showed that the results of the two methods are considerably different, especially for more massive stars. When the parameters of each method are adjusted in order to explode each progenitor with roughly the same energy, the piston method produces more massive remnants and ejects far less nickel than the neutrino method. Since the piston method is not based on a physical model of the explosion mechanism, employing the neutrino method is a step towards more realistic modeling of the explosion and more reliable predictions.

In Chapter 5 I have presented the results of spherically symmetric explosion simulations for a set of about 100 progenitor stars of solar metallicity, exploded with the proposed method. The free parameters of this method are calibrated in order to reproduce the observed properties of SN1987A, namely the explosion energy, the remnant mass and the mass of nickel ejected, with a suitable progenitor of the employed set (here chosen to be the 19.8 $M_\odot$ star). The evolution of the explosion models was followed beyond shock breakout from the stellar surface.

Because of strong star-to-star variations of the progenitor structure at the onset of collapse, we find a great variability of supernova properties (such as explosion energy, compact remnant mass, and ejected nickel mass) even in narrow progenitor-mass windows. However there is not a single or a few progenitor properties which can be used to predict

the possibility of an explosion, which depends on the detailed structure of the progenitor and on a delicate interplay of different factors during the evolution (favorable combination of mass accretion rate and neutrino heating, development of shock instabilities).
Our novel approach and results allow to establish better links of theoretical explosion models with observations.

Acknowledgements

I would like to say thanks to my advisor Hans-Thomas Janka, for his supervision during this three and a half years and for his many essential inputs to this work.
Thanks also to Almudena Arcones, for her co-supervision on the project, for her support, and for introducing me to the code.
A special thanks goes to Lorenz and Janina, for being friends more than colleagues, and to all the group members for many useful discussions and good moments. Many thanks to Andreas and Lorenz for computing the collapse and bounce phases of the models that I have used in this work.
Furthermore my thanks go to Wolfgang Hillebrandt and the Max-Planck Institute for Astrophysics, for their enduring support and the exceptional scientific environment they have created in Garching.
I would also like to thank the MPA secretary staff, Maria, Gabi and Cornelia, for being very helpful and friendly.
Last but not least, thanks to my boyfriend and my parents, who always helped and supported me. This accomplishment would not have been possible without them.

Contents

Bibliography

A. Arcones, H.-T. Janka, and L.Scheck. Nucleosynthesis-relevant conditions in neutrino-driven supernova outflows i. spherically symmetric hydrodynamic simulations. *Astronomy and Astrophysics*, 467:1227--1248, 2007.

W. D. Arnett, J. N. Bahcall, R. P. Kirshner, and S. E. Woosley. Supernova 1987a. *Annual Reviews of Astronomy and Astrophysics*, 27:629--700, 1989.

M. B. Aufderheide, E. Baron, and F. K. Thielemann. hock waves and nucleosynthesis in type ii supernovae. *The Astrophysical Journal*, 370:630--642, 1991.

A. Bauswein, H.-T. Janka, K. Hebeler, and A. Schwenk. Equation-of-state dependence of the gravitational-wave signal from the ring-down phase of neutron-star mergers. *Physical Reviews D*, submitted, 2012.

H. A. Bethe. Supernova mechanisms. *Reviews of Modern Physics*, 62:801--866, 1990.

H. A. Bethe and J. R. Wilson. Revival of a stalled supernova shock by neutrino heating. *Astrophysical Journal*, 295:14--23, 1985.

H. A. Bethe, G. E. Brown, J. Applegate, and J. M. Lattimer. Equation of state in the gravitational collapse of stars. *Nuclear Physics A*, 324:487--533, 1979.

J. M. Blondin, A. Mezzacappa, and C. DeMarino. Stability of standing accretion shocks, with an eye toward core-collapse supernovae. *The Astrophysical Journal*, 584:971--980, 2003.

R. Buras, M. Rampp, H.-T. Janka, and K. Kifonidis. Improved models of stellar core collapse and still no explosions: What is missing? *Physical Review Letters*, 90:241101, 2003.

R. Buras, M. Rampp, H.-T. Janka, and K. Kifonidis. Two-dimensional hydrodynamic core-collapse supernova simulations with spectral neutrino transport. i. numerical method and results for a 15 msun star. *Astronomy and Astrophysics*, 447:1049--1092, 2006a.

R. Buras, M. Rampp, H.-T. Janka, and K. Kifonidis. Two-dimensional hydrodynamic core-collapse supernova simulations with spectral neutrino transport. ii. models for different progenitor stars. *Astronomy and Astrophysics*, 457:281--308, 2006b.

A. Burrows. Supernova neutrinos. *The Astrophysical Journal*, 334:891--908, 1988.

A. Burrows and J. M. Lattimer. The birth of neutron stars. *The Astrophysical Journal*, 307:178--196, 1986.

A. Burrows, E. Livne, L. Dessart, C. D. Ott, and J. Murphy. A new mechanism for core-collapse supernova explosions. *The Astrophysical Journal*, 640:878--890, 2006.

P. Colella and H. M. Glatz. Efficient solution algorithms for the riemann problem for real gases. *Journal of Computational Physics*, 59:264--289, 1985.

P. Colella and P. R. Woodward. The Piecewise Parabolic Method (PPM) for Gas-Dynamical Simulations. *Journal of Computational Physics*, 54:174--201, 1984.

S. A. Colgate. Hot bubbles drive explosions. *Nature*, 341:489--490, 1989.

Stirling A. Colgate and Richard H. White. The hydrodynamic behavior of supernovae explosions. *The Astrophysical Journal*, 143:626, 1966.

P. B. Demorest, T. Pennucci, S. M. Ransom, M. S. E. Roberts, and J. W. T. Hessels. A two-solar-mass neutron star measured using shapiro delay. *Nature*, 467:1081--1083, 2010.

W. M. Farr, N. Sravan, A. Cantrell, L. Kreidberg, C. D. Bailyn, I. Mandel, and V. Kalogera. The mass distribution of stellar-mass black holes. *The Astrophysical Journal*, 741:103, 2011.

R. Fernández. Hydrodynamics of core-collapse supernovae at the transition to explosion. i. spherical symmetry. *The Astrophysical Journal*, 749:142, 2012.

C. L. Fryer. Mass limits for black hole formation. *The Astrophysical Journal*, 522:413--418, 1999.

C. L. Fryer. Fallback in stellar collapse. *New Astronomy Reviews*, 50:492--495, 2006.

Chris L. Fryer, K. Belczynski, G. Wiktorowicz, M. Dominik, V. Kalogera, and D. E. Holz. Compact remnant mass function: Dependence on the explosion mechanism and metallicity. *The Astrophysical Journal*, 749:91, 2012.

S. V. Goldreich, P.; Weber. Homologously collapsing stellar cores. *The Astrophysical Journal*, 238:991--997, 1980.

F. Hanke, A. Marek, B. Müller, and H.-Th. Janka. Is strong sasi activity the key to successful neutrino-driven supernova explosions? *The Astrophysical Journal*, submitted, 2011.

M. Hashimoto, K. Nomoto, and T. Shigeyama. Explosive nucleosynthesis in supernova 1987a. *Astronomy and Astrophysics*, 210:L5--L8, 1989.

A. Heger, C. L. Fryer, S. E. Woosley, N. Langer, and D. H. Hartmann. How massive single stars end their life. *The Astrophysical Journal*, 591:288--300, 2003.

K. Hirata, T. Kajita, M. Koshiba, M. Nakahata, and Y. Oyama. Observation of a neutrino burst from the supernova sn1987a. *Physical Review Letters*, 58:1490--1493, 1987.

H.-T. Janka. Conditions for shock revival by neutrino heating in core-collapse supernovae. *Astronomy and Astrophysics*, 368:527--560, 2001.

H.-Th. Janka. *Neutrino transport in type-II supernovae and protoneutron stars by Monte Carlo methods*. PhD thesis, Technische Universität München, 1991.

H.-Th. Janka and E. Müller. Neutrino heating, convection and the mechanism of Type-II supernova explosions. *Astronomy and Astrophysics*, 306:167--198, 1996.

H.-Th. Janka, K. Langanke, A. Marek, G. Martínez-Pinedo, and B. Müller. Theory of core-collapse supernovae. *Physics Report*, 442:38--74, 2007.

K. Kifonidis, T. Plewa, H.-Th. Janka, and E. Müller. Non-spherical core collapse supernovae. *Astronomy and Astrophysics*, 408:621--649, 2003.

F. S. Kitaura, H.-Th. Janka, and W. Hillebrandt. Explosions of o-ne-mg cores, the crab supernova, and subluminous type ii-p supernovae. *Astronomy and Astrophysics*, 450: 345--350, 2006.

J. M. Lattimer and F. Douglas Swesty. A generalized equation of state for hot, dense matter. *Nuclear Physics A*, 535:331--376, 1991.

A. I. MacFadyen, S. E. Woosley, and A. Heger. Supernovae, jets and collapsars. *The Astrophysical Journal*, 550:410--425, 2001.

A. Marek and H.-T. Janka. Delayed neutrino-driven explosions aided by the standing accretion shock instability. *The Astrophysical Journal*, 694:664--696, 2009.

A. Marek, H. Dimmelmeier, H.-T. Janka, E. Müller, and R. Buras. Exploring the relativistic regime with newtonian hydrodynamics: an improved effective gravitational potential for supernova simulations. *Astronomy and Astrophysics*, 445:273--289, 2006.

A. Mezzacappa, M. Liebendörfer, O. E. Messer, W. R. Hix, F.-K. Thielemann, and S. W. Bruenn. Simulation of the spherically symmetric stellar core collapse, bounce, and postbounce evolution of a star of 13 solar masses with boltzmann neutrino transport, and its implications for the supernova mechanism. *Physical Review Letters*, 87:1935--1938, 2001.

B. Müller, H.-Th. Janka, and A. Marek. A new multi-dimensional general relativistic neutrino hydrodynamics code for core-collapse supernovae ii. relativistic explosion models of core-collapse supernovae. *The Astrophysical Journal*, submitted, 2012.

Eric S. Myra and Sidney A. Bludman. Neutrino transport and the prompt mechanism for type ii supernovae. *The Astrophysical Journal*, 340:384--395, 1989.

T. Nakamura, U. Hideyuki, K. Iwamoto, K. Nomoto, M. Hashimoto, W. R. Hix, and F. K. Thielemann. Explosive nucleosynthesis in hypernovae. *The Astrophysical Journal*, 555: 880--899, 2001.

K. Nomoto and M. Hashimoto. Presupernova evolution of massive stars. *Physical Reports*, 163:13--36, 1988.

K. Nomoto, N. Tominaga, H. Umeda, C. Kobayashi, and K. Maeda. Nucleosynthesis yields of core-collapse supernovae and hypernovae, and galactic chemical evolution. *Nuclear Physics A*, 777:424--458, 2006.

Evan O'Connor and Christian D. Ott. Black hole formation in failing core-collapse supernovae. *The Astrophysical Journal*, 730:70, 2011.

F. Özel, D. Psaltis, R. Narayan, and J. E. McClintock. The black hole mass distribution in the galaxy. *The Astrophysical Journal*, 725:1918--1927, 2010.

M. Rampp and H.-T. Janka. Radiation hydrodynamics with neutrinos. variable eddington factor method for core-collapse supernova simulations. *Astronomy and Astrophysics*, 396:361--392, 2002.

M. Rampp and H.-Th. Janka. Spherically symmetric simulation with boltzmann neutrino transport of core collapse and postbounce evolution of a 15 solar mass star. *The Astrophysical Journal*, 539:L33--L36, 2000.

L. Scheck, K. Kifonidis, H.-Th. Janka, and E. Müller. Multidimensional supernova simulations with approximative neutrino transport. I. Neutron star kicks and the anisotropy of neutrino-driven explosions in two spatial dimensions. *Astronomy and Astrophysics*, 457:963--986, 2006.

J. Schwab, Ph. Podsiadlowski, and S. Rappaport. Further evidence for the bimodal distribution of neutron star masses. *The Astrophysical Journal*, 719:722--727, 2010.

L. I. Sedov. *Similarity and Dimensional Methods in Mechanics*. New York: Academic Press, 1959.

G. Shen, C. J. Horowitz, and S. Teige. New equation of state for astrophysical simulations. *Physical Review C*, 83:035802, 2011.

T. Shigeyama, K. Nomoto, and M. Hashimoto. Hydrodynamical models and the light curve of supernova 1987a in the large magellanic cloud. *Astronomy and Astrophysics*, 196: 141--151, 1988.

S. J. Smartt. Progenitors of core-collapse supernovae. *Annual Review of Astronomy and Astrophysics*, 47:63--106, 2009.

F. Douglas Swesty, James M. Lattimer, and Eric S. Myra. The role of the equation of state in the 'prompt' phase of type ii supernovae. *The Astrophysical Journal*, 425:195--204, 1994.

F. K. Thielemann, M. Hashimoto, and K. Nomoto. Explosive nucleosynthesis in sn 1987a. ii - composition, radioactivities, and the neutron star mass. *The Astrophysical Journal*, 349:222--240, 1990.

F.-K. Thielemann, K. Nomoto, and M.-A. Hashimoto. Core-collapse supernovae and their ejecta. *The Astrophysical Journal*, 460:408, 1996.

F. X. Timmes and F. Douglas Swesty. The accuracy, consistency, and speed of an electron-positron equation of state based on table interpolation of the helmholtz free energy. *The Astrophysical Journal Supplement*, 126:501--516, 2000.

E. F. Toro. *Riemann Solvers and Numerical Methods for Fluid Dynamics*. Springer, 1999.

R. Valentim, E. Rangel, and J. E. Horvath. On the mass distribution of neutron stars. *Monthly Notices of the Royal Astronomical Society*, 414:1427--1431, 2011.

J. R. Wilson, R. Mayle, S. E. Woosley, and T. Weaver. Stellar core collapse and supernova. *Annals of the New York Academy of Sciences*, 470:267--293, 1986.

S. E. Woosley and A. Heger. Nucleosynthesis and remnants in massive stars of solar metallicity. *Physical Reports*, 442:269--283, 2007.

S. E. Woosley and T. A. Weaver. The physics of supernova explosions. *Annual Review of Astronomy and Astrophysics*, 24:205--253, 1986.

S. E. Woosley and T. A. Weaver. The evolution and explosion of massive stars. ii. explosive hydrodynamics and nucleosynthesis. *The Astrophysical Journal Supplement*, 101:181--235, 1995.

S. E. Woosley, A. Heger, and T. A. Weaver. The evolution and explosion of massive stars. *Reviews of Modern Physics*, 74:1015--1071, 2002.

W. Zhang, S. E. Woosley, and A. Heger. Fallback and black hole production in massive stars. *The Astrophysical Journal*, 679:639--654, 2008.